Politecnico di Torino

Politecnico di Torino

Corso di Laurea Magistrale in Ingegneria Meccanica- Fabbricazione Additiva
A.A. 2020/2021
Sessione di Laurea di Ottobre 2021

Influence of the laser beam focus on the mechanical properties and microstructure of AlSi10Mg processed by L-PBF

Tutors

Prof.ssa Federica Bondioli (Academic)

Dott. John Stavridis (Company)

Dott.ssa Alberta Aversa (Academic)

Dott. Fabrizio Marinucci (Academic)

Candidate

Luca Cotto 265277

Sommario

1. Abstract 5
2. State of art 6
2.1. What is Additive Manufacturing 6
2.2. AM History 8
2.3. Advantages and disadvantages 11
2.4. Complexity for free 14
2.5. AM process 15
2.5.1. Post processing 17
2.6. MAM techniques 18
2.6.1. Powder Bed Fusion Systems 19
2.6.2. Direct Energy Deposition Technology 29
2.6.3. MAM techniques comparison 31
2.7. MAM materials 32
2.7.1. Aluminum alloys 32
2.7.2. Titanium alloys 32
2.7.3. Nickel Alloys 33
2.7.4. Fe-based Alloys 33
2.7.5. Cobalt Chrome alloys 33
2.8. Significance of laser beam focus variation on the quality of the printed components 34
2.8.1. The effect of VED 35
2.8.2. The effects of melt-pool behaviors 35
2.9. AlSi10Mg for L-PBF 37
3. Material and Methods 44
3.1. Samples Modelling 44
3.2. Samples Building 45
3.3. Metallographic characterization 48
3.3.1. Cutting 48
3.3.2. Grinding and polishing 49
3.3.3. Chemical Etching 52
3.3.4. Image acquisition 53
3.3.5. Image analysis 56
3.3.6. Fracture Surface Analysis 58
3.4. Mechanical tests 59
3.4.1. Tensile test 59

3.4.2. Microhardness 61
4. Results & Discussion 63
4.1. Microstructure characterization 63
4.1.1. Porosity 63
4.1.2. Melt pool analysis 68
4.1.3. Microstructure Analysis 70
4.2. Mechanical tests 72
4.2.1. Tensile Test 72
4.2.2. Microhardness 76
4.2.3. Fracture Surface Analysis 77
5. Conclusion 80
6. Appendix A 81
7. Bibliography 82

1. Abstract

Over the last decade, additive technologies have become one of the most interesting manufacturing techniques within the industry, particularly for metal techniques. Starting from the CAD file, Additive Manufacturing (AM) machines allow to produce any geometric shape without the usage of tools. Generally, the process is slower than convectional techniques, but it strongly depends on the geometrical complexity. What makes this process interesting are the many advantages it has, such as the reduction of components, the number of assemblies and the free design approach. There are several techniques available on the market for the fabrication of metal parts. The two main techniques are: Powder Bed Fusion (PBF) and Direct Energy Deposition (DED).

The aim of this analysis is to evaluate the effect of laser beam focus variation on the microstructure and mechanical properties of parts made of AlSi10Mg, produced by the Laser-PBF technique. The AlSi10Mg alloy is often used in the Additive Manufacturing field as it presents good casting characteristics, a narrow cooling range and good specific strength. The main fields of usage for this alloy are the automotive and aeronautical industries.

Thanks to the partnership between Politecnico di Torino and Prima Industria SpA, three different laser spot sizes were analyzed, coinciding with the conditions of -1.5, 0, +1.5 mm focusing distance. Nine samples were produced by Prima Additive PrintSharp 250. For each laser spot condition, 3 cubes for the microstructure characterization and 6 samples for the tensile tests were analyzed. Porosity, microstructure and melt pool analysis were carried out for the cubic samples. The tensile specimens were used for the tensile tests and characterization of the fracture surfaces.

The analysis was conducted as follows. Initially the state of the art of AM technology was described, in particular the process, the metal techniques and the materials. Subsequently, the methodologies adopted to perform the analysis were described. Next, the results were exposed and discussed. Possible future evolutions of the conducted analysis were exposed as last topic.

2. State of art

2.1. What is Additive Manufacturing

Additive Manufacturing (AM) is a new family of technologies that allows to produce three dimensional objects layer by layer with high complex geometry, directly from the CAD model. This technique requires the 3D model of the part, that it will be sliced into 2D thin layers by a software. The AM machines are able to deposit locally material in 2D layers and to repeat this process layer by layer until the top, obtaining the three dimensional object. ASTM defines[1] Additive Manufacturing as "A process of joining materials to make objects from 3D model data, usually layer upon layer, as opposed to subtractive manufacturing methodologies".

At the beginning, the purpose of AM technology was to produce part for improving the prototyping process. In fact, in the 1980s it was called Rapid Prototyping (RP) [2]. Many companies used this technique because allows to produce very quickly whatever part, directly from the CAD model, without the use of tools. Engineers could create different prototypes, analyze and/or test it before their release and commercialization. This activity had a big role in the AM expansion and consolidation[3].

Another important factor that had a role in AM expansion was the change in the consumer goods market [4]. As the customization and complexity of products have been increased enormously from the 1980s to the present day, at the same time, lifetimes and delivery times have been drastically reduced. For these reasons, efficient development of new products is necessary to maintain the competitiveness of companies in the market.

The first AM technology was Stereolithography (SLA)[5], born in 1985. During the following years different types of polymeric systems were born. The change from RP to AM is associated to the production of final parts. This score is obtained thanks to the research of new materials and systems that allows to have fully dense parts in traditional, or similar, materials. Nowadays several kinds of materials can be used by AM technology: different types of polymers, ceramics and metals are used, but they are few compared to traditional methods[6].

Nowadays, AM techniques are widely used and the AM market is constantly growing as new applications are discovered in various manufacturing fields. Design engineers can now decide to manufacture the parts they are studying using either AM or traditional techniques, exploiting the advantages of both techniques. They differ essentially in their approach, whether additive or subtractive, in their work volumes, both single part and productivity, and in their design freedom.

Wohlers et al. [7]conducted an analysis of AM industry growing, according to the data published, in Figure 1 represents the distribution of AM revenues for the end-market in 2018, and represents the industrial adoption of AM.

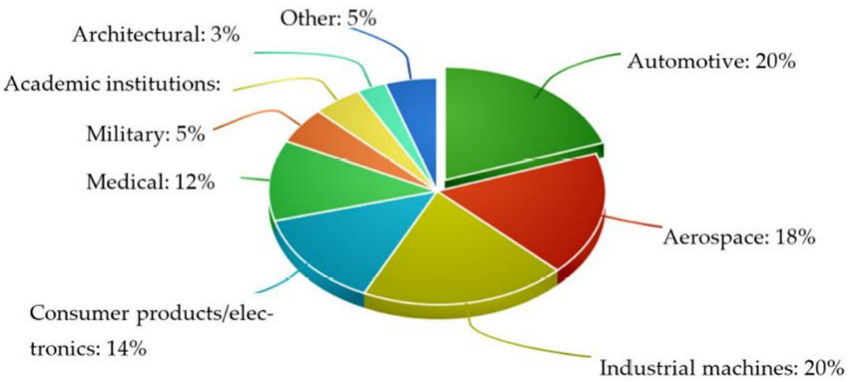

Figure 1: Industrial adoption of Additive Manufacturing [7]

Automotive, Aerospace and Industrial Machine are the main sectors of AM market, they cover over the 68% of the global AM revenues. Other sector interested in AM is the Biomedical field. Thanks to this technique prothesis and other customize parts are possible to be realized. These sectors are also ones of the main richest manufacturing fields, this because AM activity is very expensive and is useful when high-performance components occurs.

ASTM [8]had defined seven categories for classified AM, these are indicated in Table 1.

Table 1: ASTM classification (2012)[8]

Process categories	Technology	Materials
Binder Jetting	3D Printing Ink-jetting S-Print M-Print	Metal Polymer Ceramic
Direct Energy Deposition	Direct Metal Deposition Laser Deposition Laser Consolidation Electron Beam Direct Melting	Metal: powder and wire
Material extrusion	Fused Deposition Modeling	Polymer
Material Jetting	Polyject Ink-jetting Thermojet	Photopolymer Wax
Powder bed fusion	Selective Laser Sintering Selective Laser Melting Electron Beam Melting	Metal Polymer Ceramic
Sheet lamination	Ultrasonic Consolidation Laminated Object Manufacture	Hybrids Metallic Ceramic
Vat photopolymerization	Stereolithography Digital Light Processing	Photopolymer Ceramic

The AM techniques choice first of all depends on the material, secondly to other factors like the surface roughness, the build rate, the volume of the part and so on.

The most common techniques for Metal Additive Manufacturing are Laser Powder Bed Fusion (L-PBF), Direct Energy Deposition (DED) and Electron Beam Melting (EBM)[2]. They will be analyzed in the following chapter.

2.2. AM History

As mentioned above, Additive Manufacturing was born as a technique used to make prototypes. Thanks to this possibility, the representation and conceptualization of the projects had been facilitated. The first patent of RP system was applied by Hideo Kodama [9] in 1980 It sintered photopolymers by UV exposure, controlled by a mask model.

In 1983, an engineer from Colorado that produced coatings with UV lamps, invented the Stereolithography (SLA) technique. His name was Chuck Hull and after three years, in 1986, he founded 3D System company [4]. This system uses a basin full of UV photopolymer resin and a laser beam for curing the resin. When laser cure the 2D layer, the platform goes down, deep in the resin and next layer can be cure, so the process continues until the parts are finish.

In 1986, Carl Deckard and other researchers, at University of Texas, introduced the Selective Laser Sintering (SLS) system. This technique, compared to SLA, uses thermoplastic polymer in powder form and the laser source is more powerful for melt the powder. The process is different because with this technique the raw materials need to be spread over the melt layer and the supports can be recycled[4].

In 1988, Scott and Lisa Crump patented FDM system (Fused Deposition Modelling), showed in Figure 2. This technique is able to create 3D parts thanks to the deposition of thermoplastic filament, layer by layer, by a moving extruder. The thermoplastic filament is passed through a heated nozzle, melts and is laid on a platform or on previous layers, giving it the shape of the relevant section. Once the layer has been laid, the procedure is repeated. The parts produced by this technology are easily recognizable due to the low surface finish caused by the discrete deposition of material. Nowadays, it is the most famous AM technique. In fact it is possible to buy low-cost machines (Figure2) and make any object. However, these machines are very different from industrial printers in terms of resolution and repeatability[10].

Figure 2: Fused Deposition Modelling machine

In 1993, Emanuel Sachs, professor from MIT University, developed Three Dimensional Printing System (3DP). This technique was able to print all types of materials and to realize parts in different colors, but the main disadvantage was to produce no definitive parts. 3DP uses material in powder form. Its consolidation is not due to a heat source, but to the selective addition of an adhesive agent. This substantial difference made possible to use any material for the production of objects using the 3DP technique[11].

During the same years, more and more interest was focused on Metal Additive Manufacturing (MAM), since it could be used in many areas with great advantages. Universities and other research centers began to develop new methods and techniques for producing ready-to-use objects. The first technique was invented by Fraunhofer Society, in 1995, and its name was Selective Laser Melting (SLM). This system is twins of SLS systems, but SLM is able to melt the metal powder thanks to a more powerful source.

Other MAM system was Laser Engineered Net Shaping (LENS), developed by Optomec Company in 1998. This technique sprays the metal powder in a small zone where laser source hit the surface. This combination creates a binding cord that will generate a final part. This approach to material deposition has also been used by other techniques, which are known as DED techniques. The EBAM technique is similar to the LENS technique but uses metallic material in the form of wires and the fusion is enabled by an electron beam. This technique is very interesting because it allows parts to be made even in space[12].

Another technology that uses an electron beam to fuse the material is the EBM technique. EBM machines have been on the market since 1997 and have developed rapidly due to their higher productivity than MAM techniques. Today, EBM machines are widely used in the manufacture of turbine blades for aircraft engines[5].

In 1999, EXTRUDEHONE introduced Metal Binder Jetting AM process This technology is based on the consolidation of metal powder particles by means of a binder. The advantages of using the binder are that it produces more accurate structures without supports than the SLM technique[5].

Thanks to high development of new systems, materials and control systems at the beginning of 2000's AM were used in the production of ready to use products. This goal was achieved also thanks to the reduction of the price of raw materials, compared to the beginning. Nowadays AM techniques are consolidated in different manufacturing field, like aerospace and automotive field. For example, typical applications of MAM are the manufacture of engine nozzles, aircraft, human prothesis and dental implants[3].

Today AM is still a sector in evolution, research centers, universities and R&D company centers continue to develop new elements for AM consolidation in a huge manufacturing filed. Smart Tech, published their forecast into AM grow (Figure 3), from 2017 to 2028, in automotive field. It shows that AM revenues in

automotive field will increase up to 12,43 billion dollars with high expansion of the polymeric prototyping and production of metal final parts[13].

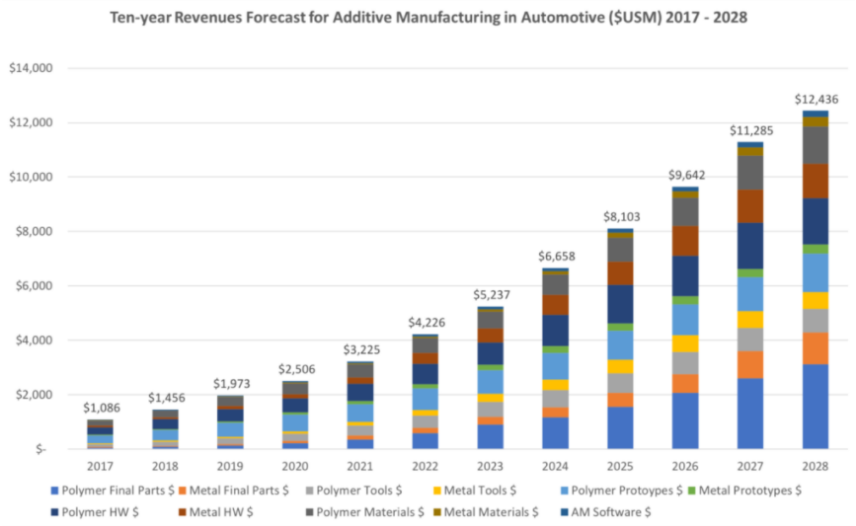

Figure 3: Smart Tech forecast of Automotive Additive Manufacturing Revenues 2017-2028[13]

2.3. Advantages and disadvantages

AM is a new technology that has large differences compared to traditional methods. The main advantages of AM technology are[14]:

- **Complexity and free design**

  Thanks to layer-by-layer approach every kind of geometry/feature are possible to be created. For example, it is possible to create internal channel inside a part (Figure 4), parts already joined together after print and a trabecular/lattice structure (Figure 4). Other important aspect is that the cost and time are not correlated to geometry complexity.

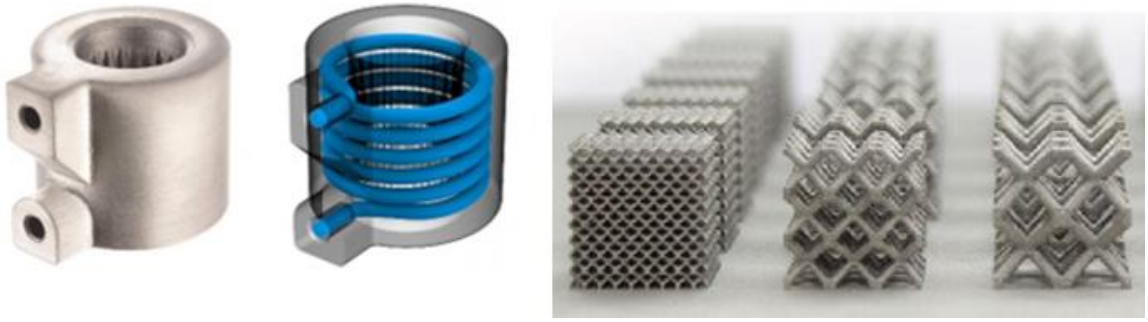

Figure 4: Free design examples. Part with internal channel [15] (left) and lattice structure [16] (right).

- **Optimization**

  Optimization is the first way to enhance complexity advantage. There are different ways to optimize a part produced with AM, it is possible enhance the mechanical characteristics of the structure, the dynamic or thermal behavior, the weight, etc. Typically, after geometry optimization is very complex to produce parts with traditional methods. In Figure 5, an example of the design optimization of a component is shown.

Figure 5:Weight optimization example [17]

- **Waste materials**

  Local deposition is one of the main features of AM techniques. This feature is a great advantage rather than conventional techniques because the material is deposited only where it is needed. At the end of the job, the parts are already finished and don't need more manufacturing processes to define their shape, they need only support removal process (when they are present). Therefore, no or little quantity of material is wasted. For example, in the case of L-PBF technology, the unfused powders are reused, after a granulometry check, while in subtractive methods shavings need to be refused.

- **Time saving**

  The high flexibility of AM is very useful in prototyping, that's why it allows to create parts with complex shape in one step. Traditional methods require different steps to create a final part and often they need specific equipments. During the development of a new product, design and features change quickly, so AM is perfect for this scope. Only changing the CAD model is possible to create in one step the prototypes without using equipment. In traditional methods, the number of producing steps increases with the complexity and so the prototyping step is longer. This implies to introduce later the product in the market, compared to the competitors, and so the reduction of the profit of the company.

- **Autonomy**

  Typically, AM machines have a high level of autonomy, during the printing process, no operator is required. Nowadays machine preparation and job unloading are done by AM technicians. In recent years, AM machine companies try to increase the activity managed autonomously by the machine.

- **Customization**

  Compared to traditional methods, an AM machine can produce whatever geometries. This allows to customize the product for the user and creates different customized products in a single job. These abilities are largely used in medical field for prothesis and dental field for implants.

On the other hand, AM technology is not proficient in every manufacturing field, there are some disadvantages that limit the applications. The main are [18]:

- **Working volume**

  The working volume is highly dependant on the AM technology. In MAM the powder bed technologies are limited by the weight of powder, the straight tolerance and the cost of the materials. In the other

hand, DED technology allows to produce bigger parts but there are also volume limits due to the heat transmission. In the following chapter more informations about MAM working volume are exposed.

- **Roughness**

Roughness is one of the main disadvantages of AM. Due to the layer-by-layer approach and other effects, the roughness is higher compared to traditional methods (Figure 6). This implies that coupling zones or specific features need post-processing operation with traditional methods. Correlated to this disadvantage, traditional methods need features for machining operations, so the free design advantage is limited.

Figure 6: Surface roughness comparison between as-build L-PBF part vs coin [19].

- **Building rate velocity**

As building rate velocity, in AM field, we consider the volume of materials deposited per hour. This parameter is lower compared to the volume of materials subtract per hour in CNC machines, so the productivity of AM machine is lower. Many researchers are focusing on increasing the deposition rate and reduce the time correlated to the build preparation and job unloading.

- **Materials**

The materials for AM are often different compared to the same materials for traditional methods: for example in PBF technology the raw materials are spherical powders. This implies an increase of the price more than 10 times due to the gas atomization process. Another problem correlated to the material is the availability: many materials are not available for AM machines. Many researchers tried to introduce new alloys or traditional alloys in AM market, inducing a decrease in the price of materials.

- **Supports**

Supports are indispensable in most of AM techniques. At the end of the process, supports are removed by AM technician and often are wasted. Some software houses, that work in AM field, introduced tools to reduce the volume of supports during the printing process.

- **Anisotropy**

  Anisotropy was one of the first problems of the AM technology, this behavior happens when layers do not correctly join, so it is correlated to layer-by-layer approach. Nowadays this effect is present, but it is less significant than the beginning.

2.4. Complexity for free

Complexity for free is a slogan introduced in the AM world to show the advantages of using AM, but also to indicate its criticisms. In Figure 7 the production cost of a component using additive or traditional technology has been plotted against the geometric complexity of the object. It is clear that the cost of additive technology is not influenced by the complexity, while for traditional technologies there is an exponential increase in price as the complexity increases. These trends are related to the time saving and complexity of AM techniques. That's why, as the complexity increases, more tools and equipment are needed in the case of traditional techniques, while in AM the machine can realize any geometry in one step. On the other hand when the geometric complexity is low, conventional manufacturing is better because it allows to low-cost parts with high productivity

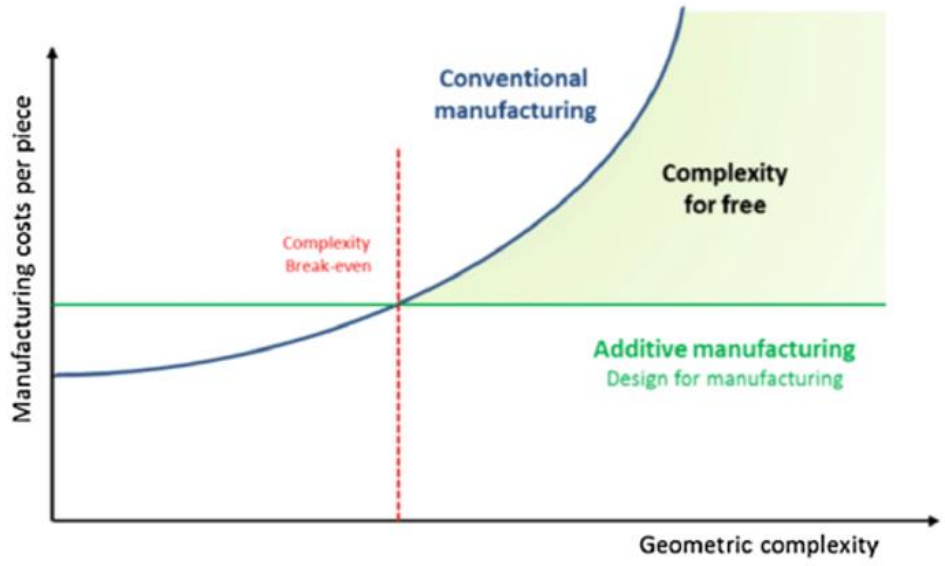

Figure 7: Comparison of conventional vs AM techniques as a function of geometric complexity and manufacturing cost per piece [20]

2.5. AM process

The AM process or workflow (Figure 8) could be divided into 8 steps [13].

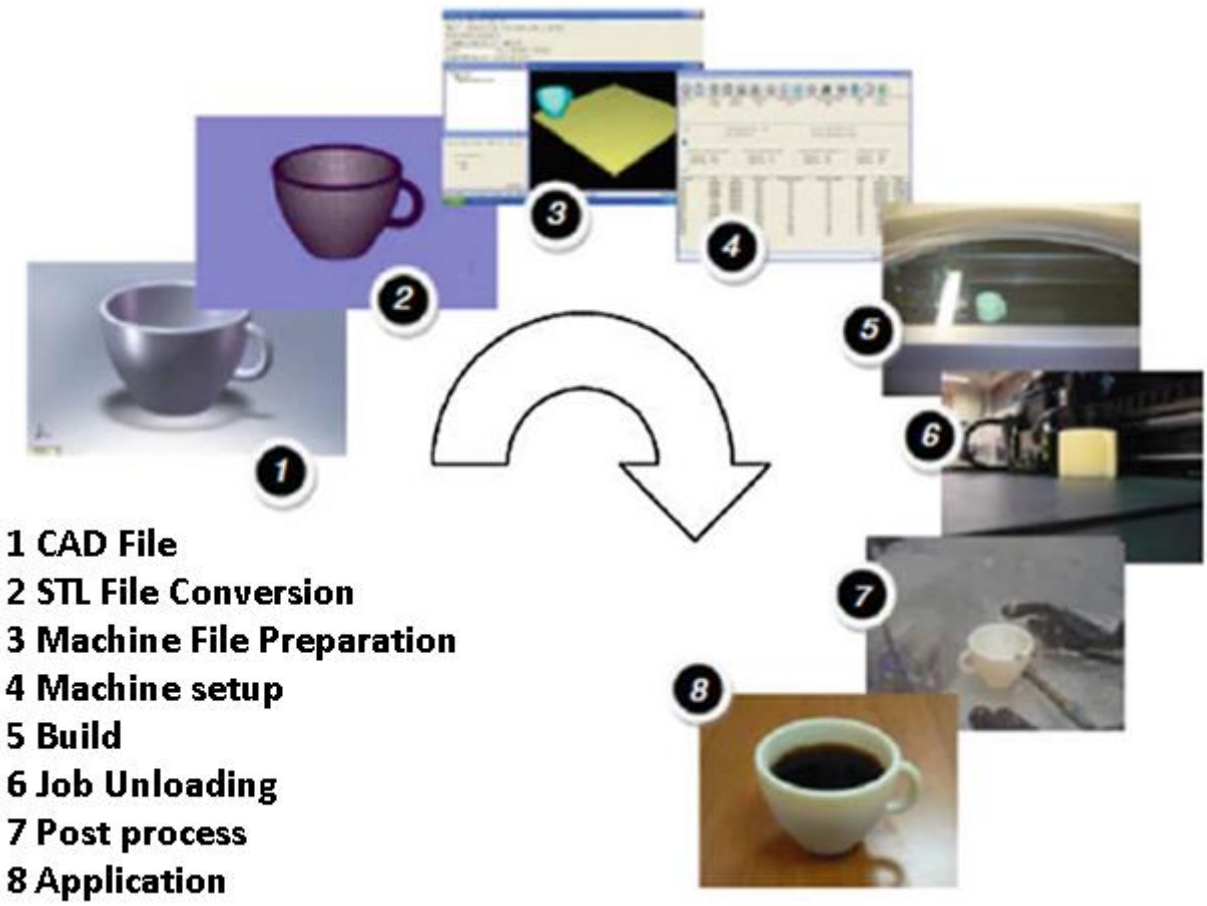

Figure 8: AM workflow [21]

These are:

- **CAD file**

  The creation of CAD file is the first step to produce a part with AM technology. CAD acronym stands for Computer Aided Design, so CAD file is a software model of a geometry created by specific software, like SolidEdge, Katia, NX, etc. CAD files can be obtained also from a physical object, thanks to reverse engineering. Engineers or users use these software to create the part or an assembly. After that, the file is saved for the next steps. The output file must be a 3D solid or surface representation. Although it is possible to analyze, optimize and conduct simulations of the part before the STL conversion.

- **STL file conversion**

  The conversion from CAD file to STL file format is necessary because the AM machines work with this format. The acronym STL stands for Standard Triangulage Language and it was born with Rapid Prototyping, in particular with SLA technique. The conversion of the file maintains the geometry of the part but changes the description of external surfaces. This operation is required also for the sliding process.

- **Machine file preparation**

  AM machine requires STL file format. It is necessary to transfer the file to the machine and manipulates it for allocating the parts into the working volume. If the parts require supports, they are created in this step. The sliding process is conducted as the last operation.

- **Machine setup**

  Before starting the building process, the machine must be set. Different parameters can be chosen, like layer thickness, and some procedures must be adopted to ensure the building of a correct part. These procedures are strongly related to AM techniques and materials.

- **Build**

  Building process is mainly an automated process, so supervision is not necessary. Usually, AM operator checks the process for the first layers to ensure no errors.

- **Job unloading**

  Once the building process is finished the parts must be removed from the working volume. This operation is very different in the AM techniques and it can require interaction with the machine and the use of safety devices like masks or gloves.

- **Post-process**

  Once the parts are removed from the machine, they can require additional processes before the application. Different processes can be adopted, they strongly depend on the AM techniques, materials and their application. The main post-process activities are explained in the next paragraph.

- **Application**

  When all the previous steps are completed the part is finally ready to be used.

2.5.1. Post processing

Post processing operations in AM often are done because few techniques allow to had a ready to use part. Different operations can be conducted after the printing process. The main activities are[22]:

- Heat treatment
- Cutting
- Remove supports
- Part cleaning
- Surface texture improvement
- Machining

The operations that will be conducted strongly depend on the material, applications and the technique. In particular for an industrial part produced by L-PBF, it is required first of all a cleaning process. The part is sandblasting to remove the unfused powder on the surface, next, if the part has internal features, they are clean. This operation is very important because if the powder remains inside the part, after the next process of heat treatment, it sinters and can plug the internal features.

The second process is the stress relief heat treatment. It allows to reduce the stress inside the material and allows the cutting process. The cutting process is not conducted before stress relief because, due the internal stress, some elements of the part can be deformed. Other heat treatments can be carried out to increase the mechanical properties.

The part is then cut from the construction platform, typically using the wire-Electrical Discharge Machining (wire-EDM) method.

After cutting, if the part has supports, these are removed manually using tools. Sometimes some supports are removed by the subsequent machining process, such as supports for holes.

The machining process often is necessary when there are features that require a special finishing or tight tolerances that cannot be achieved with the L-PBF process [4].

2.6. MAM techniques

At the beginning, metals materials were not commonly used due to their high cost. Also AM machines were not able to melt the material. In the last two decades, thanks to the consolidation of AM and the development of new AM systems and materials, MAM attracts market attention.

American Society for Testing and Materials (ASTM) International Committee F42, classified AM process into seven categories[1]. Of these categories, the following four pertain to MAM:

- Powder Bed Fusion (PBF)
    - Selective Laser Melting (SLM)
    - Electron Beam Melting (EBM)
- Direct Energy Deposition (DED)
    - Laser or e-beam
    - Wire fed or Powder fed
- Binder Jetting (BJ)
    - Infiltration
    - Consolidation
- Sheet Lamination
    - Ultrasonic Additive Manufacturing (UAM)

The most common MAM techniques are the Powder Bed Fusion and the Direct Energy Deposition. In the following paragraph they will be analyzed.

2.6.1. Powder Bed Fusion Systems

PBF machines, as the name suggests, use as raw materials metals in powder form. This is possible thanks to the gas atomizing process that allows to transform melt metal into micro-scale spheres. There are two different techniques based on the powder bed fusion system: the Laser Powder Bed Fusion (L-PBF) and the Electron Beam Melting (EBM). Essentially, they differ in the energy source. In the first case, energy is provided by one or more lasers, while in the second one the energy is provided by electron beam gun[23].

The PBF machines are very complex, they are made up of 6 main systems. These are:

- Recoating system
- Power supply
- Energy source system
- Motors
- Environmental system
- Focusing and scanning system

Both EBM and L-PBF machines have these systems, but the components often are different.

In general, the building process is the same for both the techniques. It starts with the deposition of the powders on the platform by the recoating system. The platform usually is made with the same material of the powder to avoid different expansion of the part and platform during the building process. When the powder is spread on the platform, the melting process can start. Thanks to the power source movement system, the energy beam is used for selectively melting the powder in the area defined by the first slice of the 3D model. When the first layer is finished, the platform goes down of the layer thickness chosen and the next powder layer deposition is possible. The process continues as described until the part is finished[12].

The Powder Bed Fusion techniques are very complex. During the building process many parameters affect the final part. Among these, there are energy source power, beam spot, beam focus, scan speed, building temperature, powder size, powder density and scanning strategy. Liu et al[24], reported that the scanning strategy is the second most influential parameter in the manufacture of an additive technology component. The scanning strategy refers to the logic of movement of the laser in the creation of the section of the component. It influences the disposal of heat and therefore the final microstructure of the component. Typically, the most used scanning strategy is the “zig-zag” scan with multiple remelting of the contour, as this improves the surface finish. Other strategies are used and optimized for specific applications. In Figure 9, some examples of scanning strategies are shown.

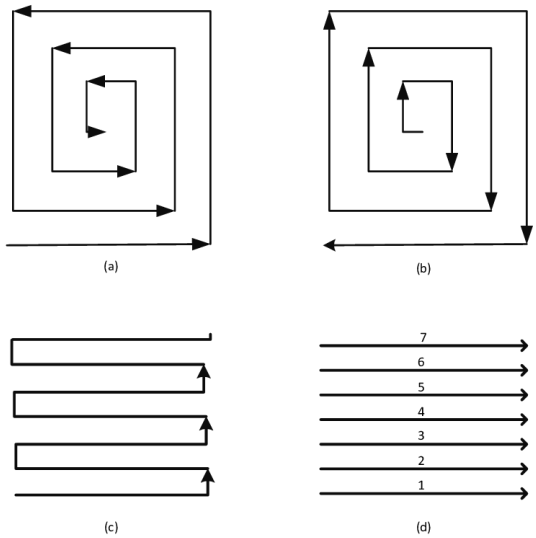

Figure 9: Scanning strategies example [25], (a) In-spiral, (b) Out-spiral, (c) Antiparallel/Zigzag, (d) Parallel

A very important characteristic of PBF process is the melt pool. It is created by the energy beam and is essentially composed by melt metal. Its proprieties are fundamental for a fully dense part. The main geometrical characteristics of melt pool are the width and the penetration depth, they are shown in Figure 10. When a correct process occurs, melt pool is little bit wider than the beam spot and penetrates greater than the layer thickness. This last condition occurs to ensure the correct attachment between the layer, so reducing the anisotropy. Figure 11 show a representation of PBF process. Typically, the beam penetrates two or three times the layer thickness. Nowadays process control system analyzes beam spot and other melt pool proprieties, like temperature, to check the correctness of the process [12].

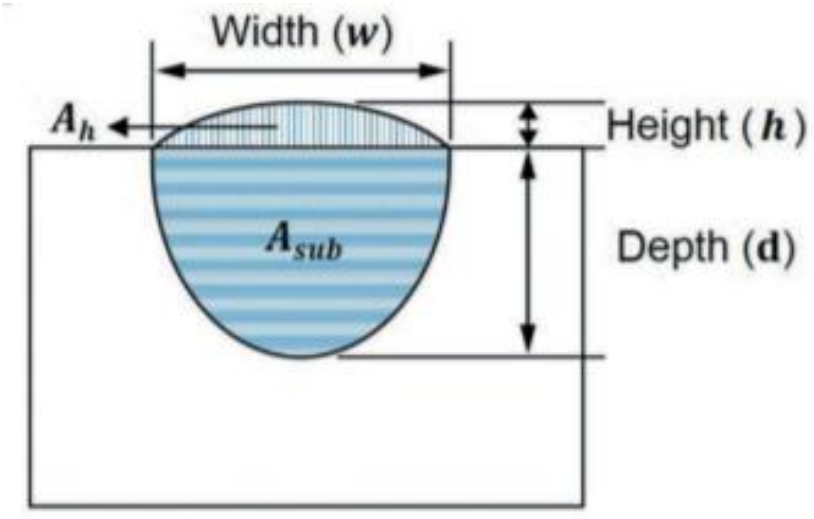

Figure 10: Melt pool geometrical characteristics [26]

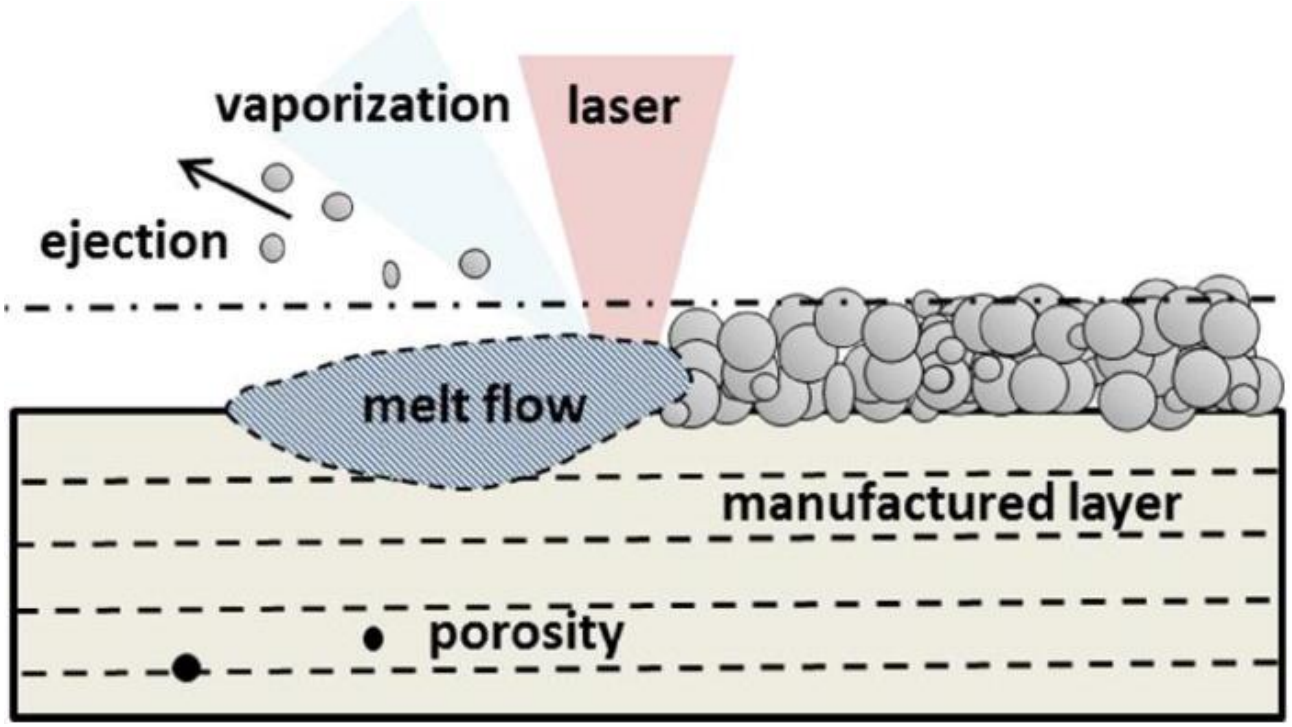

Figure 11: PBF process representation [27]

During PBF machine setup, AM operator must check the quantity of the powder in the machine, at least the amount of powder must cover the entire working volume for the height of the desired part. At the end of the process, the working volume is cleaned and the unfused powders are recycled by a sieve shaker. Recycled powder must separate from the un-used powder because they will be mixed, according to the metallurgist indication [28].

This technique is largely used because allows to realized parts with higher mechanical/metallurgical characteristics compared to traditional methods. This goal is obtained thanks to the rapid solidification of the material after the fusion (about 10^6-10^7 °C/min). For these reasons, often a distension process is conducted before cutting the parts from the platform [29].

2.6.1.1. *Laser Powder Bed Fusion Technology*

As described before, L-PBF technology uses laser as energy source. When the laser hits the powder photons interact with matter and energy exchange occurs generating heat. If the energy provided is enough, metals powder melts and solidifies very quickly, so local deposit occurs. It is possible to use a wide kind of lasers, The most common are CO2 laser, Nd fiber lasers, YAG laser and disk laser. Every laser emits photons with a specific wavelength, so this changes the laser-powder interaction and powder ablation can happen[30].

In Figure 12, a sketch of L-PBF machine is illustrated. These elements are placed inside a metal chamber isolated from the environment by a door. In some case it is provided of a gloves box.

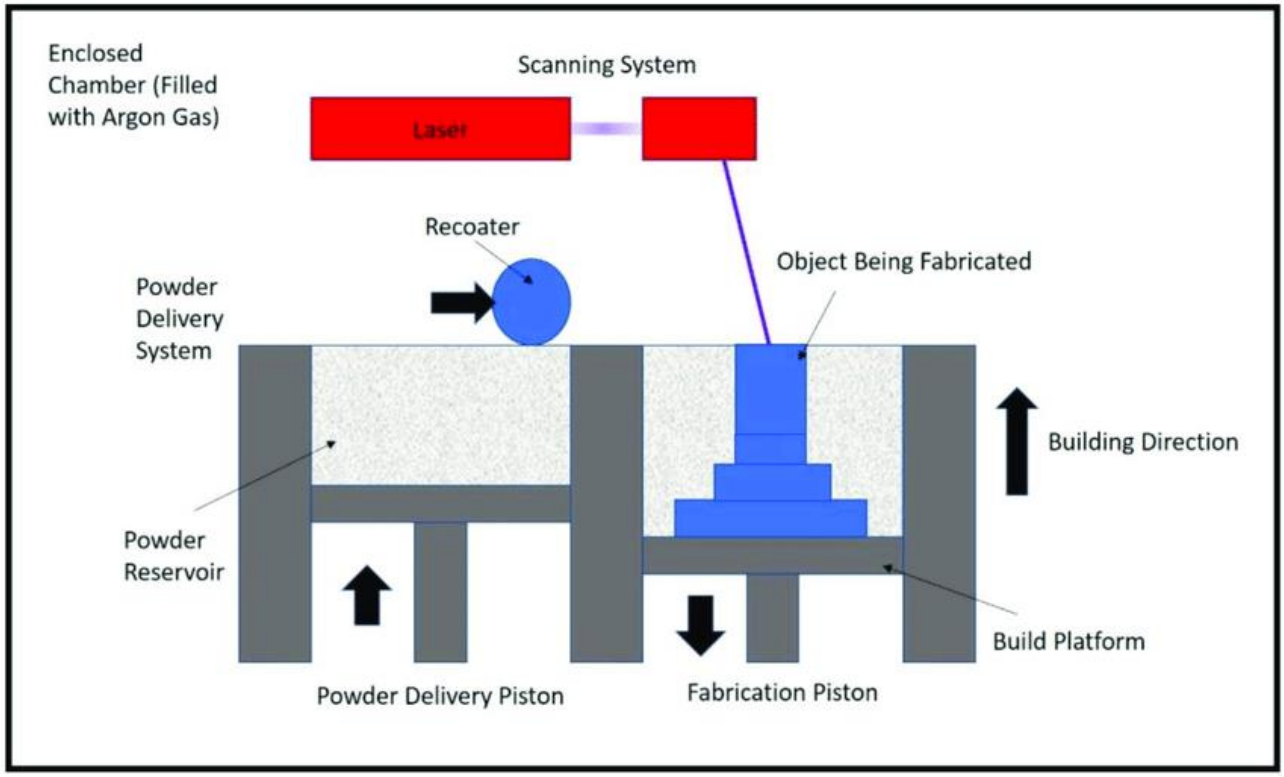

Figure 12: L-PBF machine systems [31]

On top of the machine is located the laser, it is able to generate the laser beam that is directed into the scanning system where, thanks to moving mirrors, the laser beam is directed on the powder bed. Mirrors managed to machine software, move the laser on the surface and create the cross-section of the object, in according to the sliced 3D CAD model. The fabrication and the powder delivery piston move upward or downward the powder bed with very high resolution and tolerance to assure the correctness of the layer thickness. The recoater is required to spread the powder above the fabrication powder bed. In the L-PBF machine the recoater can be a roller or racle, it depends on the company and it can be made in polymer or metal [12].

Figure 12 does not show the construction platform, which is clamped to the moving platform. It is necessary because the deposition must take place on a removable platform. Before starting the fusion of the first layer, and during printing, the platform is heated up to 200°, according to material and machine, in order to guarantee the adhesion of the first layers. A heated platform is also required to reduce the cooling gap, and so the internal stresses. During L-PBF process, inert atmosphere is required because the metal powder is very reactive with oxygen. For this reason, before the printing process, the working chamber is filled with inert gas, usually nitrogen or argon to lower the oxygen level below 500 ppm (part per million). The type of gas is related to the material. For example with titanium that is strongly reactive, argon is recommended. Inert gas performs also a second role: the direction of gas flow is random or fixed, but during the process it can be changed. This happens because when metal melts, low melting elements produce smoke that can interact with the laser, so the propriety of final part can vary. For this reason, gas flow is directed in the opposite direction respect the scanning direction. Figure 13 show a graphic representation of laser-smoke interaction[4].

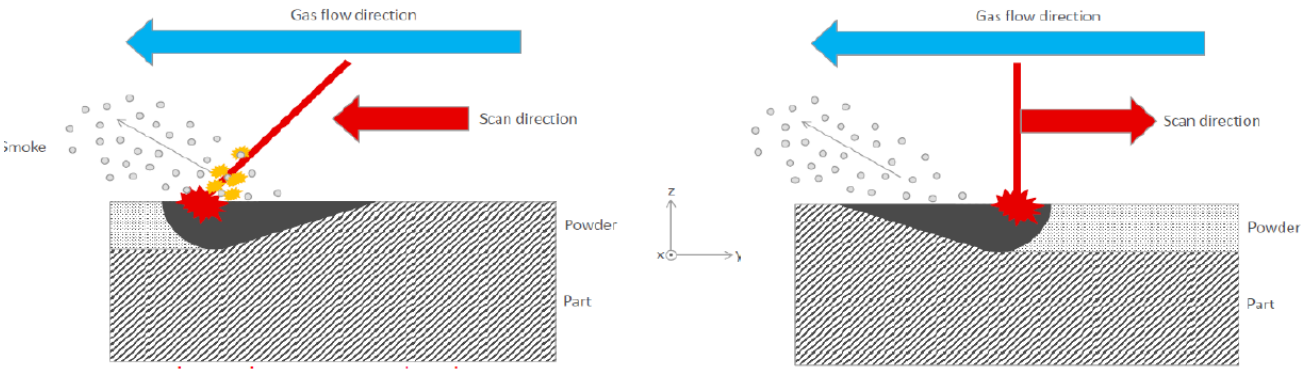

Figure 13: Laser smoke interaction [32]

With L-PBF technology a wide range of materials can be adopted, the most common are[33]:

- Titanium alloy, Ti6Al4V is the most used
- Inconel alloy
- Aluminum alloy, AlSi10Mg is the most used
- Cobalt Chrome alloy
- Maraging Steel
- Stainless Steel
- Copper

The metals are used in powder form with a specific granulometry, the powder range size for L-PBF process is 20-60 µm. In the next chapter, more information about materials is presented.L-PBF technique allows to print several parts with high complex geometry, up to volume saturation, in a single job. In addition a part

produced with this technology has better characteristic in terms of accuracy and roughness compared to the other MAM techniques[23].

In the market, the main L-PBF machines companies' seller are Prima Industrie SpA, EOS, SLM Solution and Renishaw. Everyone has machines with different sizes or with different integrated technologies, for example the working area available is in order of 150 to 400-500 millimeters. This limitation of the working area is reflected on the printed products, so it is not possible to print large parts.

2.6.1.2. *Electron Beam Melting Technology*

EBM technology was born in the early years of 1990s thanks to the collaboration of Goteborg University. It was patented by Ralf Larson in 1993. Next, Ralf Larson founded Arcam company and their systems were commercialized since 1997. In 2016, General Electric sold Arcam company. Compared to L-PBF technology, EBM machines are sold only by Arcam company. The building process is very similar to L-PBF technology, but some differences discern the technology and their applications. In Figure 14, a sketch of EBM machine is illustrated. As L-PBF technique, the systems, excluding the energy source system and focusing system, are located inside an isolated chamber[34].

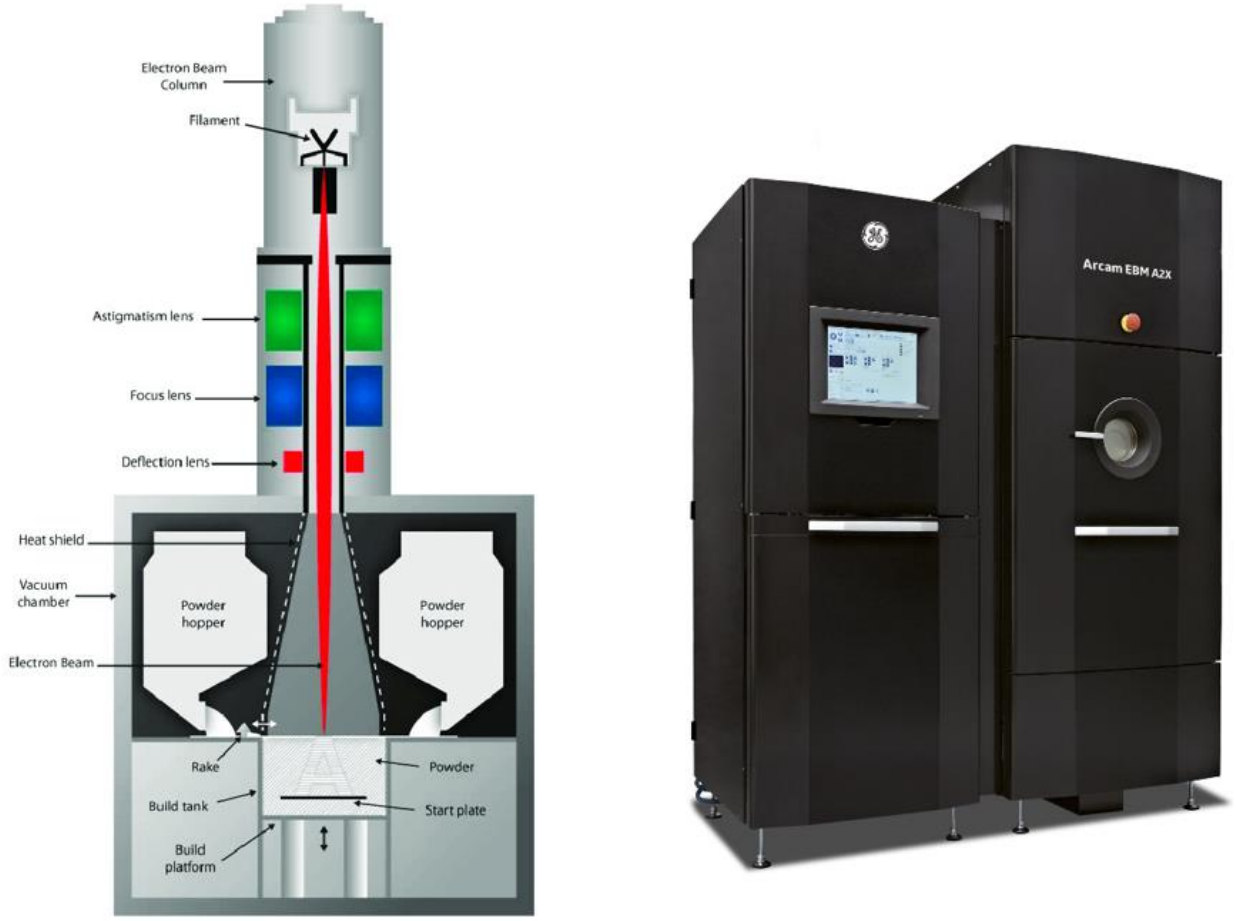

Figure 14: EBM machine systems [34] (left) and Arcam EBM A2X machine [35] (right).

On top of the machine, there is the Electron beam column where the electron beam is generated and adjusted to melt the metals powders. Under it, there is the vacuum chamber, isolated to the environment by a door, where the powder hoppers are placed. The powder hoppers deliver the powder during the process and thanks to the rake the powders are spread over the build tank. Inside build tank, the build platform can slide thanks to the motors and pistons systems. Over it, the start plate is placed but not locked as in the L-

PBF system because with this technique the unfused powder is strongly compacted. The main difference of EBM compared to L-PBF process is the energy source. EBM machine uses a stationary electron beam to melt the powder together instead of the laser. In Figure 15, a sketch of electron beam gun is illustrated[12].

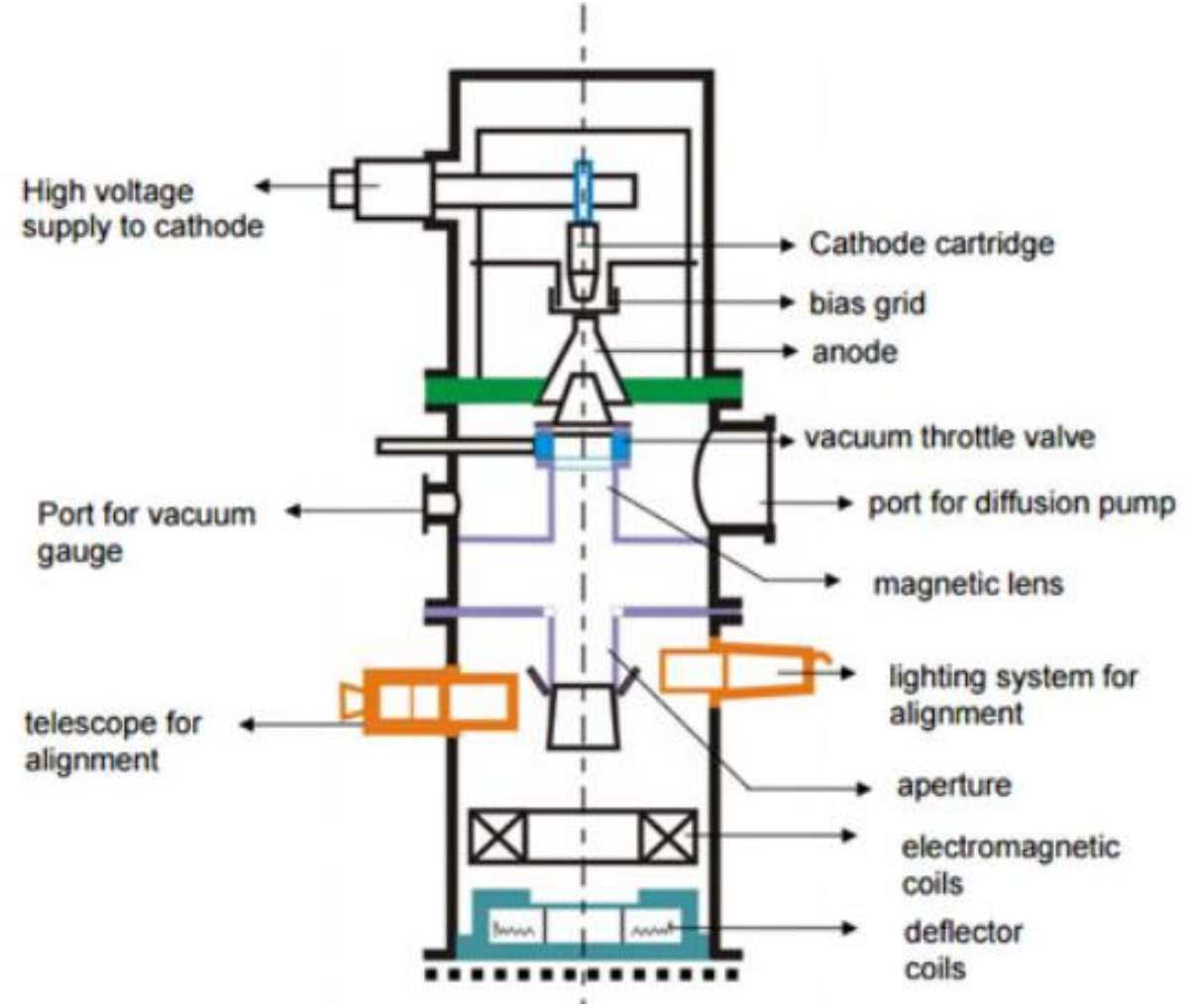

Figure 15: Electron beam gun [36].

John O et al. [22] described the electron beam generation as "A high voltage supply is placed across a grid cup and anode. A negatively charged cathode is heated to boil off electrons in a process referred to as thermionic emission. Those electrons are accelerated at high voltage (60 kV) and focused by the grid cup toward the anode passing through a hole and into a work chamber. In the chamber the charged electron beam is focused using electromagnetic coils and may be directed to locations on the workpiece using magnetic deflection coils to steer the beam. EB equipment can generate beam voltages of 60–150 kV and beam powers of 3–30 kV or more and focus to beam spot sizes of fractions of a millimeter". Inside the electron beam column vacuum is needed because gas molecules can interact or deflect electrons, so turbomolecular pump reduce the gas pressure under 10-5 Pa. There are other auxiliary systems for beam control and analysis, like telescope and lighting system used for beam alignment.

The melting process is provided by the interaction of electron beam and powders. The kinetic energy of accelerated electrons is transformed into heat by the collision between electron and powder, so melt pool appears and powders particles melt together. Compared to the laser-powder interaction, the depth penetration is bigger. This allows to fuse ticker layers. That ability of electron beam increases the productivity, but the energy required for the process is bigger. As L-PBF process, the chamber is isolated, but in this case, no gas is filled because powder oxidation is avoided by the presence of a vacuum. Vacuum also avoids interaction between electron and gas. Other differences compared to L-PBF process are the chamber temperature and the pre-heating process. Thanks to the electromagnetic coils, the electron beam can be widely defocused, so using low power and high scanning speed, layer preheating is possible. The temperature inside the chamber is increased up to 700°C. The chamber temperature depends on the used material. Typically, the temperature is approximately 0.8 time the melting temperature of the powder [29].

This process is used for two main reasons. The first one because it allows to drastically reduce the cooling gap, this induces lower electron beam energy and fewer internal stresses. The second reason is due to the powder diffusion. Internal stresses are due to the rapid solidification of melt pool. High chamber temperature allows to reduce the cooling gap and induce a distension heat treatment during the printing process. At the end the parts are ready to be removed from the platform No stress relieve is required. Powder diffusion phenomena appears for two reasons. The first one is because powder and electron beam can have different charges: electrons negatively charged scatter the powder with a positive charge. For that reason, powder cloud appears and interacts with the electron beam. The second reason is due to the kinetic energy of electrons, which is not completely transformed into heat, so the impact of electrons creates a bowling ball effect, as a ball hitting dry sand. Preheating and high chamber temperature reduce these problems because create a semi dense powder bed. This induces a more powerful cohesion force of powder, so powder diffusion phenomena decrease. For example, when the removing part procedure happens, hammer and chisel can be adopted to separate melted and un-melted powder[4].

At the end of the building process, the working chamber needs to be cooled. This operation is conducted very slowly to avoid internal stress and can take up to ten hours. For this reason, EBM machines are provided with removable build volume to increase productivity. The cooling process is performed outside the machine and a new job can prepared into EBM machine. To improve the cooling process and reduce the electrostatic charge, Helium is filled into working volume. Due to the slow cooling process and high working temperature, grain growth and microstructure relaxation occur. As L-PBF technique, EBM machines use metals in powder form as raw material. Compared to L-PBF technology, the powder size is bigger due to high penetration depth and more powerful source. EBM technique uses powder granulometry from 80 to 150 µm. This induces a more productive system but on the other hand, high roughness and low accuracy part occurs, compared to L-PBF process [22].

Due to the interaction between electron beam and powder, powder needs to be conductive, so the materials option available on market are fewer compared to L-PBF. The main metals used are[33]:

- Titanium Alloy
- Cobalt Chrome
- Stainless Steel
- Aluminum Alloy
- Maraging Steel
- Inconel Alloy

As mentioned before, EBM machines are sold only from Arcam company. Their systems are limited in working volume as in L-PBF technology. Nowadays the machine with the largest working volume is the Arcam EBM Spectral L with cylindrical volume of 350x430 mm.

2.6.2. Direct Energy Deposition Technology

Unlike powder bed technologies, Direct Energy Deposition techniques deposit and fuses the material only where it is needed. Depending on the materials and types of heat source used, there are different typologies of DED processes, which have a similar operating system. The materials can be in the form of powder or wire and the heat generation can be by an electron beam or a laser source. These techniques are the evolution of welding process, in fact they are similar to Tungsten Inert Gas (TIG) process. The most used technique is Laser-DED technique. It fuses the material in powder form and uses laser as energy source. In this paragraph, only L-DED technique will be analyzed. The deposition, in L-DED techniques, is a local process, powder nozzles blow the powder directly on the desired surface and the solidification process can take place. As in TIG process, to avoid oxidation and interaction between the atmosphere and melt pool, a shielding gas flow system is installed on the deposition head. The melting process occurs due the laser-powder collimation in the same area, so welding seam occurs [30]. In Figure 16, a deposition head of L-DED is illustrated.

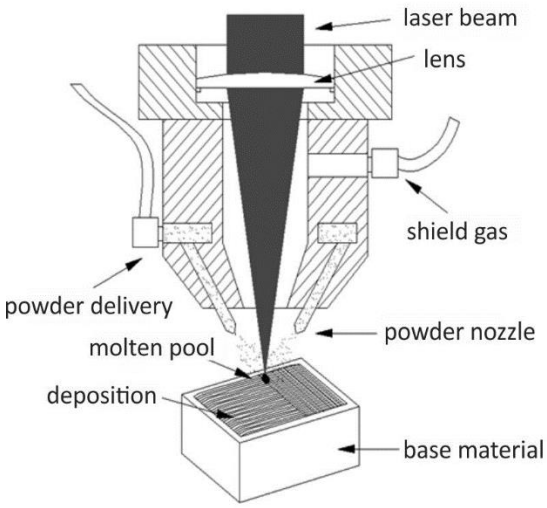

Figure 16: Deposition head of L-DED machine [37]

Laser beam is generated by laser source and it is transported into deposition head by a glass fiber where it is collimated by a lens. Shielding gas is insufflated inside the deposition head and it avoids melt pool oxidation. Powder nozzles are located at the end of head deposition. They blow the powder where laser beam is collimated. The deposition can start from the building platform or on parts surfaces. Nowadays DED machines are five or six axis machines and the deposition head is encourages on a robotic arm. The building platform is locked to a rotating table. It allows to deposit material in every position. These elements are located inside a working chamber that can be filled with inert gas. Deposition process is controlled by a close-loop control system. The geometry, melt pool temperature and composition are analyzed during the process. Thanks to the control system, real time parameters adjustment can be performed. Great possibility of these machines is to realize part with different materials or create metal alloy directly during deposition process. Thanks to

the presence of multiple powder nozzles, generally three or four, different powder can be sprayed from the nozzles, so on the deposition area, new metal alloy composition is created. Another possibility is to change the metal powder during the process to obtain multi materials part. During deposition, not all the particles are melted, due to the powder spray. Particles can be scattered by other particles or to the surface. Figure 17 show the particle scattering phenomena and the L-DED deposition. For this reason, DED machines need a particle recovery system. L-DED technique uses powder with particle size range of 25-45 μm [4].

Figure 17: L-DED deposition process and particle scattering [38]

Any type of material or mixture of powders that are sufficiently stable to form a melt pool can be used in DED techniques. Materials that are very difficult to process are those with high thermal conductivity and high reflectivity, such as some Aluminum alloys, gold and copper. These materials, due to their characteristics, can reflect the laser beam and in some cases even cause internal damage to the machine itself. An important aspect of DED process is the shielding gas flow. The gas pressure above the melt pool must keep constant during the deposition process because the melt pool may be oxidized. For this reason, many analyzes were conducted at different head deposition velocity and gas flow-velocity curve were obtained. In some L-DED machines, the shielding gas flow does not allow properly deposition with certain materials, so the deposition chamber is filled by Argon or Nitrogen, depending on the reactivity of materials [23].

Unlike the other MAM technologies, DED machines have bigger working volume, so this allows to create much larger objects and it makes this technology suitable for part repairing. This advantage is correlated to local process approach. For example, the bigger Prima Industrie DED machine has a 4140 x 2100 x 1020 mm working volume. Other advantage of local process approach is that some CNC machines can become DED

machines only changing the CNC tool with the deposition head. Prima Industrie, DMG Mori and Optomec are the main sellers of DED machines.

On the other hand, there are some disadvantages compared to other MAM technologies. The main disadvantage is the combination of low resolution and high surface roughness. This induces also a productivity limit because any action aimed to increase productivity would result in a reduction of resolution. Another disadvantage is the geometry limits due to the impossibility of DED technique to realize supports, so undercuts and other specific features can not be created. For these reasons, machining is required.

Automotive, Aerospace and Oil&Gas fields are the main sectors of DED technologies.

2.6.3. MAM techniques comparison

Regarding the main MAM techniques, Table 2 analyses the main aspects of the technologies to understand their applications and differences.

Table 2: MAM techniques comparison [39] [40][41]

	EBM	**L-PBF**	**L-DED**
Thermal source	3-4 kW	100-1000 W	2-3 kW
Atmosphere	Vacuum	Inert gas or vacuum	Inert gas
Build rate	55-80 cm3/h	5-20 cm3/h	7-70 cm3/h
Tolerance	±0.4 mm	±0.2 mm	±0.1–0.2 mm
Powder bed temperature	700-1000°C	30-250°C	/
Layer thickness	50-200 µm	20-100 µm	20-100 µm
Scanning	Deflection coils	Galvanometers	3-axis robot arm
Scan speed	<8000 m/s	<8 m/s	/
Surface roughness	Ra= 25-35 µm	Ra= 11 µm	Ra = 11 µm
Materials	Conductivity limited	Polymers, ceramics, metals	Metals
Powder particle size	80-150 µm	20-60 µm	150-300 µm

2.7. MAM materials

Nowadays a wide range of metals are available for Metals Additive Manufacturing technologies, the main alloys are:

- Aluminum alloys
- Titanium alloys
- Nickel alloys
- Fe-based Alloys
- Cobalt Chrome alloys

2.7.1. Aluminum alloys

Aluminum alloys are the most used light alloys, due to their high strength-to-weight ratio, high casting, characteristics and good corrosion resistance. The most common alloys are AlSi10Mg and AlSi12Mg[42][43], they are relatively easy to process due to their small solidification interval and low coefficient of thermal expansion compared to normally thermo-mechanical aluminum alloys. For high strength applications, a hardenable Al-Mg-Sc alloy is proposed by Schmidtke et al.[44] The addition of Sc enables precipitation hardening by the formation of Al3Sc precipitates and grain refinement in AlMg alloys. Another aluminum alloy used in additive manufacturing applications is Al6061, which has properties similar to 7000 alloys, i.e. good mechanical properties, superior to most alloys and excellent corrosion resistance. Typical applications are in the automotive field. A357 alloy is also largely used in the AM field for low stress applications.

Another important alloy is Scalmalloy. In this alloy, silicon is replaced by scandium which gives excellent mechanical properties, far superior to normal Al alloys. For this reason, Scalmalloy is widely used in the aeronautical field where the specific properties play a major role.

2.7.2. Titanium alloys

Ti and Ti alloys are very interesting in AM field. Ti Alloys are used in many industrial applications and they present high machining costs and long lead times. For this reason, titanium alloys have been widely used in AM applications. The most widely used Ti alloy is Ti-6Al-4V, which has different microstructures depending on the printing technology used. W. Xu et al[21], reported that SLM can result in either fully martensitic (α') or fully lamellar α/βphases; EBM can have lamellar α/β, α', massive α grains or non-lamellar α and β phases[45]; LMD can achieve α'+partially decomposed α' phases[46].

Other Ti base alloys that have been developed are alloys with a higher content of alloying elements, such as Ti51Al42V6Cr1[47] and Ti-Al-Mo-V-Cr-Fe[48]. Titanium alloys are widely used in the aeronautical and biomedical fields due to their excellent mechanical, physical and biocompatibility properties.

Very important for the aeronautical field are Ti-Al alloys, which are used to make turbine blades. Their main characteristics are low density, and therefore high specific properties, good creep resistance and good mechanical properties. The two main alloys are Ti-3Al and Ti-Al.

2.7.3. Nickel Alloys

Ni-based superalloys usually have very poor machinability due to their low thermal conductivity and high hardness. These alloy's disadvantages make Ni based superalloys available for the AM application because near net shape components are produced with AM technologies, so machining is reduced. The most used Ni based alloys are the Inconel 718, Inconel 725 and Hastelloy-X, due to their mechanical and creep resistance at high temperatures. These alloys are used extensively in the aeronautical field for the manufacture of turbine discs. Ni based alloys require post processing treatments, such as HIP and aging, to obtain tensile strengths similar to those of cast products[30].

2.7.4. Fe-based Alloys

Iron-based alloys and steels are one of the most popular alloys for metal AM, including stainless steels and tool steels. The most widely used alloys are 316L, or 304L due to their excellent ductility and corrosion resistance, they are widely used in applications involving water, such as marine, culinary, pharmaceutical and dental. Other iron base alloys used are 18Ni-300, as maraging steel, 17-4 PH, as precipitation hardenable stainless steel, and H11/H13, as tool steel [30].

2.7.5. Cobalt Chrome alloys

This class of super-alloys presents high strength, superior corrosion resistance, non-magnetic behavior and good biocompatibility. Co28Cr6Mo is the most used. This is an alloy commonly used for surgical implants due to its high wear-resistance and nickel-free (< 0.1% nickel content) composition. It is also used for engine components, wind turbines and many other industrial components as well as in the fashion industry to make jewelry[49].

2.8. Significance of laser beam focus variation on the quality of the printed components

The laser generates convergent-divergent laser beam. The laser beam spot can be controlled in two ways. The first one is varying the distance between focal lens and target, so define the defocus distance. The second one is using a beam expander.

Defocus distance approach is more popular. In L-PBF machine, the focal lens is called θ lens, and the target is the substrate, where melt occurs. θ lens collimates the laser at a fixed distance from itself, in which condition the laser focus is minimal. The focal plane is defined as the plane in which the focus occurs. The defocus distance corresponding to the distance between the focal plane and the substrate. It can assume positive or negative value, and this corresponds to a divergent and convergent laser beam, respectively. Due to the symmetry of the laser, equal values of defocus distance, in absolute value, corresponds to the same laser beam spot size. In figure 18, the laser beam characteristics are shown.

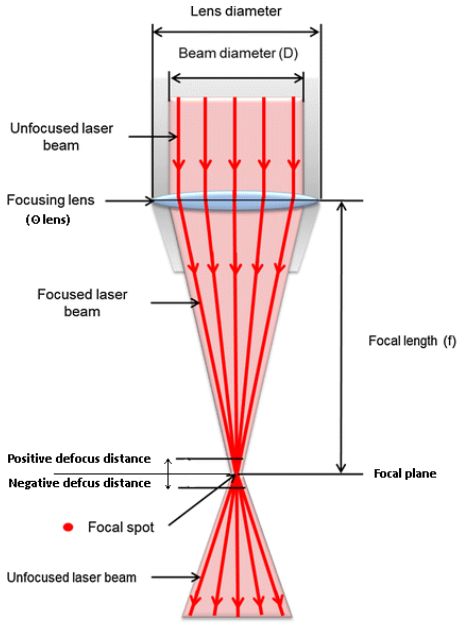

Figure 18: Laser beam characteristics

Varying the laser spot size affects two main aspects of the powder-material interaction. First of all, it changes the behavior of melt-pool. Melt-pool changes from keyhole to conduction mode or vice versa. The second aspect is the changes in VED (Volume energy density), namely the intensity per volume unit of laser energy absorbed by material.

2.8.1. The effect of VED

VED is one of the most affecting parameters in L-PBF. In general, it is calculated, as Formula 1 [50]:

$$VED = \frac{P}{v \cdot h \cdot d} * 10^6 \quad \left[\frac{J}{mm^3}\right] \quad (1)$$

P is the laser power [W], v is the scan speed [mm/s], h is the hatch distance [µm] and d is the layer thickness [µm].

This description does not take into account the effect of variation of the laser spot size. Many researchers conducted studies about this topic, and different relations were born to describe this interaction. One of these is reported in Formula 2[51]:

$$VED = \frac{P}{v \cdot d \cdot t} \quad \left[\frac{J}{mm^3}\right] \quad (2)$$

P is the laser power [W], v is the scan speed [mm/s], d is the diameter of the laser spot [mm] and t is the layer thickness [mm].

Overall, all the relations describe a decrement in VED associated to an increase of laser beam size, at same laser power. This behavior is expected, that's why the energy of the laser is distributed on a bigger area/volume. As the laser spot is linked to the defocus distance, a variation of defocus distance from zero, either positive or negative, leads to a VED reduction. The reduction of VED also induces a reduction in temperature and so in the thermal gradient of the melt pool. Varying the thermal gradient of the melt pool can induce a change in the microstructure and/or in the defects[51].

Different studies analyze the effect of defocus distance in samples made by L-PBF. The researchers describe an increase of unfused defects when VED reduction occurs. This behavior is explained by the insufficient energy provided to the powder. The melt pool does not penetrates enough the substrate to recast the underlying layers and melts all the powder[52].

2.8.2. The effects of melt-pool behaviors

Two main melt pool conditions occur during powder melting: the conduction mode and the keyhole mode. They are separated by a transaction mode with characteristics of both the melting conditions. The melt pool behaviors are correlated by the laser beam nature, namely by the convergent or divergent laser beam. Conduction mode occurs when the laser beam is divergent. This type of interaction allows the formation of a stable melt pool with a homogeneous thermal gradient. In the other hand, Keyhole mode occurs when the

laser beam is convergent. In this case, the melt pool is less stable compared to the Conduction mode, and the thermal gradient has a preferential direction. Overall, the melt-pool behavior affects three characteristics of the part produce with PBF technology: (i) Melt pool boundaries, (ii) Relative density and defects, (iii) Refusion and overlapping[52][53].

The convergent/divergent nature of laser beam, and so the melt pool behavior, has a straight influence on the morphology of the melt pool. As describe in L-PBF paragraph, the geometrical parameters of melt pool are the width and the penetration depth. In conduction mode, the melt pool has a semi-circular shape, so with aspect ratio near one. This morphology allows to have heat dissipation without a preferential direction. On the other hand, the keyhole mode has aspect ratio strongly different to one. Also, the melt pool has a preferential direction along the building direction, so higher penetration depth occurs. This morphology provides a preferential heat flow direction[53][54].

The melt pool behavior has a strong effect on the defects and so on the relative density. The conduction mode is preferable because allows having fewer defects, compared to keyhole mode. Using a convergent laser beam, the absorbance of the material increases drastically, so high thermal gradient and high temperature appear in melt pool. This produces the formation of macro-pores and cracks, respectively due to the evaporation of low melting material and high thermal gradient. In conduction mode, the defects are only unfused defects due to the low energy density provided[52].

The last characteristics affected by melt pool behavior are refusion and overlapping. Keyhole mode is affected of higher penetration depth, this induces more layers refusion. For that reason, low-melting material evaporation is more critical, compared to conduction mode. The overlapping phenomena is present in both conditions. A change in defocus distance is related to higher laser beam size, so higher overlapping phenomena occurs. Overlapping, as refusion, induces more evaporation of low-melting material and so composition variation of the final part[55].

2.9. AlSi10Mg for L-PBF

AlSi10Mg is a hypo-eutectic casting alloy widely used in AM fields thanks to its castability and stability. This alloy offers good strength and hardness. For this reason, it is therefore used for parts with thin walls and complex geometry subjected to high loads, as in the aerospace and automotive industries. As Al-Si phase diagram shows (Figure 19), the percentage of Si is higher than the solubility limits at room temperature. This characteristic allows having high casting characteristics and high laser absorption. Another important characteristic is the near eutectic composition that allows to control the material shrinkage and induces a low solidification range. AlSi10Mg alloy can be heat treated thanks to the presence of Si and Mg that induced the precipitation of Mg2Si[56].

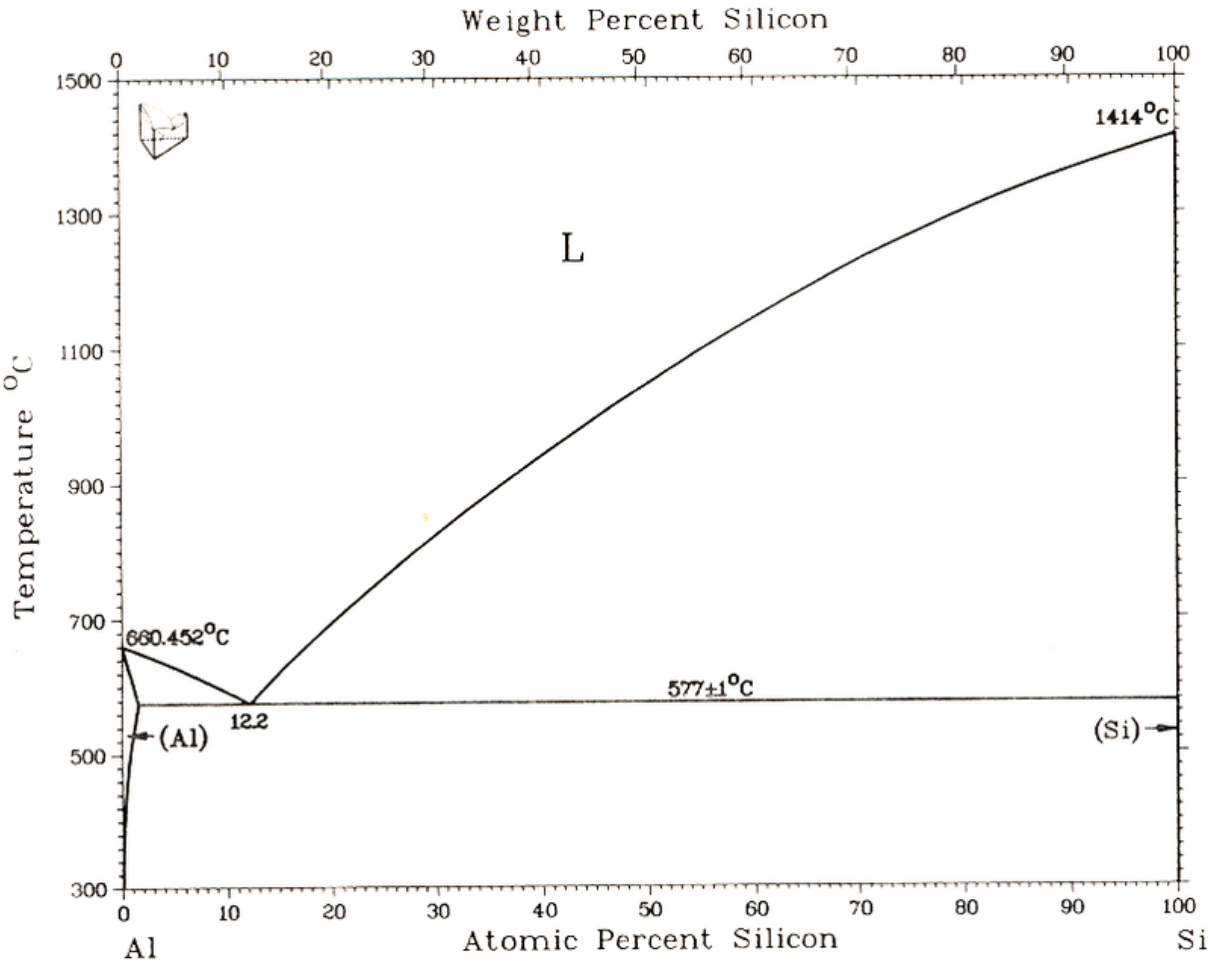

Figure 19: Al-Si phase diagram [57]

The AlSi10Mg L-PBF powder is realized by gas atomization. Typically, it does not have any specific defects, but sometimes the powders have satellites with a discrete tendency to detach. Another defect that can be found, is the presence of micro-cracks on the surface, it is due to the presence of a thin layer of oxide surrounding the powder. Thanks to the high presence of Si, the powder granulometry after the gas

atomization process is very useful for AM technology because Si allows having spheric powder with a similar size and so high flowability propriety. In Table 3, an indication of AlSi10Mg composition is provided.

Table 3: Chemical composition of the AlSi10Mg powder used for the additive manufacturing industry supplied by EOS, SLM Solutions and RENISHAW[58].

AlSi10Mg composition		
Element	**Minimum** (wt %)	**Maximum** (wt %)
Al	/	*Balance*
Si	9	11
Fe	/	0.55
Cu	/	0.05
Mn	/	0.45
Mg	0.2	0.45
Ni	/	0.05
Zn	/	0.1
Pb	/	0.05
Sn	/	0.05
Ti	/	0.15

Thanks to L-PBF process, the microstructure of final part is very fine and do not obtainable with conventional casting process. Due to the fine dimension of melt pool, the cooling rate is very high and so grain growth is inhibited. Generally, the microstructure of an as-build part produced by L-PBF is a cellular-dendritic structure consisting of an α-Al matrix surrounded by a network of eutectic matrix with very fine fibrous Si[59] (Figure 20).

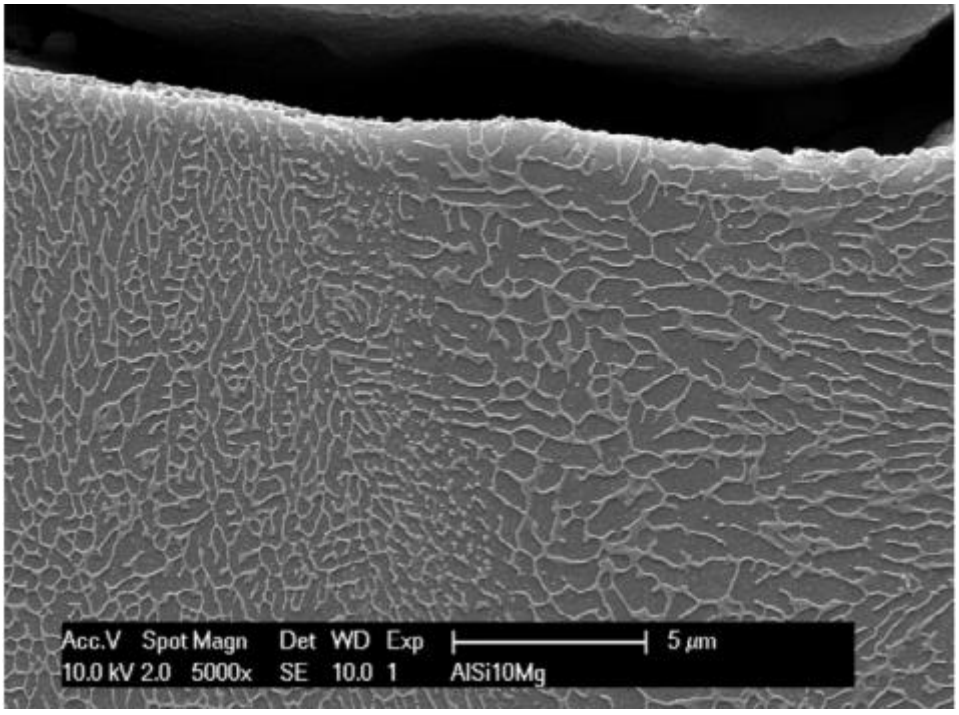

Figure 20: SEM micrograph of a AlSi10Mg SLM part [60]

The large-scale microstructure of the samples is characterized by spherical melt pools elongated in the building direction (Figure 21). Across the melt pool, three zones could be differentiated by the morphology and size of the cellular-dendrites, on both longitudinal and transverse cross sections[61][62]. These are:

- Fine zone, situated in the center of the melt pool. The cellular-dentrides structure grown toward the center of laser tracks and their width is about 500 nm.
- Coarse zone, situated at the border of the melt pool. The width is about 10 µm and the primary α-Al is equiaxed. No significant growth direction is observed.
- Heat affected zone, situated outside the coarse zone. Its width is about 2-3 µm.

The different zones (Figure 21) are due to the heat dissipations. The highest temperature is obtained in the center of melt pool thanks to the gaussian energy distribution of the laser, so a fine grain zone occurs.

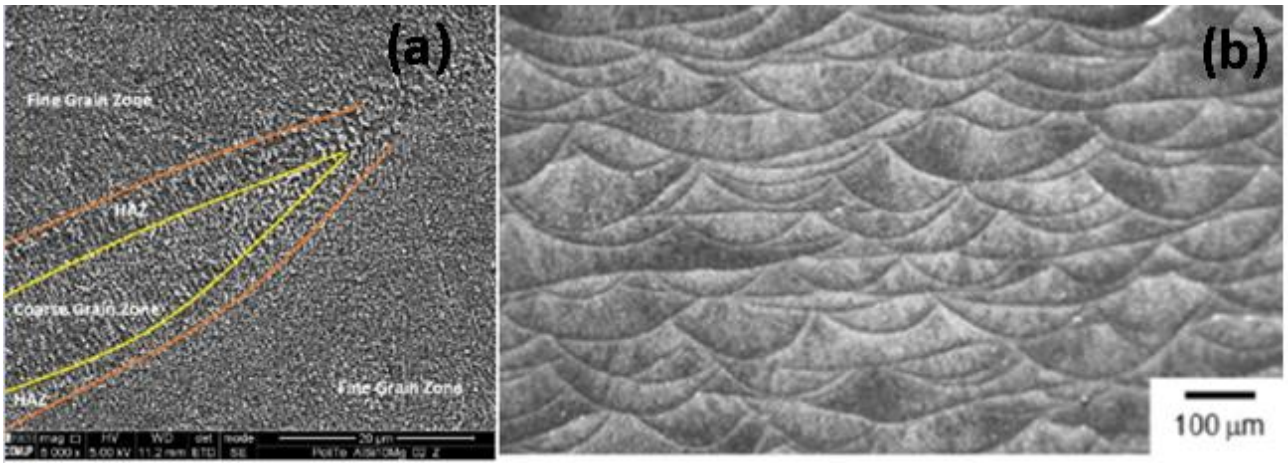

Figure 21: Morphology of the melt pool (a) [62] and Cross section optical micrographs (b) [56] of AlSi10Mg as - fabricated sample produce by L-PBF

Vary post processing treatments can be adopted to improve some characteristics of parts produced in AlSi10Mg by L-PBF technique. The most interesting articles about it are following reported.

- N. Takata et al.[56], conducted a study on the microstructure and mechanical properties after heat treatment of SLM-produced AlSi10Mg alloy samples. Cubic samples were obtained and annealing treatment (300° for 2h) or solution treatment (530° for 6h) were conducted. The microstructure of the as-built sample agrees with that described above, while after treatment at 300° the Si particles are enlarged and the Si diamond phase precipitates within the α-Al matrix. After treatment at 600°, it was not possible to observe the melt pools, moreover the Si particles enlarged and an intermetallic phase (β-AlFeSi) with a rod-shaped morphology was formed. Figure 22 show a graphic representation of the microstructure in as-build and after heat treatment of the samples. The mechanical properties of the samples are reported in Figure 23, there is a reduction in both hardness and tensile strength but a greater elongation at break

after heat treatment. The high reduction in tensile strength was associated with the destruction of the fine structure within the α-Al grains.

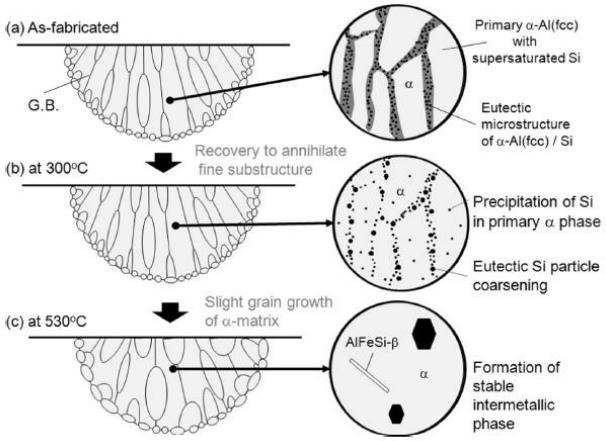

Figure 22: Graphic representation of the microstructure in as-build and after heat tretament AlSi10Mg samples [56].

Table 4: Mechanical characteristics of as-build and after heat treatment AlSi10Mg samples. X-Y proprieties for sample build along the building platform and z properties for sample build along the growing direction [56].

Condition	Yield Stress [MPa]		Ultimate Tensile Strength [MPa]		% Elongation	
	X-Y	Z	X-Y	Z	X-Y	Z
As-build	279	220	475	476	7.5	5.5
Annealed at 300° for 2 h	180	175	285	290	18.6	14.2
Solution treated at 530° for 6 h	153	139	269	245	18.3	18.1

- W.Li et al [61], conducted a study on the influence of solution and artificial aging heat treatment on the microstructure and mechanical properties of samples made of AlSi10Mg using the L-PBF technique. Treatments were carried out at 450°, 500° and 550° for 2 h followed by water quenching. One half of the samples were also subjected to artificial aging treatment at 180° for 2 h followed by quenching. The resulting microstructure of the as-built samples is cellular-dentritic with a network of Si in primary α-Al matrix, in agreement with the previous description. All the heat-treated samples, observed an enlargement of the Si particles and a reduction in their number within the α-Al matrix. The latter effect is due to the reduction of Si solubility in the α-Al matrix, i.e. eutectic Si is rejected by supersaturated Al (Figure 23). During this phenomenon, Si particles can react with Mg particles to form the Mg2Si phase, which is associated with an increase in strength in Al-Si-Mg alloys. The increase in Si particle size, on the other hand, is due to Ostwald ripening, i.e. the phenomenon of coalescence of particles at the expense of smaller ones. As in the study analyzed above, the as-built samples have the greatest characteristics in terms of UTS and YS but the least in terms of ductility (Figure 24). After the heat treatment, a reduction in both UTS and YS is observed due to the destruction of the very fine Si networks. The increase in ductility, on the other hand, is due to two factors. The first is the increase in the size of the Si particles and the

second is the reduction in internal tension due to the heat treatment. The hardness trend is in line with that of the UTS.

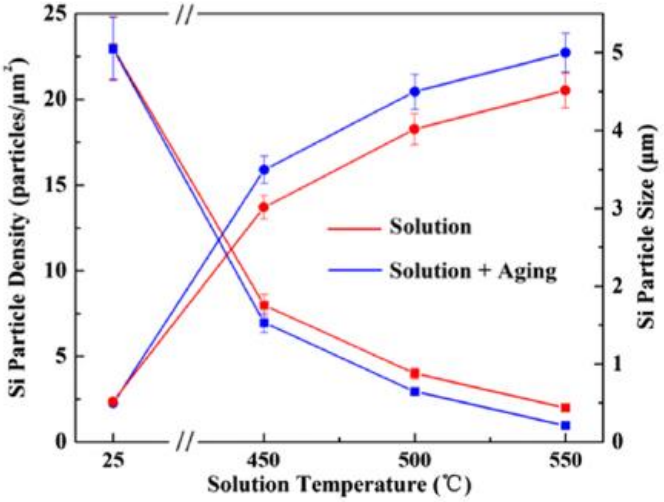

Figure 23: The Si particle density and size as a function of solution and artificial aging temperature [61].

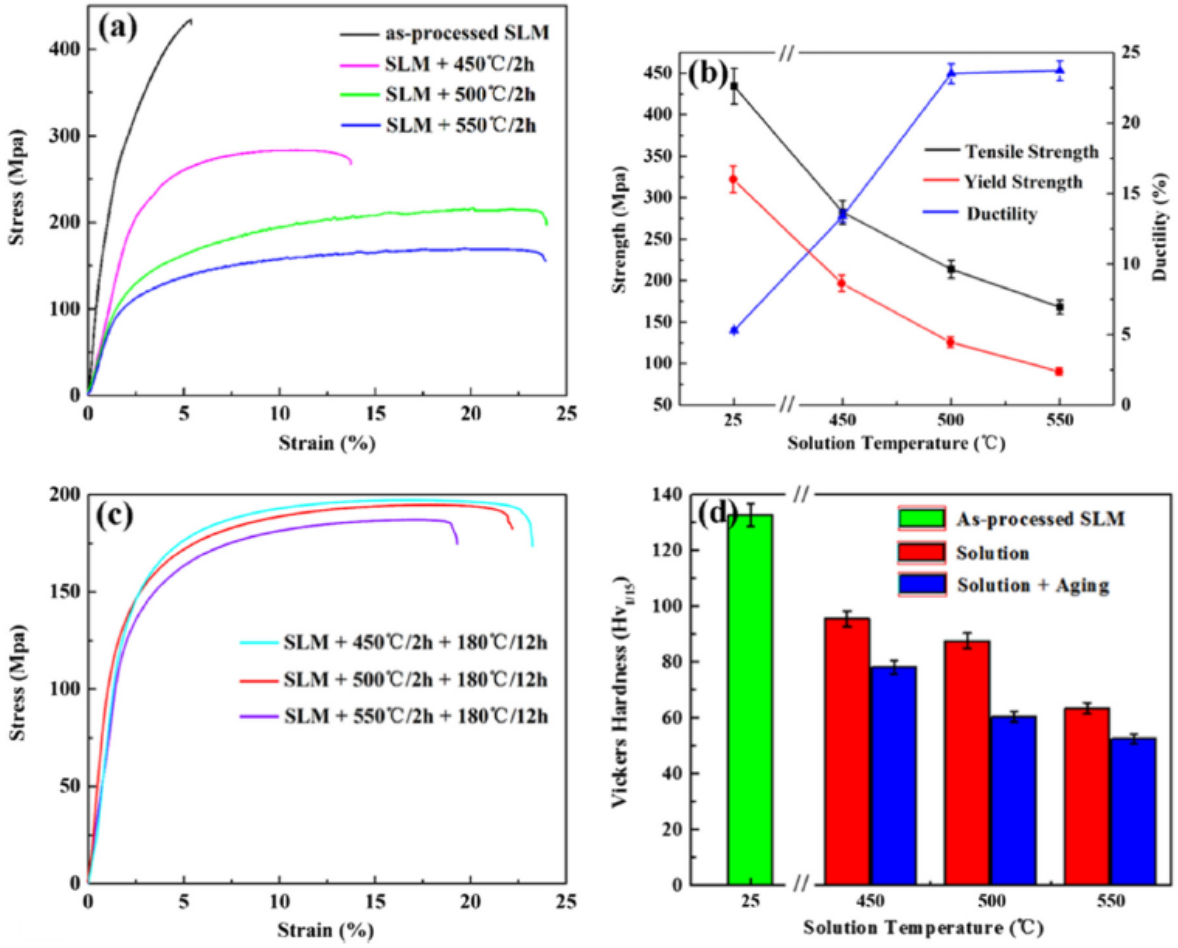

Figure 24: (a) Room temperature tensile stress-strain curves of the as-built SLM samples that solution heat-treated at different temperatures; (b) corresponding mechanical data; (c) tensile test stress-strain curves of the solution artificial aging specimens; (d) the Vickers hardness of the as-built and heat-treated SLM specimens [61].

- L. Thijs et al [63], conducted a study on the influence of scanning strategies on the microstructure and texture of samples made of AlSi10Mg using the L-PBF technique. The influence of scanning methods was taken into account by comparing unidirectional and bidirectional scanning strategies. The influence of rotation of the scanning strategy and the so-called “island scanning” strategy also are taken into account. The scanning strategies analyzed are shown in Figure 25.

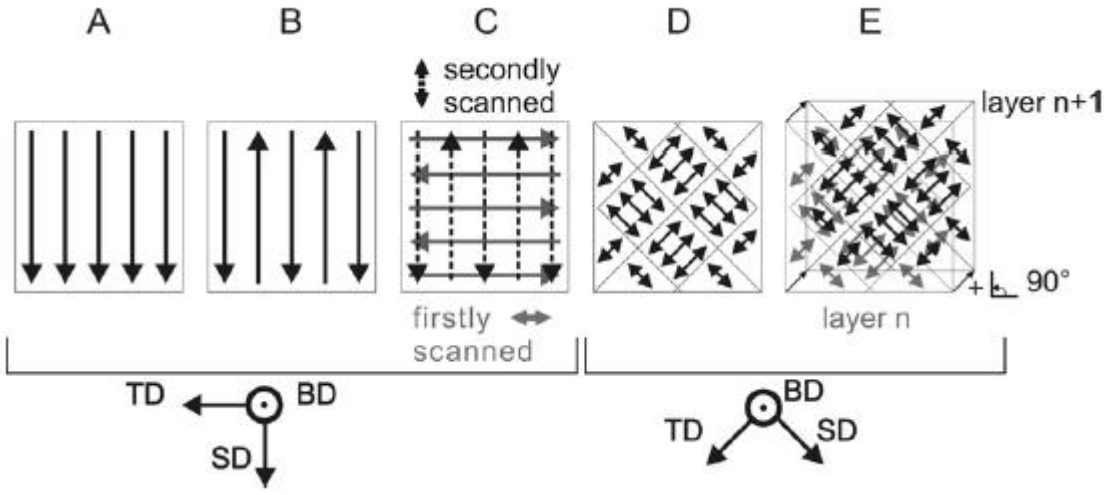

Figure 25: Overview of the scanning strategy used for the different samples. The building (BD), scanning (SD) and transverse direction (TD) are indicated. Sample A is scanned with long unidirectional vectors; sample B with long bidirectional vectors; sample C is is first scanned with long bidirectional vectors in TD and secondly scanned with long bidirectional vectors in SD; sample D is scanned with island strategy with 90_ rotation but without shift and sample E is scanned with island strategy with 90_ rotation and 1 mm shift between the layers [63].

A fine microstructure with micro grains with preferential <100> direction and fcc Al cells decorated with a 'diamond' Si phase was obtained. Several variations in texture were detected. With A type scanning strategy, a high <100> texture along the scanning direction and a weak <110> texture along the growth direction of the part were detected (Figure26). The normalized texture difference was calculated to analyze the texture differences. This parameter was calculated for all strategies and obvious differences in texture were detected between samples C and A, D and A. For samples A and C, a 35% reduction in the normalized texture difference was detected. This means that the rotation of the scanning direction induces a considerable reduction of the fibres aligned along the scanning direction but maintaining the same weak texture along the growth direction. Another significant change in texture was observed when changing the strategy from uni-directional to 'island scanning'. A greater reduction was achieved compared to sample C, i.e. a more isotropic texture was obtained. The texture variation of sample E compared to sample D is 1%, therefore negligible. No significant texture variation was observed when using uni- or bi-directional scanning.

An analysis of the texture along the direction of growth in sample E was carried out. It does not show texture variation along the direction of growth, that's why no large scale growth mechanisms occurs.

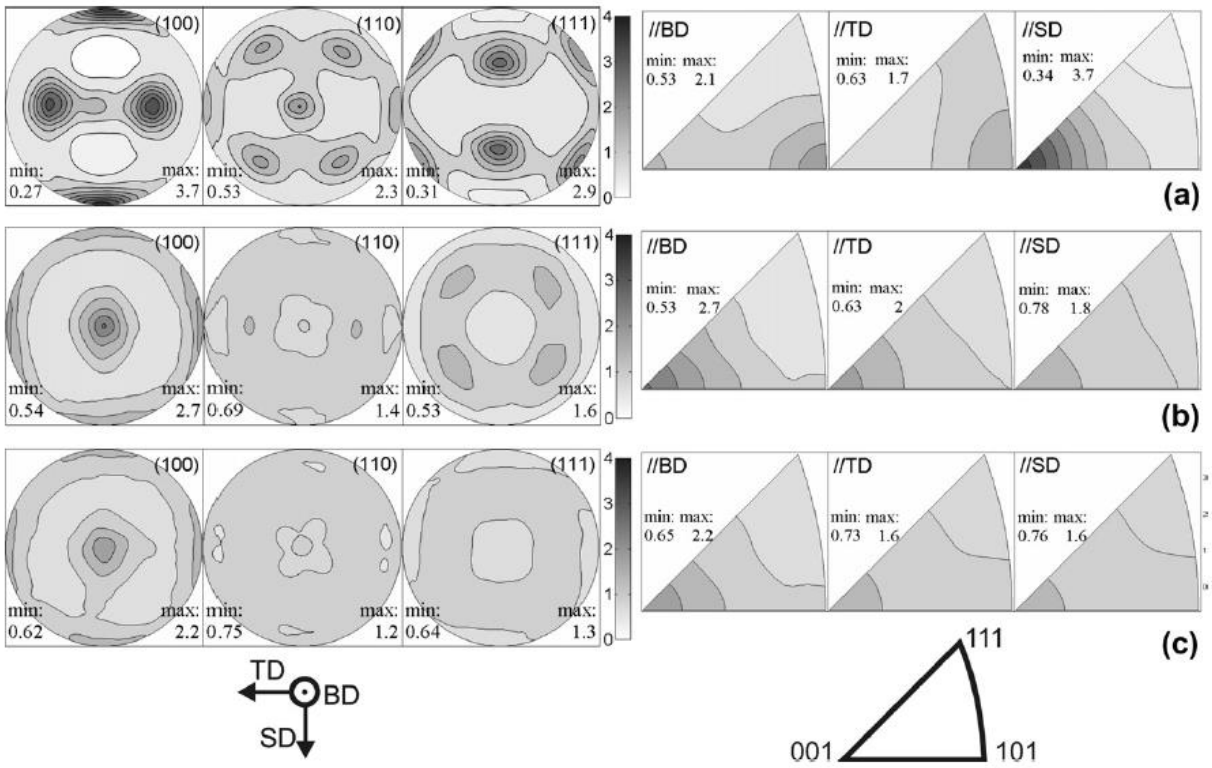

Figure 26: Pole figures and inverse pole figures for AlSi10Mg SLM parts produced using different scanning strategies. The (100), (110) and (111) pole figures (left) and inverse pole figures (right) parallel to the building direction (BD), scanning direction (SD) and the transverse direction (TD) are given. Figs are shown for a sample produced with: unidirectional long scanning vectors (sample A) (a); bidirectional long scanning vectors rotated 90 (sample C) (b) and island scanning without shift (sample D) (c). Furthermore, the orientation of the specimen coordinate system is shown and the relative intensity of the diffraction peaks compared to an isotropic powder material reference sample is indicated by the grey scale[63].

3. Material and Methods

3.1. Samples Modelling

The realization of the samples was obtained with the collaboration of Prima Industrie SpA. In its factory the CAD files were realized, and the building process was done. The activities started from the realization of the CAD file: 6 tensile test speciments and 3 cubes for each job were realized. In Figure 27, the nominal dimensions of the samples are shown.

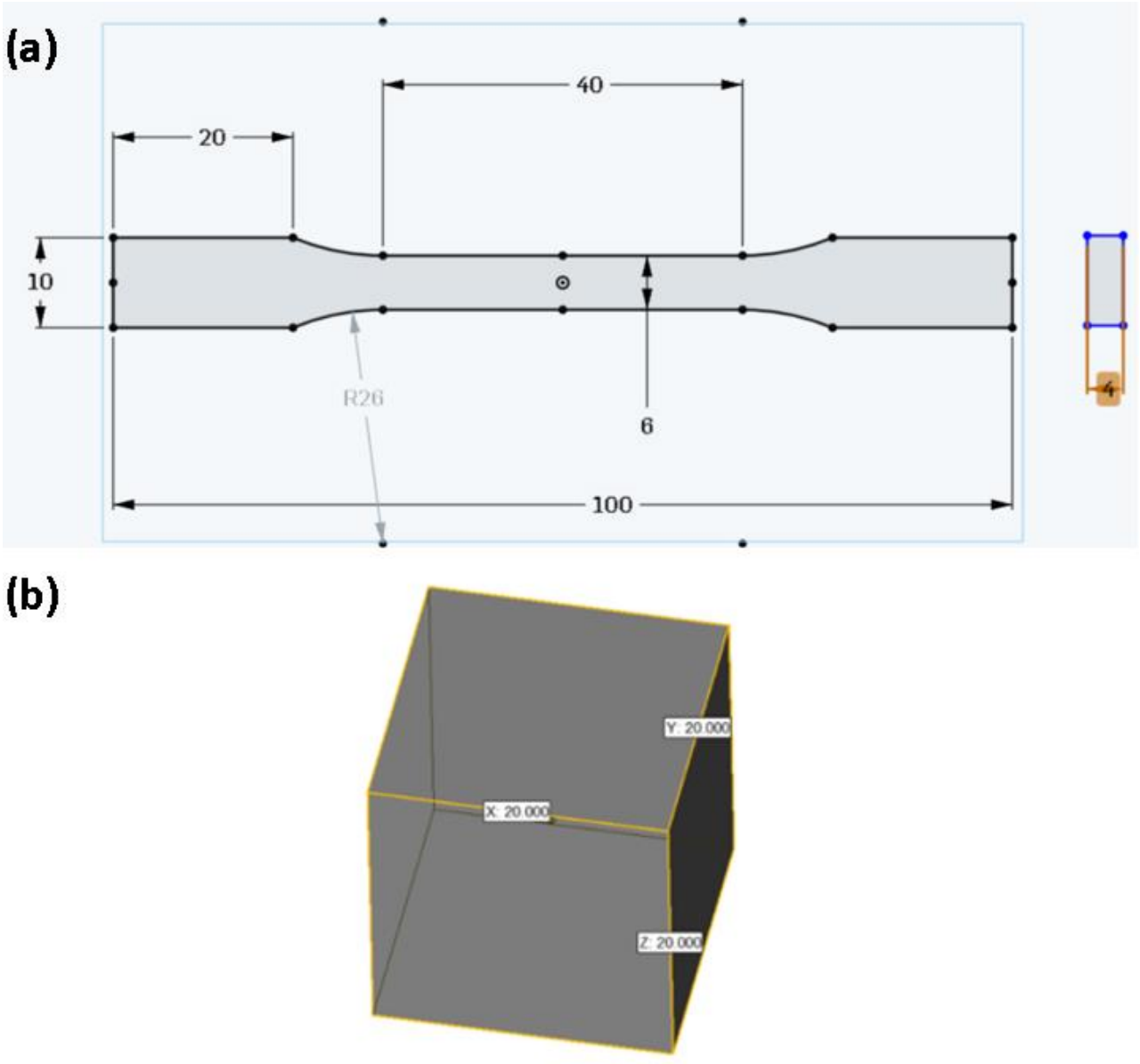

Figure 27: Nominal dimension of the samples.(a) Tensile test speciment, (b) cubic sample.

The machine file preparation was carried out using Materialise Magics software. The tensile specimens were printed according to two different strategies, one with the longitudinal direction of the specimen orthogonal to the growth direction and inclined by 45° to the y-axis of the printing plane. The second strategy involves positioning the specimen with longitudinal direction parallel to the growth direction. These different orientations were chosen to evaluate only the anisotropy phenomenon separating it from a possible preferential direction (x or y). In Figure 28, the location of samples into the working volume is shown.

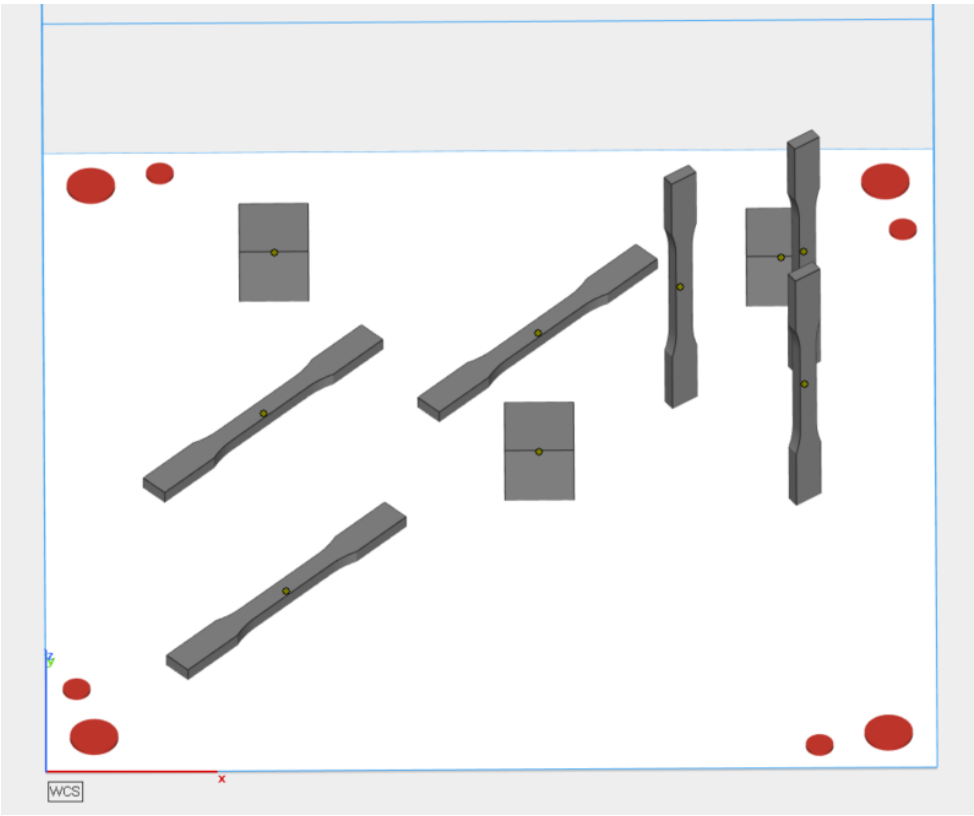

Figure 28: Location of the sample into the working colume.

Subsequently, through the software of Prima Industrie, the STL file underwent the slicing process. The definition of the process parameters was obtained in the previous step, standard Prima Industrie machine parameters were used.

3.2. Samples Building

Samples were realized by PrintSharp 250, its characteristics are reported in Appendix A.

AlSi10Mg powder by Carpenter Additive was used to fabricate the samples. All specimens were constructed using recycled powder through the sieve. The characteristics of the powder are shown in Table 5.

Table 5: AlSi10Mg Carpenter Additive powder characteristics. In blue the chemical composition, in green the powder properties [64].

Aluminium (wt. %)	Balance
Nitrogen (wt. %)	0-0.10
Copper (wt. %)	0-0.05
Tin (wt. %)	0-0.05
Lead (wt. %)	0-0.05
Titanium (wt. %)	0-0.15
Zinc (wt. %)	0-0.1
Silicon (wt. %)	9.0-11.0
Nickel (wt. %)	0-0.05
Manganese (wt. %)	0-0.1
Magnesium	0.25-0.45
Iron (wt. %)	0-0.4
Oxygen (wt. %)	0-0.1
Granulometry [2]	<63µm

The samples were made using the "stripe" scanning strategy. This scanning strategy involves a series of unidirectional scans with "hatch distance" and defined field width and angle. These last two parameters are defined as "field width" and "hatch angle" respectively. The "hatch angle" parameter is defined as the angle formed by the stripe and the Y axis of the machine. The "field width" is define as the length of each series of unidirectional scan. It is possible to scan the layer by two alternate unidirectional scanning strategies called "White area" and "Black area", and associate different process parameters. Between one unidirectional scan and another, a section area is not scanned. This section has a width defined by the "Field overlap" parameter. The edges of the part are fused multiple times, typically twice, at a distance defined by the "Filling offset" from the nominal edge of the part.

The scanning strategy of successive layers is rotated counterclockwise, therefore, the “Field angle” parameter, defined as the angle between the stripe and the Y axis, varies during the process.

The construction of the samples was obtained keeping the same parameters of "White area" and "Black area".

[2] ASTM B214

In Figure 29, a sketch of the “Stripe” scanning strategy is shown.

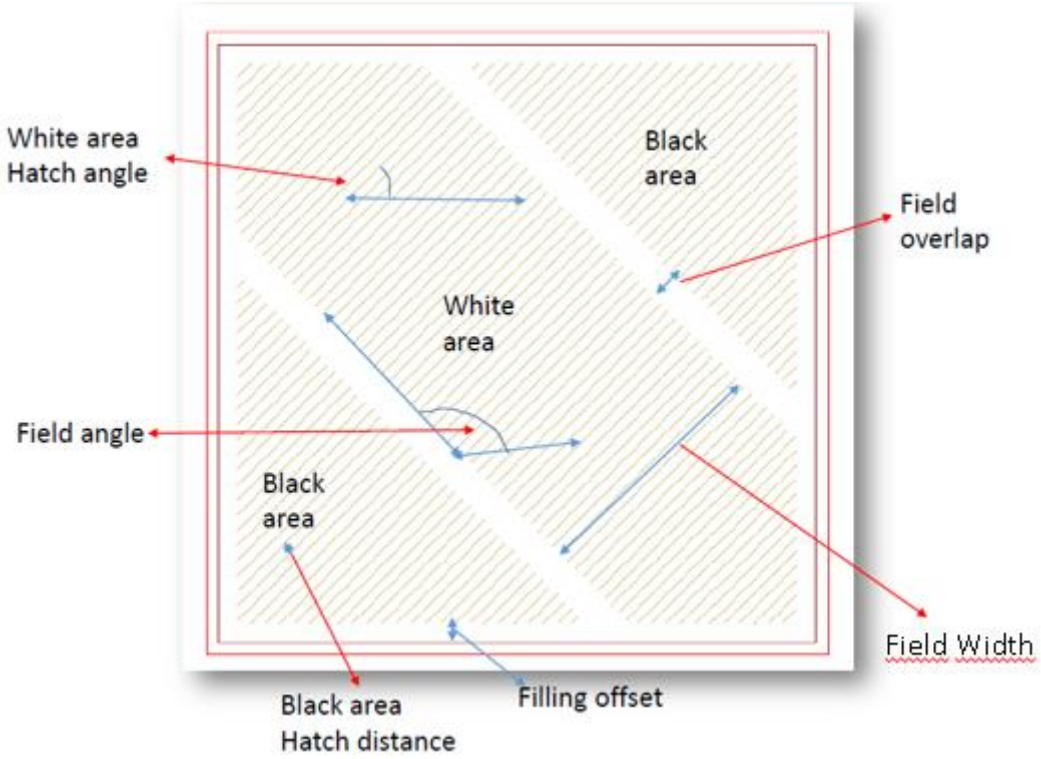

Figure 29: Sketch of Prima Industrie SpA scanning strategy [65].

Before making each job, an evaluation of the focus was carried out. Three job were realized with the same machine file, machine condition and process parameters. Only focus was changed. Samples were made with defocus distance: -1.5, 0, +1.5 mm. The change of laser focus was obtained by modifying the laser collimator.

In Figure 30, the samples encourage to the building platform, after the building process, are shown.

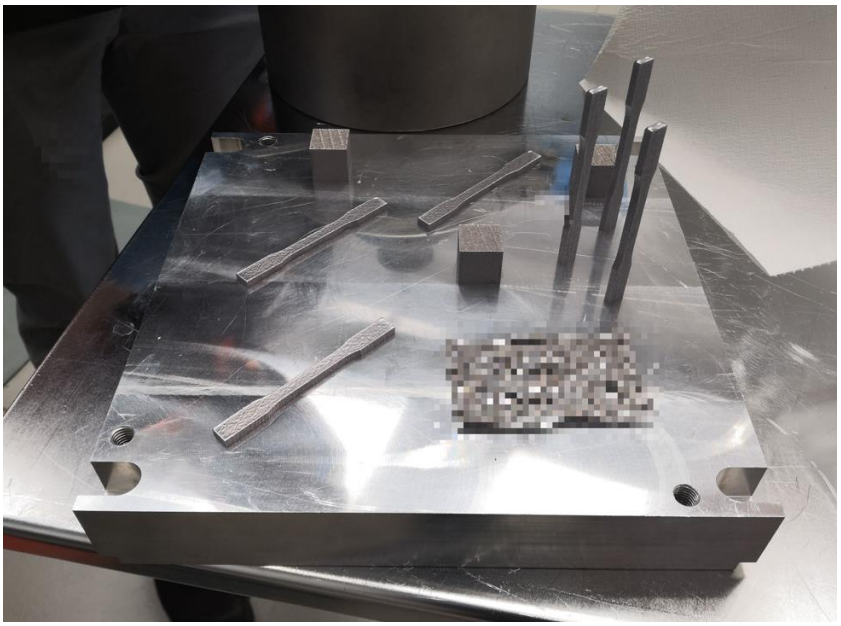

Figure 30: Sample after building process.

At the end of the construction process, each job was removed from the working chamber and cleaned. A focus check was then carried out. Finally, the samples were cut from the plate using wire-EDM, sorted by type and numbered. Each sample was numbered from 1 to 9, the samples numbered 1 to 3 were obtained with a defocus distance of -1.5 mm, the samples numbered 4 to 6 were obtained with zero defocus distance, the last samples were obtained with a defocus distance of +1.5 mm. The directions of the machine axes were also engraved on the samples. The x-axis corresponds to the direction of the recoater, while the z-direction coincides with the direction of growth.

3.3. Metallographic characterization

All the metallographic characterization was performed in the laboratories of the Department of applied science and technologies (DISAT) of Politecnico di Torino.

3.3.1. Cutting

The cutting process is the first step for metallographic characterization. The samples were cut by a precision cut-off machine, the *Buehler Isomet 4000* (Figure 31)

Figure 31: Buehler Isomet 4000 [66].

The procedure started choosing the correct sample holder and after it was fixed by screws to the moving platform. Subsequently it was necessary to choose the appropriate cutting blade and anchor it to the spindle by plate and bolt. In this work a cermet blade was chosen. When the blade is fixed, the sample is located and locked in the sample holder in such a way that no interference is observed between the blade and any object during cutting. The cutting direction was x-z.

Before setting the cutting parameters, it was necessary to check the lubricant flow. Therefore, a special command was used to activate the flow of liquid which is sprayed onto the blade. Once the direction of the flow has been adjusted, so that one nozzle wets the side of the blade and the other the cutting edge, it was possible to move on to the next step.

Thanks to the control panel, rotation speed, feed rate and cut length were possible to be set. These parameters were chosen according to the material (Table 6).

Table 6: Precision cut-off machine parameters.

Parameter	**Value**
Rotation speed	1600 rpm
Feed rate	0,5 mm/s
Cut length	25 mm

When the cutting parameters have been set, the sample was positioned a few millimeters from the blade by the movement of the table. The hood was closed and the cutting process started.

When the cut was finished the blade stopped and it was possible to open the hood and to remove the two pieces of the sample. At this point, the pieces of the sample were marked. The procedure was repeated for each cubic sample.

3.3.2. Grinding and polishing

Once the cutting process has been completed a surface finishing process was necessary. This step is important for the further surface observations of the samples. Grinding and polishing processes were conducted according to ASTM D5671-20 [67] standard method. The *Mecotech 234* (Figure 32), was used to carry out this task.

Figure 32: Mecotech 234.

The entire process is carried out by abrading the surface; various abrasive papers (grinding) and cloths (polishing) were used to obtain an adequate polish. The grinding activity began using a P400 abrasive paper, which was blocked by a ring to a rotating table. The machine was then switched on and a rotating table speed of 250 rpm was set. The process requires the presence of water to transport away the abraded particles and keep the temperature low during the process. Therefore, the water flow was centrally positioned and regulated by a knob. At this point, it was possible to start the operation. The sample can then be placed on the abrasive paper and grinded in such a way that the desired surface is abraded (Figure 33).

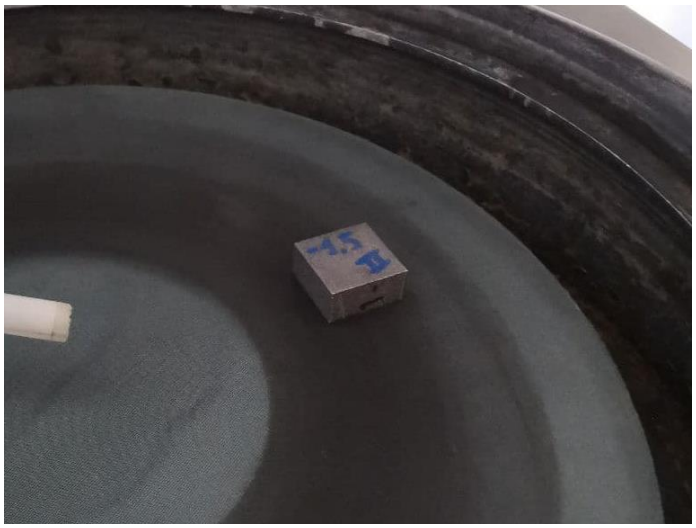

Figure 33: Sample in polishing position

Initially, the sample should be oriented in such a way as to create scratches at right angles to the existing scratches (Figure 34). This operation allows having a visual check on the scratch disappearance. When the previous lines have disappeared, it was necessary to change the abrasive paper. It was used an abrasive paper with a finer grit size, i.e. with a higher P value.

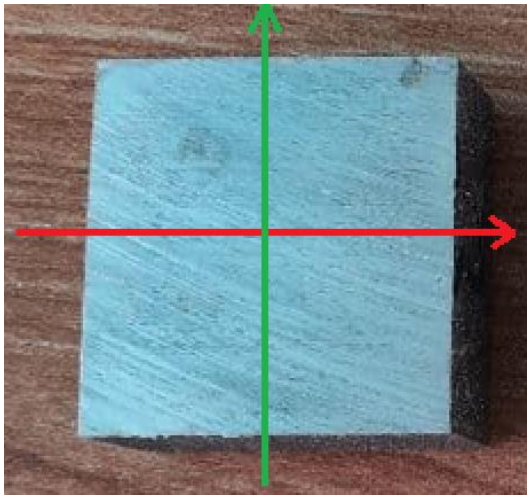

Figure 34: Correct and wrong direction to place the sample during polishing

In this work, a P600 abrasive paper was used. The process can be repeated always orienting the sample in such a way as to create scratches orthogonal to the previous ones. The procedure just described has been carried out for further 4 times using respectively abrasive papers P800, P1200, P2400 and P4000 (Figure 35). When P4000 grinding were finished, the samples were further polished using pans with 3 and 1 µm sticks respectively.

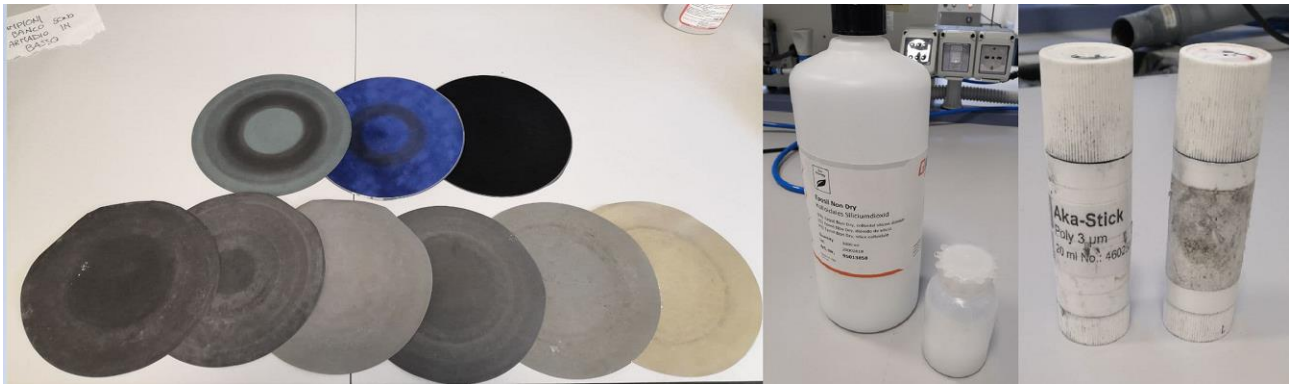

Figure 35: Pans and abrasive paper (left); Colloidal silicon dioxide (center); 3 µm and 6 µm pans sticks (right).

The last step was to polish the surface with a solution of distilled water and silica particles (1:1 ratio of silica). At the end of the process, the samples have a mirror-like surface (Figure 36).

Figure 36: Samples after cutting on the left and after polishing on the right

3.3.3. Chemical Etching

The etching was carried out to highlight and allow the analysis of the microstructure. To carry out this operation, Keller acid is distributed on the previously polished surface of the sample. Keller acid composition is shown in Table 7. The acid reacts preferentially along the borders and center of melt pools, generating a clearer image of them.

The etching operation was conducted under a ventilated hood and the reaction time was 10 s (Figure 44). The reaction was stopped by water.

Table 7: Keller acid composition

Keller acid composition	
Hydrofluoric acid (HF)	1 cm^3
Hydrochloric acid (HCl)	1.5 cm^3
Nitric acid (HNO_3)	2.5 cm^3
Water (H_2O)	9 cm^3

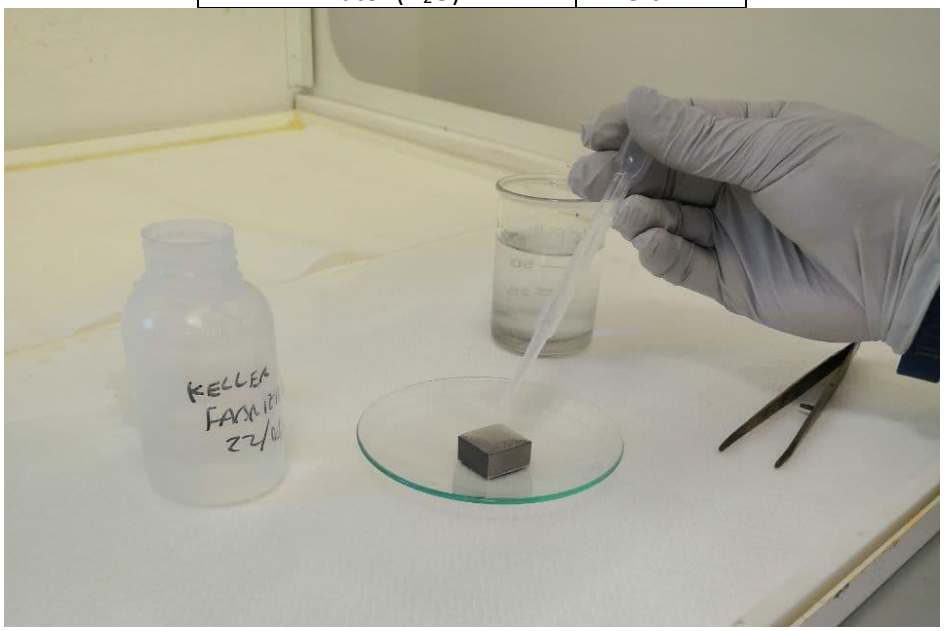

Figure 37: Keller-etching.

3.3.4. Image acquisition

After polishing, it was possible to analyze the surface of the samples, i.e. the x-z plane. To carry out this operation, *Leica MDI 500M* (Figure 37) optical microscope was used. The microscope can analyze the surface of the sample, at different levels of magnification, thanks to the planar movement of the sample holder.

Figure 38: Leica DMI 500M

In this step mainly three tasks were carried out:

- **<u>Porosity image acquisition</u>**

  The acquisition procedure starts by turning on the microscope and the acquisition software. Then it was necessary to select the desired level of magnification. In the porosity image analysis were obtained images respectively with 50x and 100x level of magnification. Subsequently the sample to analyze was placed on the sample holder and oriented following the building direction. Brightness and contrast were adjusted. Subsequently, using two knobs able to move the sample on the x and y axis respectively, 12 images per sample were acquired according to the schema shown in Figure 38.

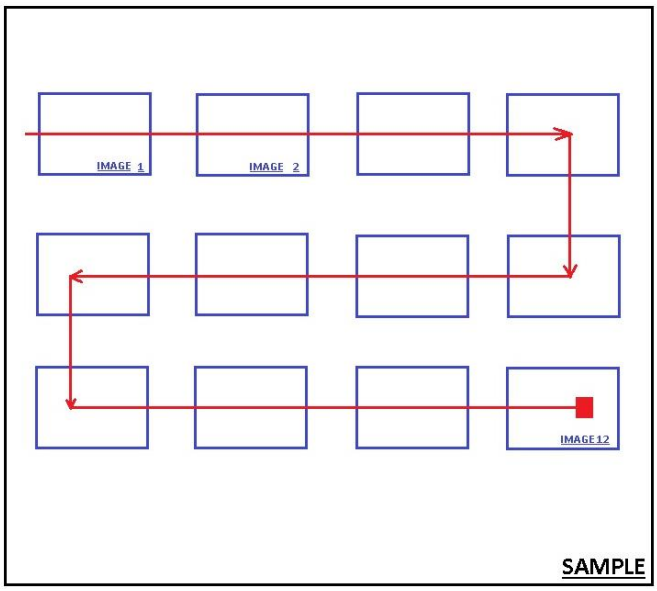

Figure 39: Image acquisition schema.

Once the first 12 images were acquired, the magnification level was changed to 100x and other 12 images were acquired according to the same acquisition schema.

The images are acquired in greyscale as the subsequent analysis requires this methodology to obtain the porosity information. An example of an image can be seen in Figure 39, in which the pores are highlighted in black while the bulk is grey.

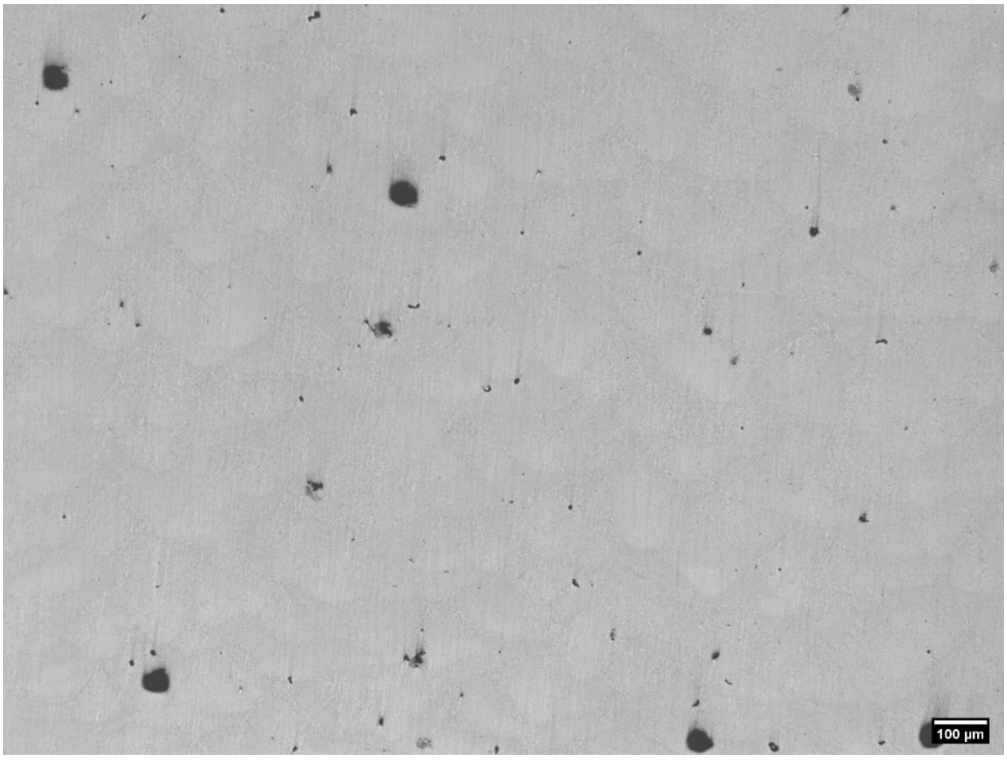

Figure 40: Porosity image obtained from optical microscope.

- **Melt pool image acquisition**

The melt pool image acquisition was carried out on the metallographic etched samples. It was used the same procedure of porosity image acquisition but were obtained 10 images per sample with 100x level of magnification. An example of an image can be seen in Figure 40, in which the pores are in black, as before, while the melt pool boundaries in white.

Figure 41: 100x image of the melt pools obtained by optical microscope.

- **Microstructure image acquisition**

The microstructure images were obtained after etching. Images of two different zones for each sample were obtained at different levels of magnification. Magnification levels of 500x and 1000x were adopted. An example of the image obtained is shown in Figure 41.

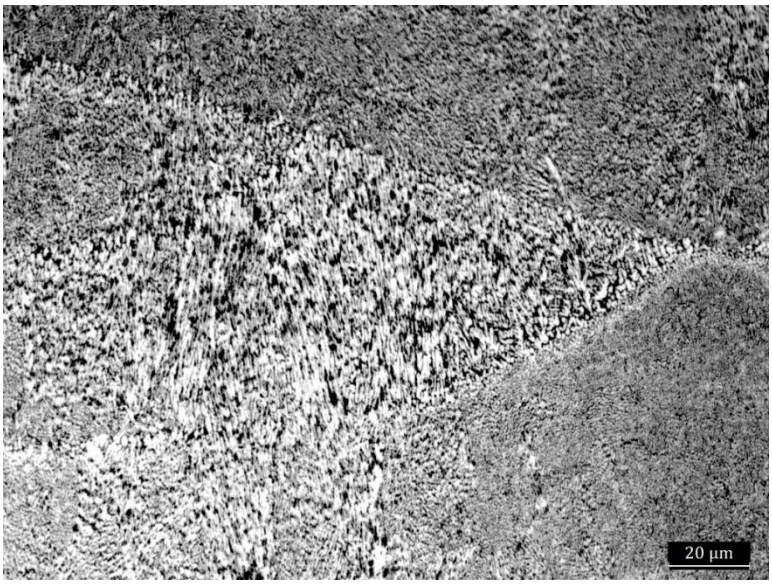

Figure 42: 500x image of the microstructure obtained by optical microscope.

3.3.5. Image analysis

Once the images were acquired, it was possible to post-process them using Image J software. *Image J* is an image processing and analysis software in Java developed by National Institutes of Health, United States. Two kind of image analysis were performed.

Porosity image analysis

Image J requires an 8-bit image to perform porosity analysis. For this reason, the first operation carried out was the conversion of the image. This operation transformed the image into a grey scale, so each pixel is characterized by a grey intensity. Due to the different reflection of light, porosity and defects are shown in dark color (Figure 42).

In order to distinguish massive material and defects, the *Threshold function* is used (Figure 42), which generates a binar image (Figure 42) depending on the greyscale threshold value. The threshold value was chosen manually and customized for each image. At this point, the *image analysis command* was launched. The quantifies the black area against the white one, returning a percentage. The *% Area* parameter was extrapolated and analyzed to obtain statistical information.

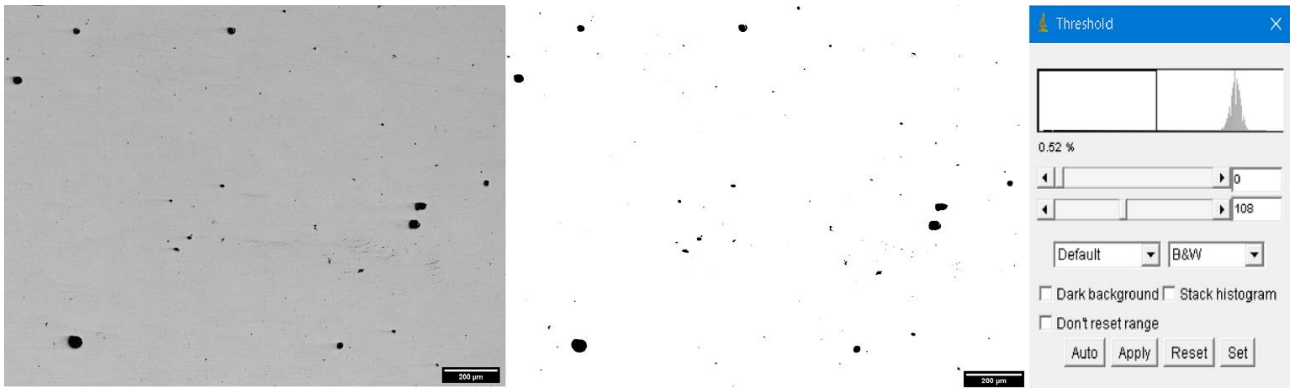

Figure 43: Pre and post porosity image analysis (left) and Threshold function (right)

Melt pool geometry

The size of the melt pools was calculated by drawing segments corresponding to the width and depth of the melt pools. To carry out this operation, it was necessary to define the image scale by *Set Scale Bar* command. It allows to perform the measurement with unit of measurement chosen. Once the definition of the image scale was completed, the segments relative to the dimensions of the melt pools were traced, highlighted and analyzed (Figure 43). The melt pools to be analyzed were chosen by selecting melt pools with defined and

partially recast edges. At the end of this operation the relative lengths were saved and analyzed to obtain statistical indications.

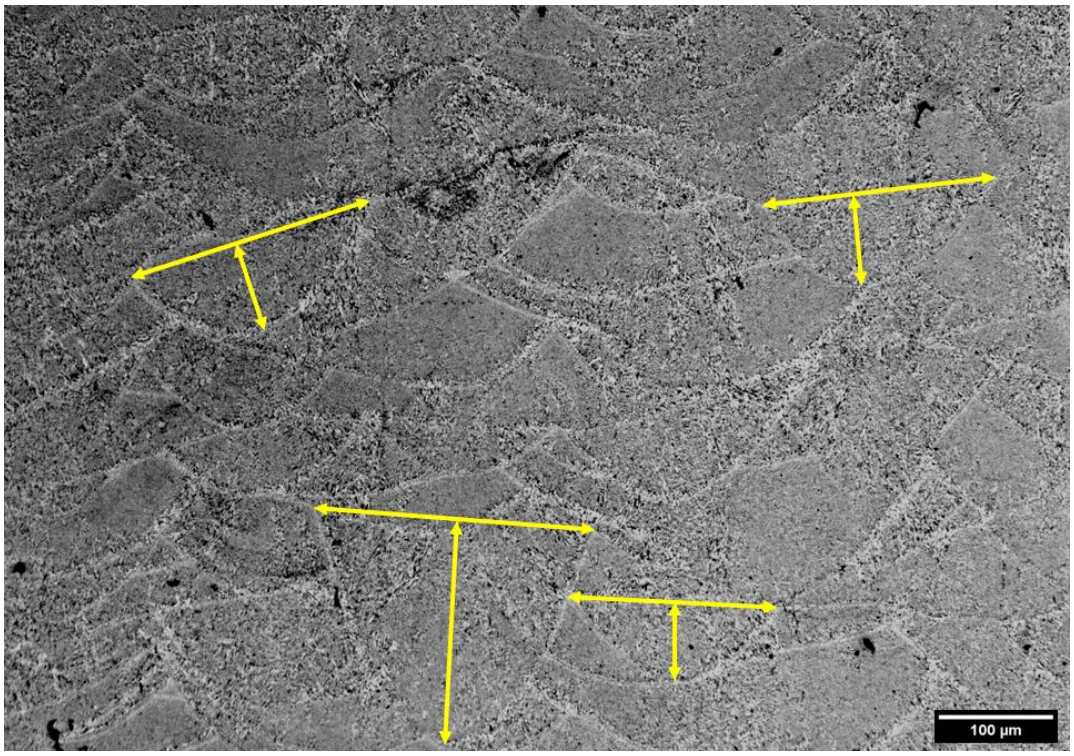

Figure 44: Segment about melt pools geometrical characteristics analysis.

3.3.6. Fracture Surface Analysis

The fracture surface analysis was carried out to obtain information regarding to the mechanism of fracture of the samples made with different defocus distances. *Phenom ProX*, a Scanning Electron Microscopy (SEM) machine (Figure 45), was used to obtain the fracture information. The specimens with the best mechanical characteristics, for each laser spot condition, were cut to analyze the fracture surfaces. The specimens were cut by *Buehler Isomet 4000*, orthogonally to the longitudinal direction of the tensile specimens at about 3 mm from the surface to be analyzed.

Figure 45: Phenom ProX SEM machine[68].

The samples were then cleaned of impurities using a sonicator machine. The samples were immersed in an ethanol bath which was sonicated for ten minutes. After sonication the samples were dried and placed on the pin stub.

Using the SEM machine, the fracture surfaces of the samples was evaluated at different levels of magnification.

3.4. Mechanical tests

3.4.1. Tensile test

The tensile test was conducted on the specimens made with vertical and horizontal growth direction according to ASTM E8 [69] standard method. The machine Zwick-Roell Z050 tensile tester (Figure 46) was used to carry out this test.

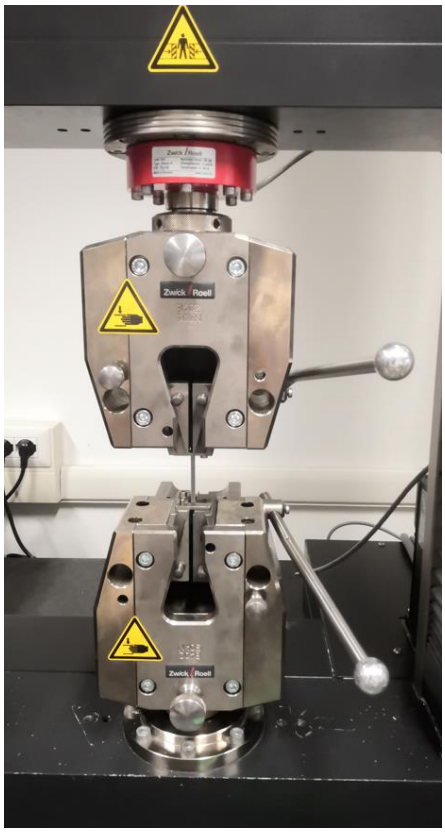

Figure 46: Zwick-Roell Z050 tensile tester.

Before starting the tensile test, the samples were marked with their process parameters, numbered in ascending order and marked with the 30 mm useful length, as shown in Figure 47.

Figure 47: Zero focus marked samples.

The useful length was taken as the inner distance between the red lines.

The first operation carried out was to fix the correct sample clamps to the fixed and mobile rod, then the machine was switched on and configured. After this operation, the sample was clamped in the sample holders (Figure 48) in such a way as to prevent slippage and the strain gauge was connected in the central area of the useful section. After that, the test started and the strain gauge was held in position until few moments before breaking.

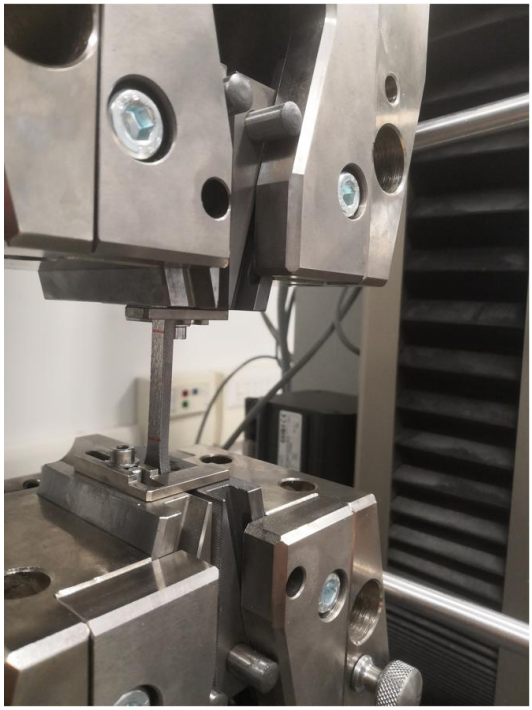

Figure 48: Clamped sample.

The specimen was then removed from the machine and the operations described above were carried out for the remaining specimens. At the end of the test, the two edges of the specimens with best mechanical

characteristics were brought back into contact and a gauge was used to obtain a measurement of the final length of the useful section.

Were obtained information about Ultimate Tensile Strength (UTS), Yield Stress (YS), % Elongation (ε) and Young's modulus.

3.4.2. Microhardness

The Vickers microhardness test was carried out by the *Microhardness tester VMHT* (Figure 49). The microhardness test is based on the analysis of the impression (Figure 50) left by an indenter loaded with a known weight for a certain time. The machine parameters used are shown in Table 8.

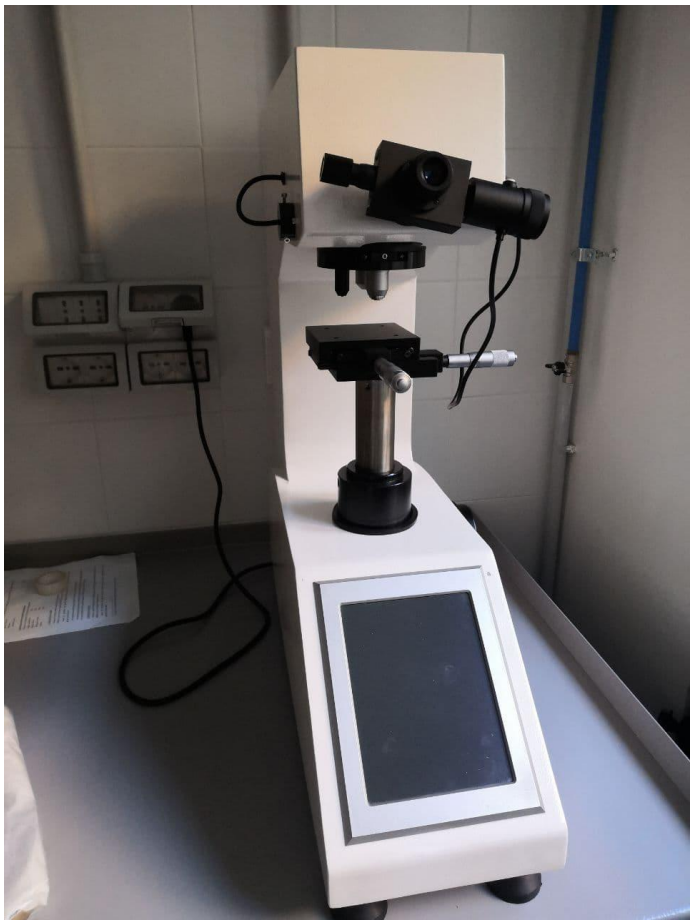

Figure 49: Microhardness tester VMHT

In order to carry out this test, it is necessary to have perfectly flat-parallel specimens.

The microhardness test was conducted according to ASTM E384 – 17 [70]. It started by focusing the sample through a 100x lens, then the measuring system of the machine was calibrated by aligning the measuring lines. After alignment, the sample surface was focused with a 400x lens and the machine parameters were set. The microhardness test was then conducted. Subsequently, the diagonals of the impression, D1 and D2, were obtained manually through the measurement lines (Figure 50). The machine software is able to subsequently indicate the hardness value from the diagonal measured. This value was transcribed for subsequent statistical analysis.

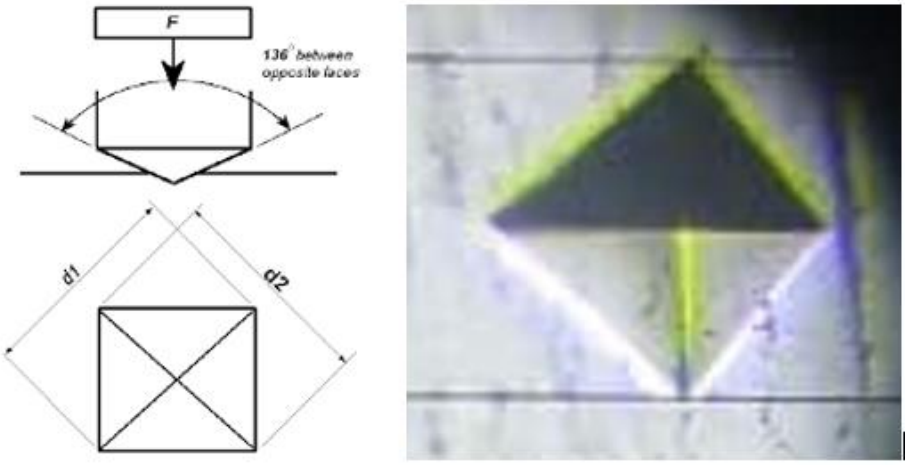

Figure 50: Impression of Vickers microhardness test [71] and D2 measurement

Table 8: Microhardness test parameters

Parameters	Value
Load	0.1 Kg
Dwell Time	15 s

This procedure was carried out 10 times per sample with a distance between the impressions greater than 5 times the value of the largest diagonal.

4. Results & Discussion

4.1. Microstructure characterization

4.1.1. Porosity

The porosity data extracted from Image J were analyzed and processed to obtain the porosity mean values and their standard deviations of the samples. In Table 9, 10, 11 and in Figure 51, 52, 53 the mean value and standard deviation of the porosity of the samples with constant focus are shown.

Table 9: Mean porosity and its standard deviation of samples obtained with defocus distance of -1,5 mm.

Sample	1	2	3
Mean Porosity [%]	0.298	0.688	0.729
Standard Deviation	0.114	0.310	0.325

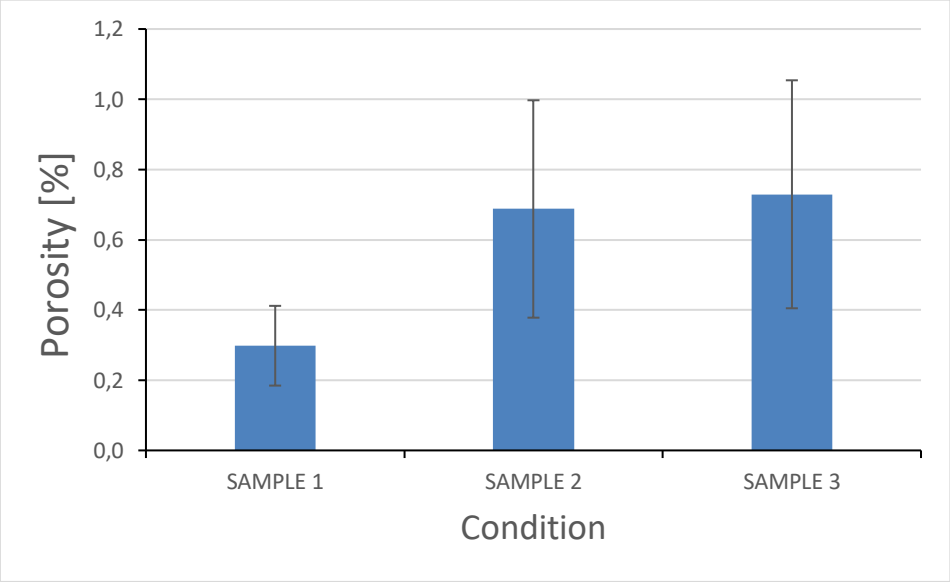

Figure 51: Bar chart of porosity results of samples obtained with defocus distance of -1,5 mm.

Table 10: Mean porosity and its standard deviation of samples obtained with zero defocus distance.

Statistical parameter	Sample 4	Sample 5	Sample 6
Mean Porosity [%]	0.581	0.673	0.218
Standard Deviation	0.253	0.340	0.117

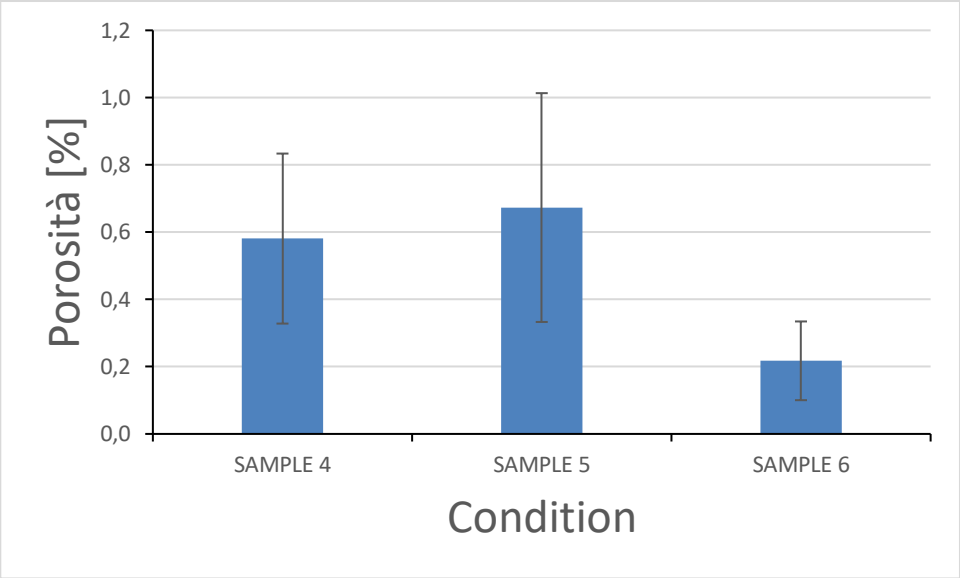

Figure 52: Bar chart of porosity results of samples obtained with zero defocus distance.

Table 11: Mean porosity and its standard deviation of samples obtained with defocus distance of +1,5 mm

Statistical parameter	Sample 7	Sample 8	Sample 9
Mean Porosity [%]	0.220	0.162	0.560
Standard Deviation	0.137	0.095	0.266

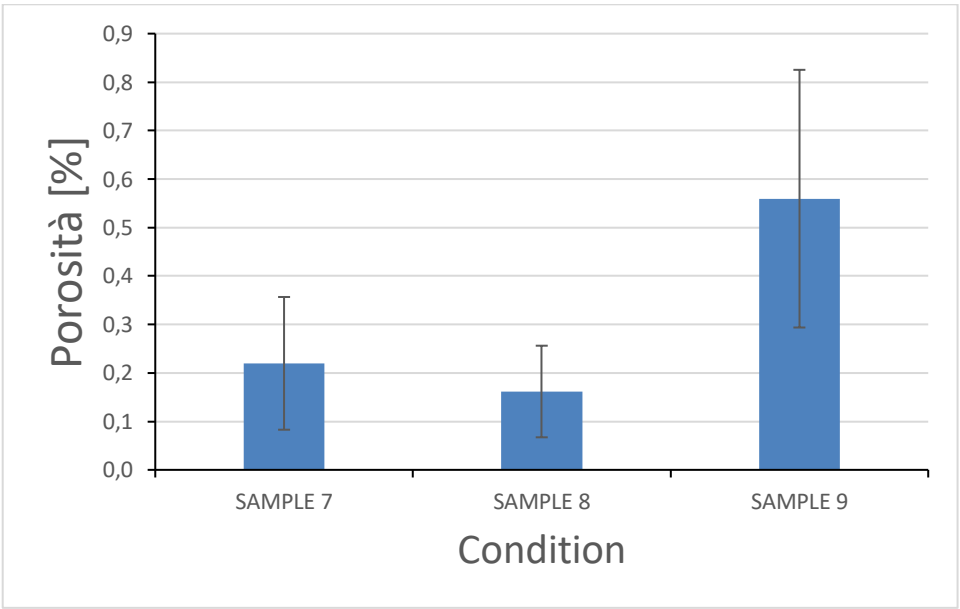

Figure 53: Bar chart of porosity results of samples obtained with defocus distance of +1,5 mm.

In Table 12 and in its correlated Figure 54 the porosity mean values, the mean density and their standard deviations of the samples obtained with different defocus distance (Δf) are shown.

Table 12: Mean porosity, mean density and their standard deviation of the samples obtained with different defocus distance.

Statistical parameter	Δf= -1,5 mm	Δf= 0 mm	Δf= +1,5 mm
Mean Porosity [%]	0.572	0.490	0.314
Mean Density [%]	99.428	99.510	99.686
Standard Deviation	0.249	0.237	0.166

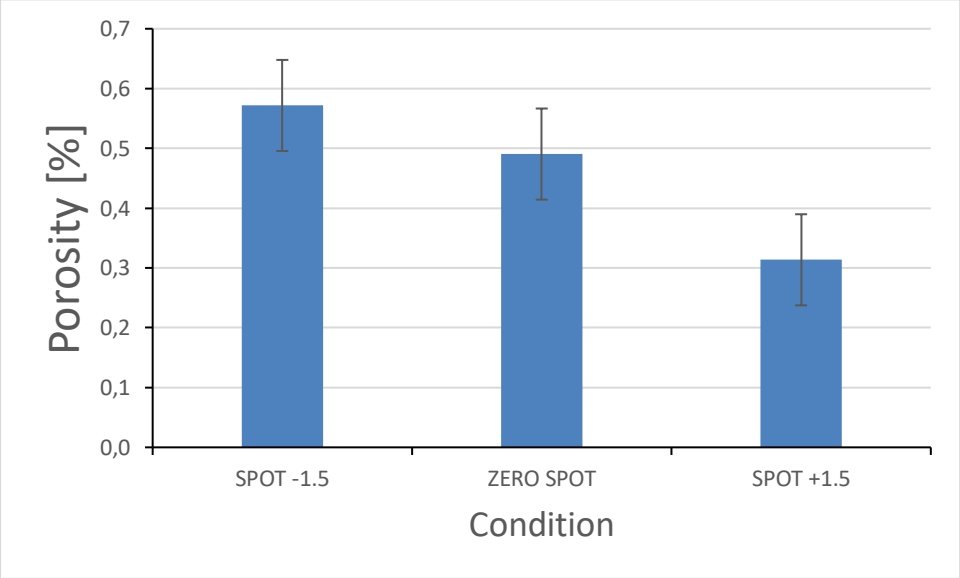

Figure 54: Bar chart of the porosity results of the samples obtained with different defocus distance.

The samples obtained with a defocus distance of +1.5 mm have the lowest porosity value, in average value. The samples obtained with zero and negative defocus distance are more porous in average value, the most porous sample is the one obtained with defocus distance -1.5. In absolute terms the average values of the samples obtained with zero and -1,5 mm of defocus distance are within the standard deviation of the other samples. Overall, the porosity results of the samples obtained at different defocus distances show a slight trend of reduction of the porosity as the defocus distance increases. Similar behavior of the porosity as a function of variation of the laser beam focus is observed by Zhou et al [55].

In Figure 55, 56, 57 a 50x images of each sample obtained by optical microscope are shown.

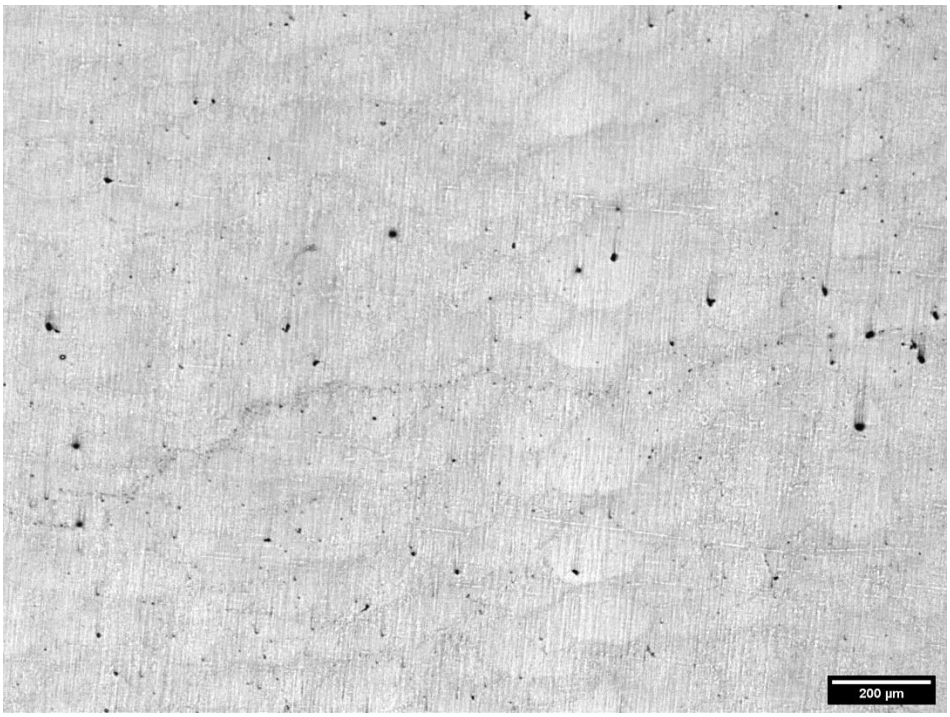

Figure 55: 50x optical microscope image of sample n.1 obtained with defocus distance of -1,5 mm.

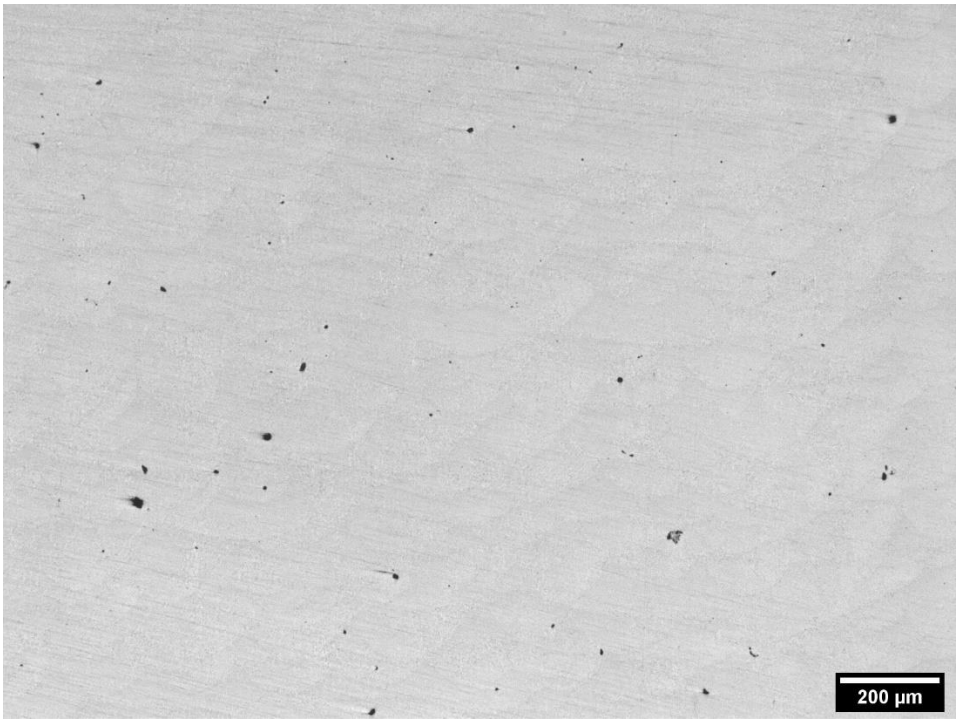

Figure 56: 50x optical microscope image of sample n.6 obtained with zero defocus distance.

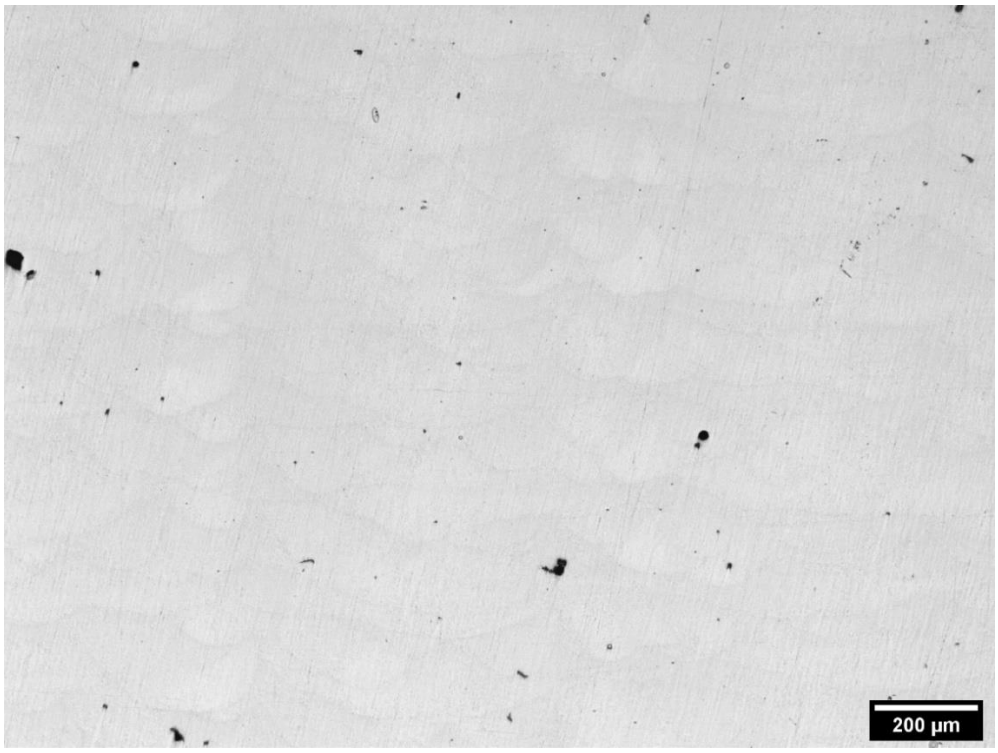

Figure 57: 50x optical microscope image of sample n.7 obtained with defocus distance of +1,5 mm.

For the sake of completeness, Figure 58 shows the average density and standard deviation obtained from the samples with different focus.

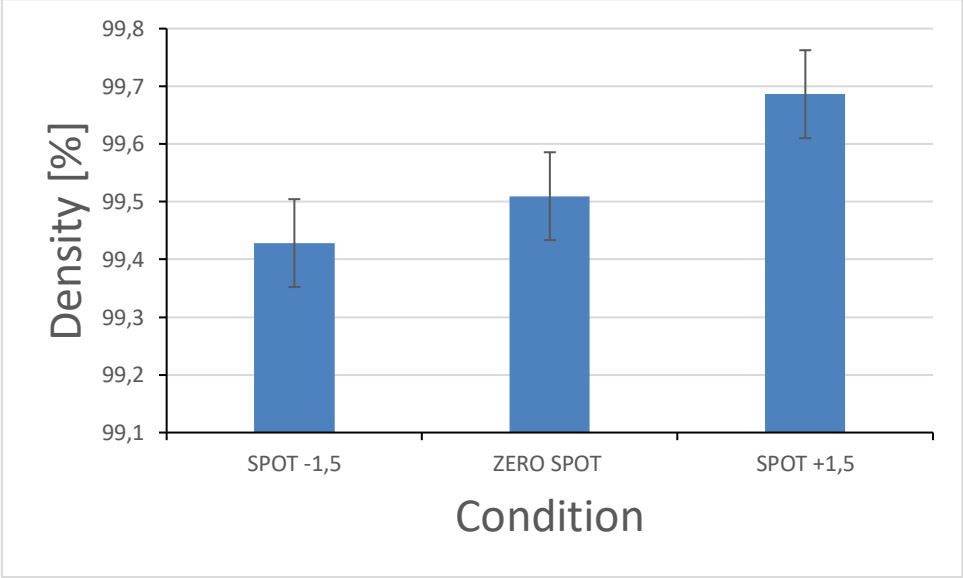

Figure 58: Bar chart of the density results of the samples obtained with different defocus distance.

All the samples have a mean density greater than 99%.

4.1.2. Melt pool analysis

The data from Image J were processed to obtain the mean values and standard deviations (σ) of the width and the depth of the melt pools. In Table 13 the results of the analysis are shown.

Table 13: Results of melt pool analysis

Sample	Width (W)		Depth (d)	
	Media [µm]	σ	Media [µm]	σ
Δf= -1,5 mm	180.14	26.23	83.13	35.77
Δf= 0 mm	204.74	37.44	62.83	18.02
Δf= +1,5 mm	183.46	34.90	64.06	18.76

The results of the melt pool analysis are plot in Figure 59 and 60.

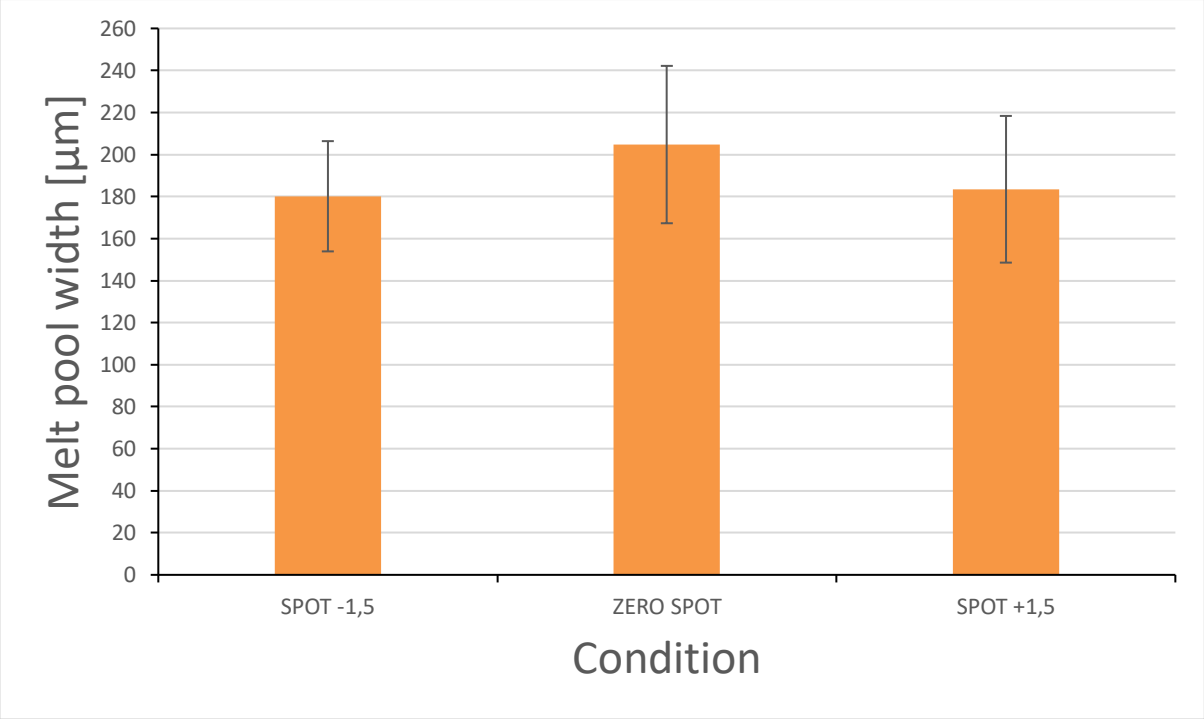

Figure 59: Bar chart of melt pool width analysis of the samples obtained with different defocus distance.

Samples obtained with zero defocus distance present the greatest mean value of melt pool width. Samples produced with defocus distance of 1.5, in absolute terms, have approximately the same mean value of melt pool width, on average.

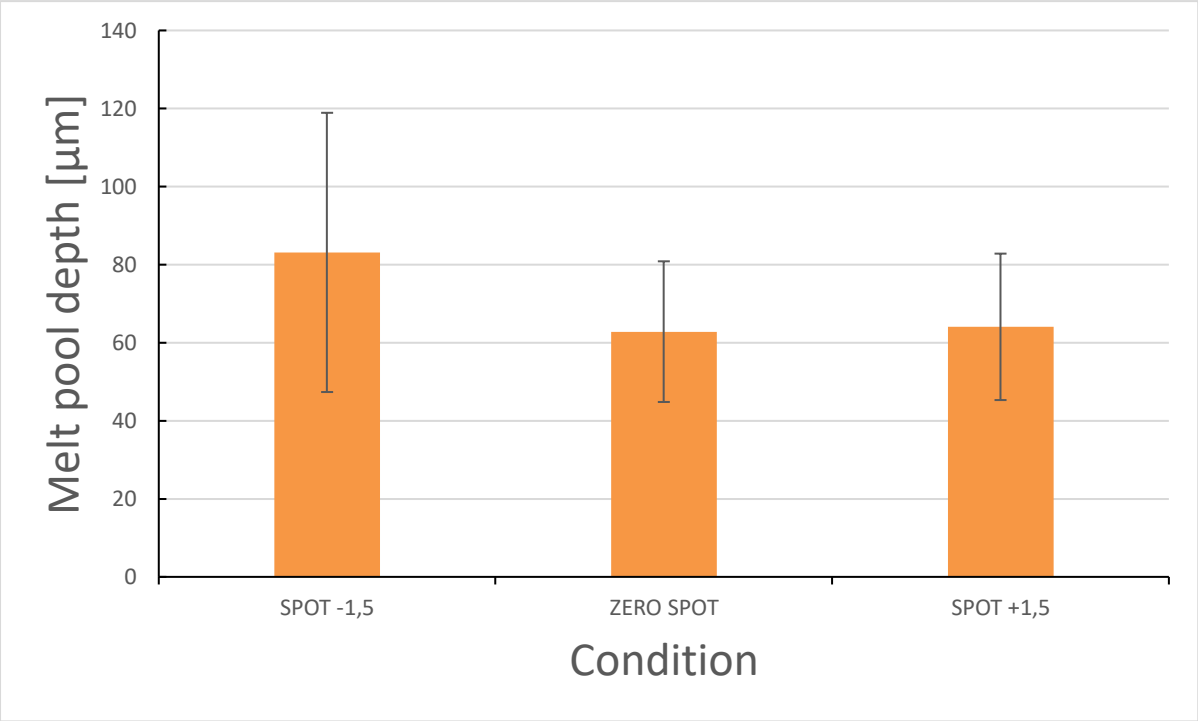

Figure 60: Bar chart of melt pool depth analysis of the samples obtained with different defocus distance

Samples produced with a negative defocus distance, on average, have deeper melt pools. Samples produced with zero defocus distance and +1.5 have approximately the same mean value of melt pool depth.

In both geometric characteristics of the melt pools, no trend is observed.

Even in this case it can be asserted that the changing of focus conditions, does not affect significantly the shape of the melt pools.

4.1.3. Microstructure Analysis

The microstructure of the samples obtained in collaboration with Prima Industrie SpA was analyzed by optical microscope. In Figure 61, 62, 63 an image of the microstructure at 500x and 1000x for each laser spot condition is shown.

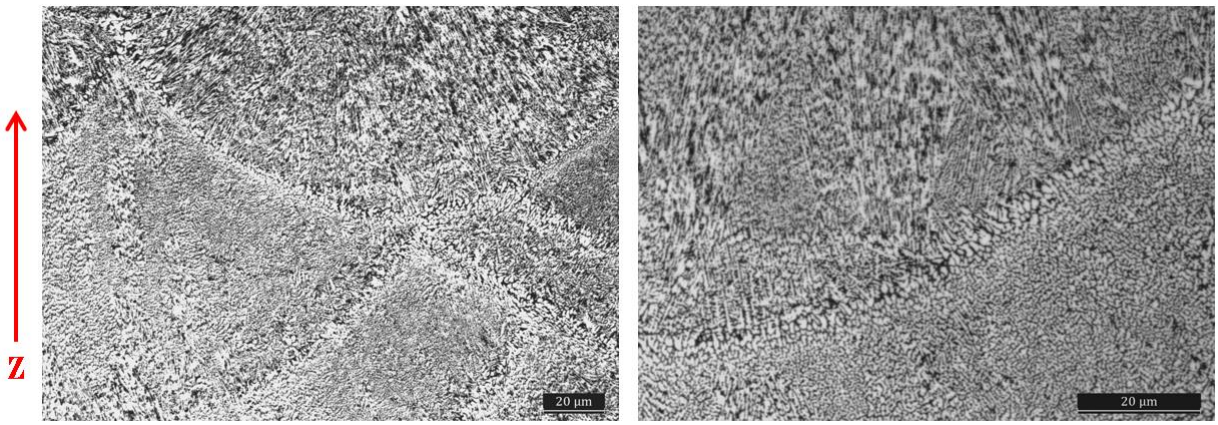

Figure 61: 500x (left) and 1000x (right) image of sample n.1(focus -1.5).

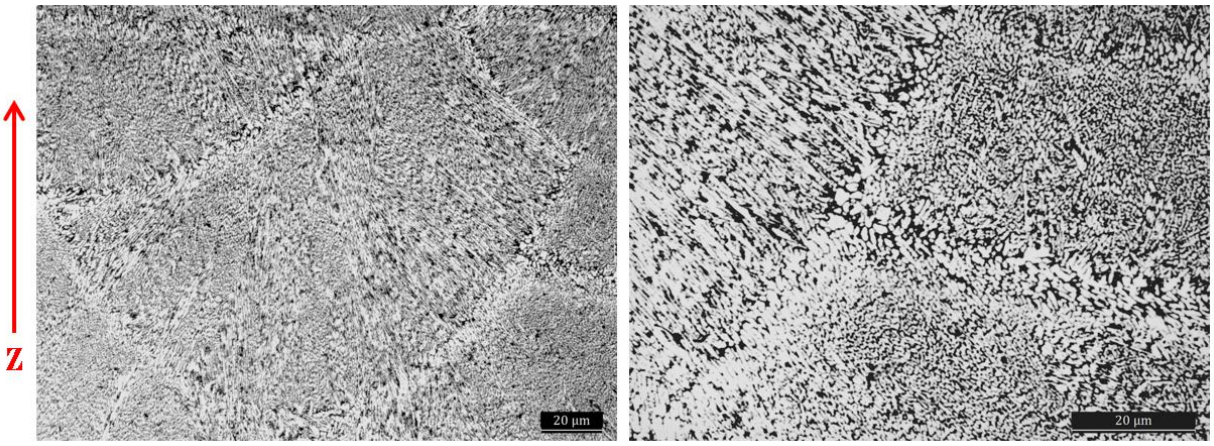

Figure 62: 500x (left) and 1000x (right) image of sample n.6 (focus 0).

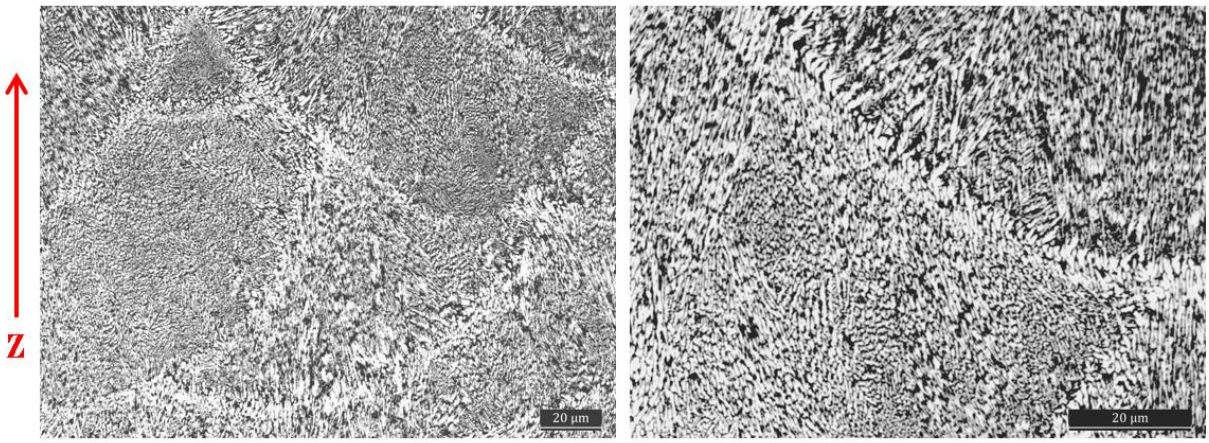

Figure 63: 500x (left) and 1000x (right) image of sample n.8 (focus +1.5).

All samples show a similar microstructure. The presence of an α-aluminum matrix surrounded by a eutectic silicon lattice is observed. No microstructural changes are observed due to variation in defocus distance.

The presence of columnar structures preferentially oriented along the growth direction of the specimens (z) is observed. The columnar structures are oriented along the z-direction due to local thermal gradients. The local thermal gradient is always oriented orthogonally to the melt pool boundaries (MPB) (Figure64).

Microstructural variation is observed within the melt pools. Three different zones can be distinguished (Figure 64), they are characterized by:

- Fine cellular structure, in the center of the melt pool (1 in Figure 64);
- Coarser cell structure, from the center to the edges of the melt pool (2 in Figure 64);
- Heat affected zone, near the edges of the melt pool (HAZ in Figure 64).

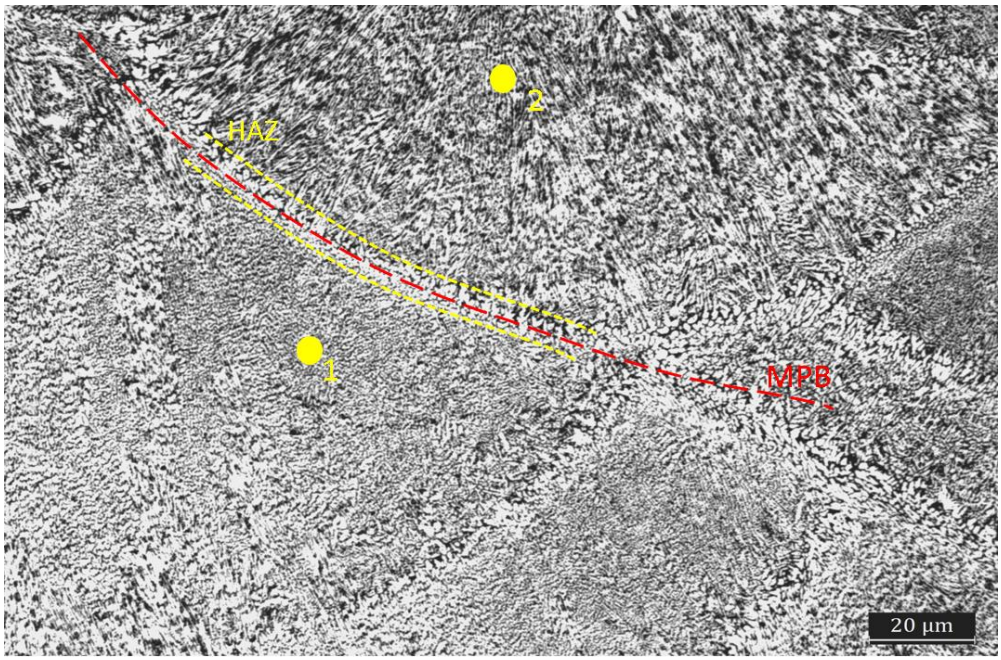

Figure 64: Microstructural variation inside the melt pool.

The presence of a fine cell structure is due to the presence of a homogeneous thermal gradient in the central zone of the melt pool. The central zone of the melt pool is also subject to rapid cooling, which preferentially induces the phenomenon of nucleation, so fine structure occurs.

The presence of a coarser cell structure is due to the presence of a strong thermal gradient. The thermal gradient has made the phenomenon of growth preferable to nucleation, so we observe larger and more directional grains.

This microstructural variation is observed also from other researchers[59][55][42][72].

4.2. Mechanical tests

4.2.1. Tensile Test

The tensile test was carried out to evaluate the variation in mechanical characteristics of the samples made with different laser spots. The results obtained were processed in such a way as to obtain indications of mean values and standard deviations of the Ultimate Tensile Strength (UTS), Yield Stress (YS), % Elongation (ε) and Young's modulus. In Table 14, the results of the analysis and values from literature (LV) [55] are shown.

Table 14: Tensile test results of the analysis and value from literature[55].

Sample	Young's Modulus [GPa]		Ultimate Tensile Strength [MPa]		Yield Stress [MPa]		% Elongation	
	Analysys	LV	Analysis	LV	Analysis	LV	Analysis	LV
Δf= -1,5 mm	56.12 ± 5.57	63.7	400.28 ± 8.98	395 ± 12	239.09 ± 12.92	177 ± 6	4.6	7.3 ± 1.2
Δf= 0 mm	58.22 ±7.74	66.9	404.73 ± 4.36	429 ±20	236.09 ± 8.54	175 ± 6	6.13	7.5 ± 1.5
Δf= +1,5 mm	58.52 ± 8.95	63.5	402.56 ± 7.01	440 ± 15	237.62 ± 10.05	177 ± 6	4.33	8.2 ± 1.6

In figure 65, 66, 67, 68 the tensile test analysis results of the samples obtained with different defocus distance are plotted.

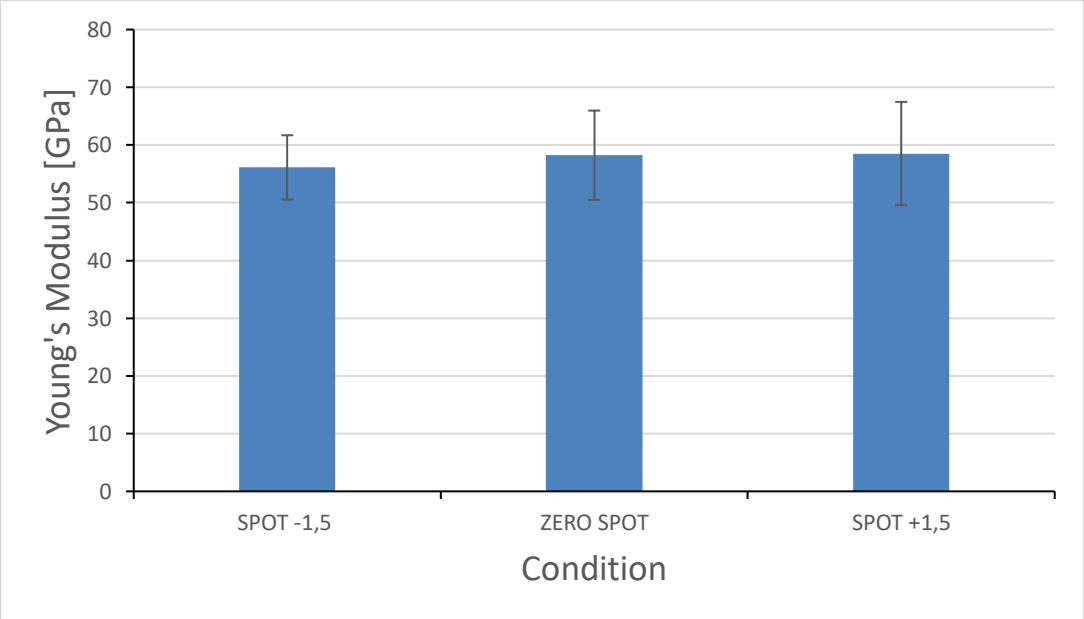

Figure 65: Mean values and standard deviations of Young's modulus of the samples obtained with different defocus distance.

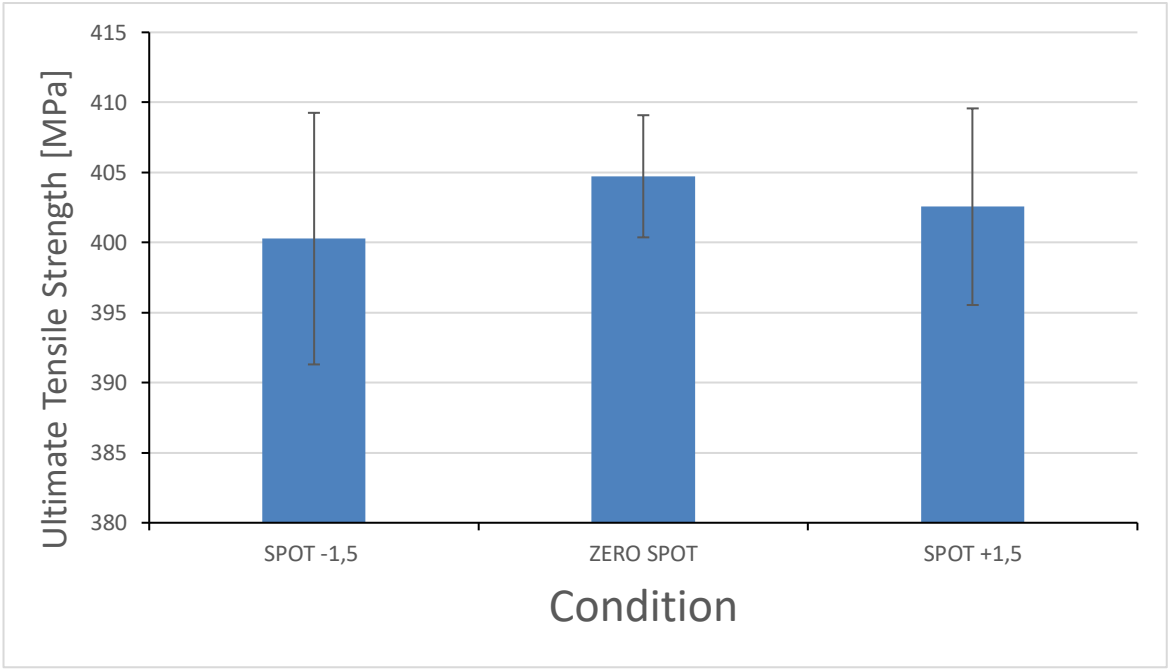

Figure 66: Mean values and standard deviations of Ultimate Tensile Strength of the samples obtained with different defocus distance.

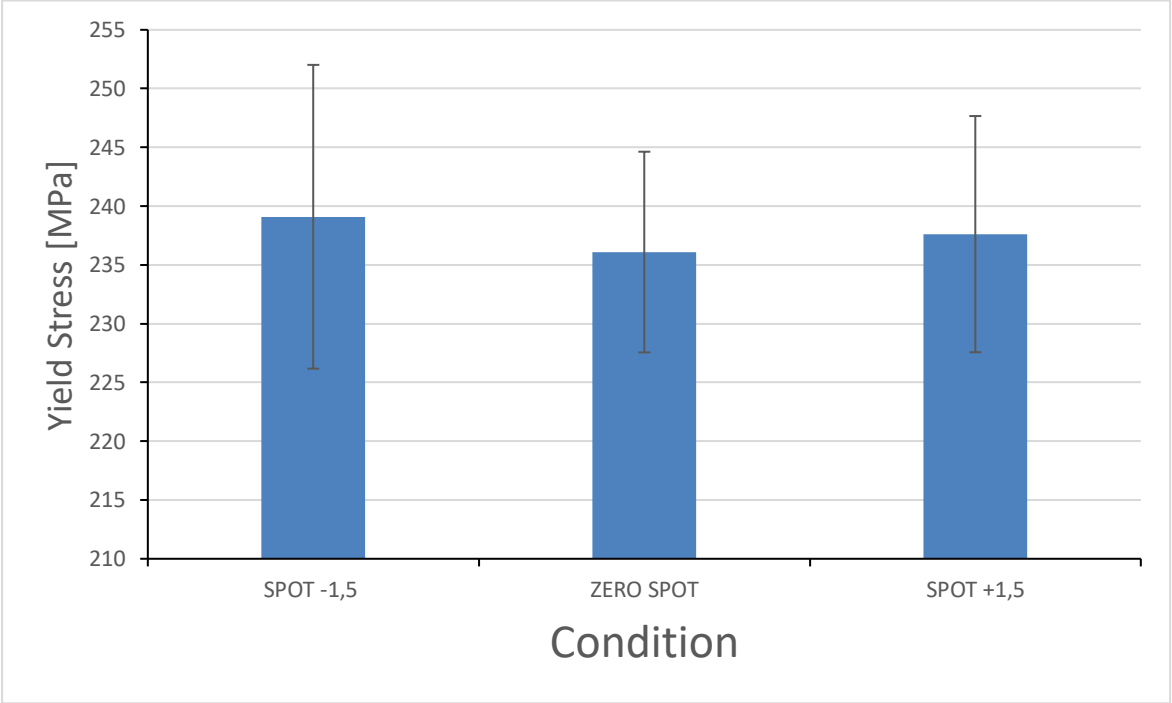

Figure 67: Mean values and standard deviations of Yield Stress of the samples obtained with different defocus distance.

.

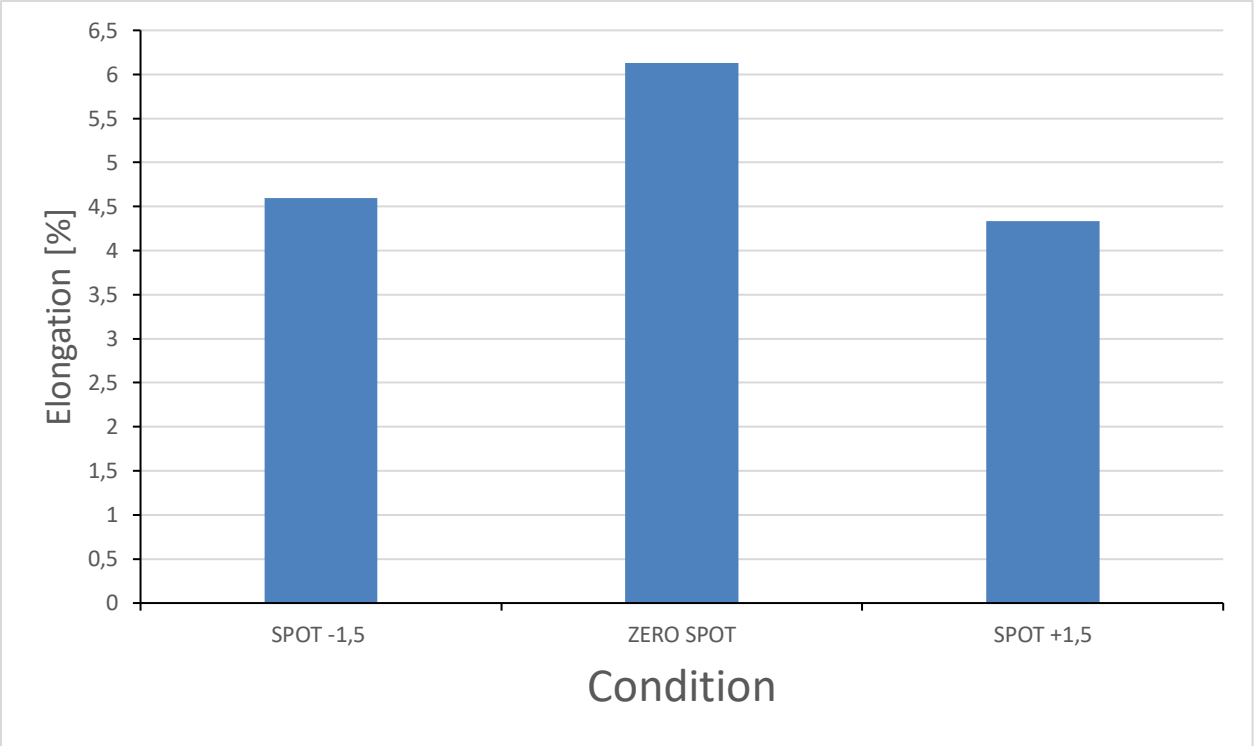

Figure 68: Mean values and standard deviations of Elongation of the samples obtained with different defocus distance.

The samples obtained with zero defocus distance and 1.5 mm defocus distance present the highest mean value of Young's modulus, their value is 58 GPa. The sample obtained with defocus distance -1.5 presents a lower mean value of Young's modulus. There is no significant variation of Young's modulus in the different samples.

The sample obtained with zero defocus distance has the highest mean value of UTS. The mean values of the samples obtained with +1.5 and -1.5 mm defocus distance are slightly lower, 2 and 4 MPa respectively. Even in the case of UTS there are small variations in the mean values and large standard deviations.

The samples obtained with defocus distance of -1.5 mm have the highest mean value of Yield Stress, it is about 239 MPa. The mean value of Yield Stress of the samples obtained with zero defocus distance and +1,5 mm of defocus distance is approximately 3 MPa and 1 MPa, respectively, lower than the mean value of the samples obtained with -1.5 spot. As in the case of Young's Modulus there is no significant variation of YS in the different samples.

The sample obtained with zero defocus distance have the highest value of Elongation, about 6%. The sample obtained with 1,5 mm, in absolute value, of defocus distance present similar Elongation, about 4,5%.

In conclusion, the changing of the focus does not affects significantly the tensile properties of the samples.

As shown in Table 14, the mechanical characteristics of the samples obtained with different defocus distance are lower compared to the values from literature obtained by similar analysis. Zhou et al. [55] obtained the most significant variation in Ultimate Tensile Strength, while the Young's modulus, the YS and the % Elongation results are not strongly affected by 1,5 mm, in absolute value, defocus distance.

The mechanical characteristics of the samples obtained with different defocus distance are also less compared to the values from literature obtained with the best process parameters condition[73][56]. Li et al. [61] reported UTS value of 434.25 MPa.

4.2.2. Microhardness

The data from the Vickers Microhardness Test were processed to obtain information about mean values and standard deviations. The results of the analysis are shown in Table 15 and plotted in Figure 69.

Table 15: Results of microhardness analysis.

Statistical parameter	Δf= -1,5 mm	Δf= 0 mm	Δf= +1,5 mm
Mean Microhardness [HV]	114.27	116.3	116.76
Standard Deviation	8.26	4.18	4.01

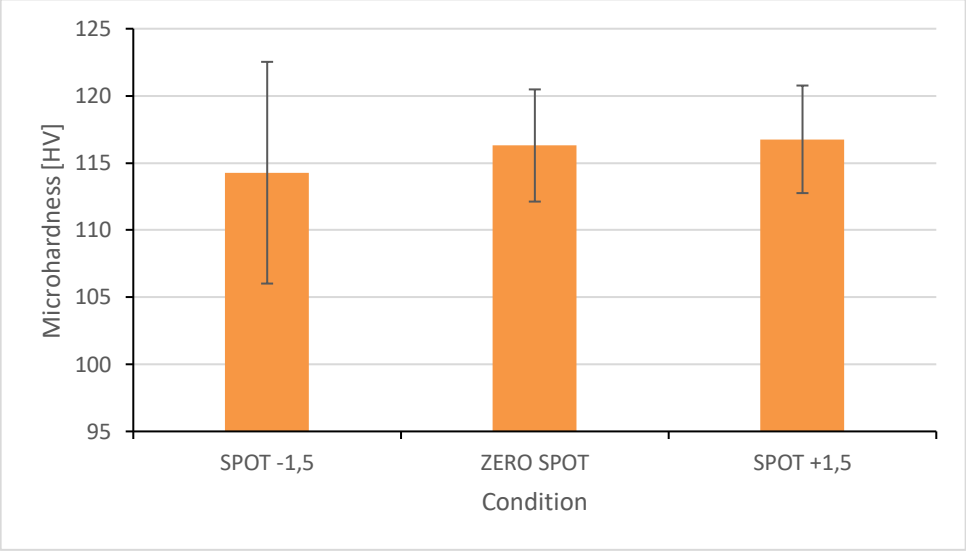

Figure 69: Bar chart of the results of the microhardness analysis.

The samples obtained with zero defocus distance and 1.5 mm defocus distance present the highest mean value of Young's modulus, their value is about 116 HV. The sample obtained with defocus distance -1.5 presents a lower mean value of Young's modulus, about 114 HV. These results are less than the value observed in literature. Thijs et al. [74] reported value of 127 HV in samples realize in AlSi10Mg by L-PBF technology. Even in this case no trend is observed changing the focus distance.

4.2.3. Fracture Surface Analysis

The fracture surface images were analyzed to evaluate the failure mechanism, verified during the tensile test. Figure 70, 71, 72 show the images of fracture surfaces obtained from the SEM microscope, for each laser spot condition.

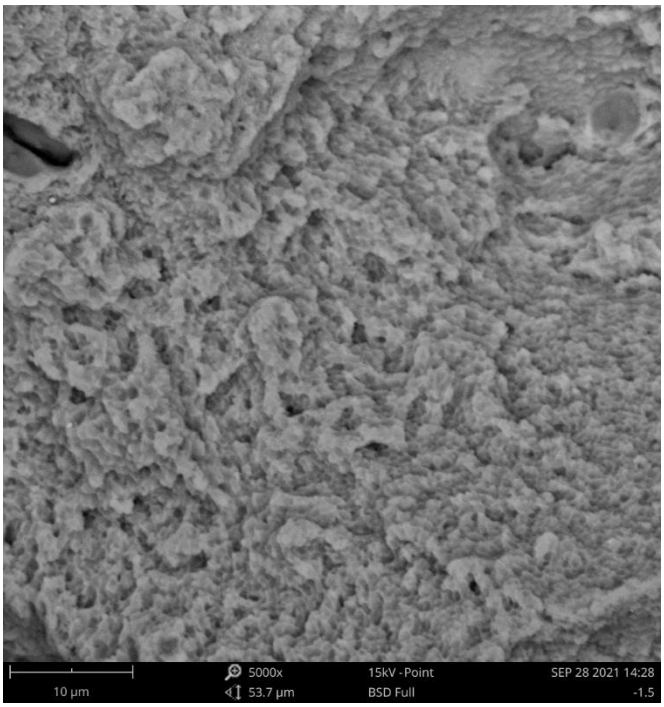

Figure 70: Fracture surface image of the sample n.1(focus -1.5).

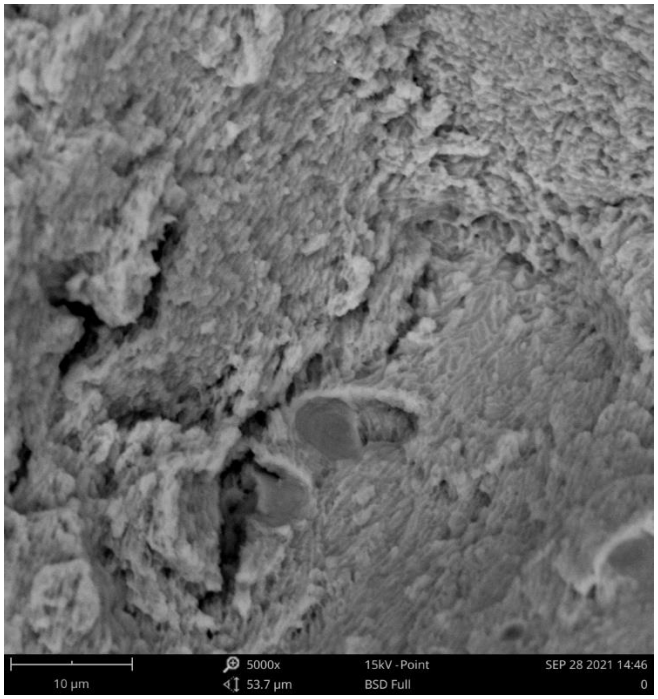

Figure 71: Fracture surface image of the sample n.6(focus 0).

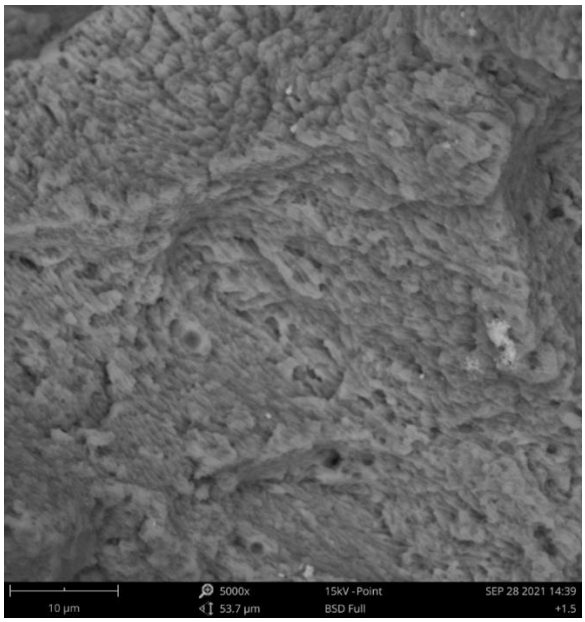

Figure 72: Fracture surface image of sample n.8(focus -1.5).

The fracture surfaces morphology of the specimens obtained with different laser sports are similar.

The fracture surfaces morphology shows the absence of dimples as the failure mechanism is ductile-fragile. This behavior is in agreement with the low elongation shown during the tensile test. Other researchers have obtained similar results in fracture surface analysis [75][74]. W. Li et al [61] obtained the same indications from studying the fracture surfaces of as-build and heat-treated specimens.

The fracture surface analysis also showed the presence of unfused particles within the metal matrix. In Figures 73 and 74 an example of un-melted particles is shown.

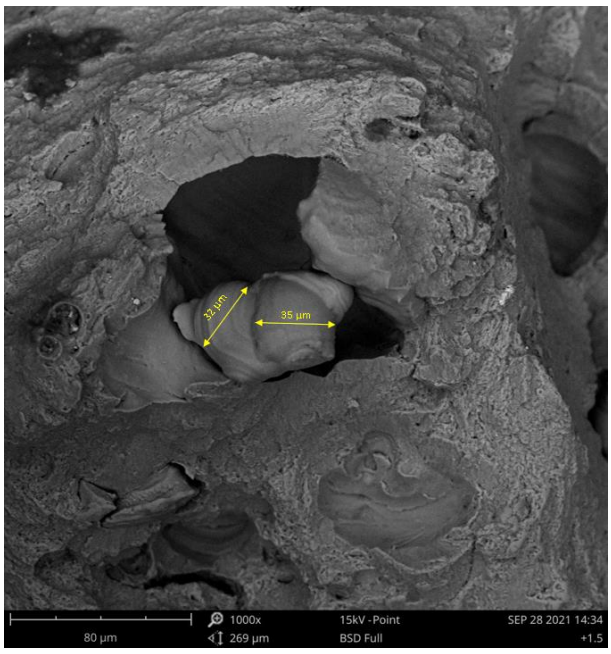

Figure 73: Fracture surface SEM image of two unfused particle.

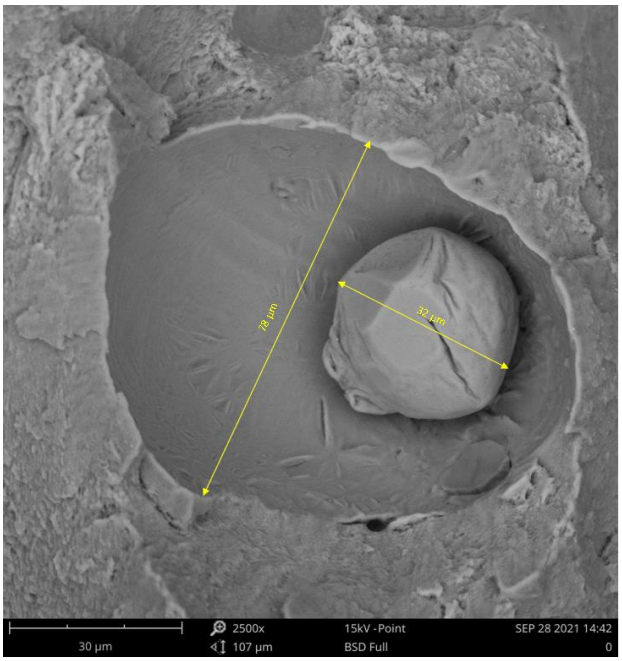

Figure 74: Fracture surface SEM image of a cavity within an unfused particle.

As shown in Figure 73 and 74, the dimension of the particles is in according to the AlSi10Mg powder used (Sample Construction Chapter). Unfused powder particles were found in all laser beam focus conditions. For this reason their presence is not attributable to the variation of the melt pool behavior [76] but to a not fully optimized process [77] and the usage of recycled powder. This issue is also responsible for the observed reduction in mechanical properties. The presence of unfused powder induces the creation of privileged sites for the initiation of fracture phenomena [61].

5. Conclusion

The aim of this work was to analyze the effects of laser beam focus variation on the microstructure and on the mechanical properties of AlSi10Mg samples obtained via L-PBF.

The experimental analyses conducted in this study provided the following results:

- No significant changes were observed in the microstructure and melt pool size caused by the variation of laser beam focus. The same trend was found in the mechanical properties and fracture surfaces.
- The porosity analysis showed a slight increase in density with increasing defocus distance. The samples obtained with 1.5 mm of defocus distance have the highest density value, about 99,67 %. All the samples present a porosity higher than 99.27 %.
- The results of porosity, microstructure and fracture surfaces were found to be in agreement with the results in the literature.
- The presence of un-melted powder particles was observed during the analysis of the fracture surfaces. Their un-melted presence was observed in both samples with defocus distance equal to zero and not. The presence of un-melted powder is due to a not fully optimized process and to the usage of recycled powder.
- The mechanical properties obtained are lower than the values present in literature. This phenomenon is caused by the presence of un-melted particles, which induce the formation of nucleation sites.
- The Prima Additive PrintSharp 250 is able to produce dense parts even with zero or ±1,5 mm defocus distance.

In conclusion, the aims of this study were achieved: the found microstructure consists of a cellular-dendritic structure of α-aluminum phase surrounded by eutectic phase of silicon with different morphologies within the melt pool. The obtained mechanical properties were slightly lower if compared with the values present in literature. Possible future studies could analyze both a wider range and lower values of defocus distance in order to evaluate the effects of laser beam focus at similar VED conditions to the zero defocus distance configuration.

6. Appendix A

"Print Sharp 250 (Figure 75) is the medium volume machine for Powder Bed Fusion applications, developed for industrial production of complex components. Suitable also for Additive Manufacturing service oriented companies and for prototyping purposes, exhibits a high flexibility in terms of part management and operation performance."[78]. In Table 16 the technical specifications of the machine are reported.

Figure 75: Prima Additive Print Sharp 250.

Table 16: Technical specification of PrintSharp 250. In blue the size&power specification, in grey the laser specification, in red the machine&additive process detail and in green the auxiliaries and software specification

Parameter	Value
Dimensions (LxWxH)	3500 (L)- 1100 (W)- 2450 (H) mm
Weight	2000 kg
Power Supply	380 V/50 Hz/8kW
Type of laser	Yb (Ytterbium) Fiber Glass
Laser Power	200 W/ 500 W (Optional)
Laser Focus Diameter	70 – 100 µm
Beam Wavelength	1060 – 1080 nm
Building Volume	250 x 250 x 300 mm
Beam Deflection Speed	8 m/s
Positioning Speed	10 m/s
Build rate	12 – 30 cm^3/h
Layer Thickness	0.02 – 0.1 mm
Layer Width	0.1 mm (single line width)
Recoater Specs	Travel: 650 mm
Building Platform z-axis	Travel: 300 mm/Speed max : 6 mm/s/Res: 0.01 mm
Heating Platform	Up to 200°C
Monitoring of O_2 Level	Below 100 ppm
Permissible Room Temperature	15 – 30°C
Gas (Consumption – running/filling)	7 l/min (running)
System Fill Consumption	20 l/min (up to filling)
Cam Software	Materialise Magics
Control & Other Software	Eplus control software (EPC)
Industrial Interfaces	Ethernet

7. Bibliography

[1] ASTM, “ASTM International Committee F42 for Additive Manufacturing Technologies.” 2009.

[2] J. Gardan, “Additive manufacturing technologies: State of the art and trends,” *Int. J. Prod. Res.*, vol. 54, no. 10, pp. 3118–3132, 2016, doi: 10.1080/00207543.2015.1115909.

[3] W. E. Frazier, “Metal additive manufacturing: A review,” *J. Mater. Eng. Perform.*, vol. 23, no. 6, pp. 1917–1928, 2014, doi: 10.1007/s11665-014-0958-z.

[4] Luca Iuliano, “Tecniche fabbricazione additiva.” DIGEP Department of Politecnico di Torino, 2020.

[5] S. Pratheesh Kumar, S. Elangovan, R. Mohanraj, and J. R. Ramakrishna, “Review on the evolution and technology of State-of-the-Art metal additive manufacturing processes,” *Mater. Today Proc.*, vol. 46, no. xxxx, pp. 7907–7920, 2021, doi: 10.1016/j.matpr.2021.02.567.

[6] D. Herzog, V. Seyda, E. Wycisk, and C. Emmelmann, “Additive manufacturing of metals,” *Acta Mater.*, vol. 117, pp. 371–392, 2016, doi: 10.1016/j.actamat.2016.07.019.

[7] R. . K. Wohlers, T.; Campbell, I.; Diegel, O.; Huff, “3D Printing and Additive Manufacturing State of the Industry: Annual Report 2018.” 2018.

[8] ASTM F2792-12a, “Standard Terminology for Additive Manufacturing Technologies.” 2012.

[9] C. A. G. Lengua, “History of Rapid Prototyping,” in *Rapid Prototyping in Cardiac Disease: 3D Printing the Heart*, K. M. Farooqi, Ed. Cham: Springer International Publishing, 2017, pp. 3–7.

[10] “White Clouds.” [Online]. Available: https://www.whiteclouds.com/3DPedia/fdm.html#:~:text=History of Fused Deposition Modeling,FDM technology and founded Stratasys.

[11] “Ryanwkendall.” [Online]. Available: https://www.ryanwkendall.com/uploads/1/3/3/4/133493762/3d_printing_history.pdf.

[12] W. J. Sames, F. A. List, S. Pannala, R. R. Dehoff, and S. S. Babu, “The metallurgy and processing science of metal additive manufacturing,” *Int. Mater. Rev.*, vol. 61, no. 5, pp. 315–360, 2016, doi: 10.1080/09506608.2015.1116649.

[13] “SmartTech.” [Online]. Available: https://www.smartechanalysis.com/reports/automotive-additive-manufacturing/.

[14] T. E. Endres, “Advantages of Rapid Prototyping,” *SAE International*. 1999, doi: 10.4271/1999-01-3433.

[15] “Desktopmetal.” [Online]. Available: https://www.desktopmetal.com/resources/internal-channels.

[16] “Sculpteo.” [Online]. Available: https://www.sculpteo.com/en/3d-learning-hub/3d-printing-software/lattice-generation-tools/.

[17] “vetted3d.” [Online]. Available: https://www.vetted3d.com/services.

[18] K. S. Prakash, T. Nancharaih, and V. V. S. Rao, “Additive Manufacturing Techniques in Manufacturing -An Overview,” *Mater. Today Proc.*, vol. 5, no. 2, pp. 3873–3882, 2018, doi: 10.1016/j.matpr.2017.11.642.

[19] “Manufactur3dma.” [Online]. Available: https://manufactur3dmag.com/surface-roughness-a-guide-to-metal-additive-manufacturing-by-digital-alloys/.

[20] H.-J. D. Z. Andreas Kirchheim, “Why Education and Training in the Field of Additive Manufacturing is a Necessity,” *Industrializing Additive Manufacturing - Proceedings of Additive Manufacturing in Products and Applications - AMPA2017*. pp. 329–336, 2016, doi: 10.1007/978-3-319-66866-6_31.

[21] W. Xu *et al.*, “Additive manufacturing of strong and ductile Ti-6Al-4V by selective laser melting via in situ martensite decomposition,” *Acta Mater.*, vol. 85, pp. 74–84, 2015, doi: 10.1016/j.actamat.2014.11.028.

[22] J. O. Milewski, *Additive Manufacturing of Metals*, Volume 258. Springer Series in Materials Science, 2017.

[23] F. Calignano *et al.*, “Overview on additive manufacturing technologies,” *Proc. IEEE*, vol. 105, no. 4, pp. 593–612, 2017, doi: 10.1109/JPROC.2016.2625098.

[24] Y. Liu *et al.*, “Optimization of parameters in laser powder deposition AlSi10Mg alloy using Taguchi method,” *Opt. Laser Technol.*, vol. 111, no. March 2018, pp. 470–480, 2019, doi: 10.1016/j.optlastec.2018.10.030.

[25] J. H. H. Sankhya Mohanty, Cem Celal Tutum, “Cellular scanning strategy for selective laser melting: evolution of optimal grid-based scanning path and parametric approach to thermal homogeneity,” *Proceedings Volume 8608, Laser-based Micro- and Nanopackaging and Assembly VII; 86080M*. doi: 10.1117/12.2004256.

[26] “Osti.” [Online]. Available: https://www.osti.gov/pages/servlets/purl/1648875.

[27] V. Gunenthiram *et al.*, “Analysis of laser – melt pool – powder bed interaction during the selective laser melting of a stainless steel To cite this version : HAL Id : hal-01664637,” 2017.

[28] M. Zenou and L. Grainger, *Additive manufacturing of metallic materials*. 2018.

[29] A. Vafadar, F. Guzzomi, A. Rassau, and K. Hayward, “Advances in metal additive manufacturing: A review of common processes, industrial applications, and current challenges,” *Appl. Sci.*, vol. 11, no. 3, pp. 1–33, 2021, doi: 10.3390/app11031213.

[30] Paolo Fino, “Materiali per la fabbricazione additiva.” DISAT Department of Politecnico di Torino, 2020.

[31] L. Jiao, Z. Y. Chua, S. K. Moon, J. Song, G. Bi, and H. Zheng, “Femtosecond laser produced hydrophobic hierarchical structures on additive manufacturing parts,” *Nanomaterials*, vol. 8, no. 8, 2018, doi: 10.3390/nano8080601.

[32] N. C. Daniele Botto, “Optimization for Additive Manufacturing of a Turbine Blade,” 2018, [Online]. Available: https://webthesis.biblio.polito.it/11244/1/tesi.pdf.

[33] D. Zhang *et al.*, “Metal Alloys for Fusion-Based Additive Manufacturing,” *Adv. Eng. Mater.*, vol. 20, no. 5, pp. 1–20, 2018, doi: 10.1002/adem.201700952.

[34] R. Lancaster, G. Davies, H. Illsley, S. Jeffs, and G. Baxter, “Structural integrity of an electron beam melted titanium alloy,” *Materials (Basel).*, vol. 9, no. 6, 2016, doi: 10.3390/ma9060470.

[35] “General Electric.” [Online]. Available: https://www.ge.com/additive/additive-manufacturing/machines/ebm-machines/arcam-ebm-a2x.

[36] “Mechanicalwalkins.” [Online]. Available: http://www.mechanicalwalkins.com/electron-beam-

machining-parts-working-advantages-disadvantages-and-applications/.

[37] S. Bhattacharya, I. V. Singh, and B. K. Mishra, “Mixed-mode fatigue crack growth analysis of functionally graded materials by XFEM,” *Int. J. Fract.*, vol. 183, no. 1, pp. 81–97, 2013, doi: 10.1007/s10704-013-9877-5.

[38] “3dnatives.” [Online]. Available: https://www.3dnatives.com/en/directed-energy-deposition-ded-3d-printing-guide-100920194/.

[39] B. Vayre, F. Vignat, and F. Villeneuve, “Metallic additive manufacturing: State-of-the-art review and prospects,” *Mech. Ind.*, vol. 13, no. 2, pp. 89–96, 2012, doi: 10.1051/meca/2012003.

[40] “Slm-solutions.” [Online]. Available: https://www.slm-solutions.com/.

[41] “Optomec.” [Online]. Available: https://optomec.com/3d-printed-metals/lens-technology/.

[42] Y. J. Liu, Z. Liu, Y. Jiang, G. W. Wang, Y. Yang, and L. C. Zhang, “Gradient in microstructure and mechanical property of selective laser melted AlSi10Mg,” *J. Alloys Compd.*, vol. 735, pp. 1414–1421, 2018, doi: 10.1016/j.jallcom.2017.11.020.

[43] A. I. Mertens, J. Delahaye, and J. Lecomte-Beckers, “Fusion-Based Additive Manufacturing for Processing Aluminum Alloys: State-of-the-Art and Challenges,” *Adv. Eng. Mater.*, vol. 19, no. 8, 2017, doi: 10.1002/adem.201700003.

[44] K. Schmidtke, F. Palm, A. Hawkins, and C. Emmelmann, “Process and mechanical properties: Applicability of a scandium modified Al-alloy for laser additive manufacturing,” *Phys. Procedia*, vol. 12, no. PART 1, pp. 369–374, 2011, doi: 10.1016/j.phpro.2011.03.047.

[45] S. L. Lu, M. Qian, H. P. Tang, M. Yan, J. Wang, and D. H. StJohn, “Massive transformation in Ti-6Al-4V additively manufactured by selective electron beam melting,” *Acta Mater.*, vol. 104, pp. 303–311, 2016, doi: 10.1016/j.actamat.2015.11.011.

[46] C. Qiu, G. A. Ravi, C. Dance, A. Ranson, S. Dilworth, and M. M. Attallah, “Fabrication of large Ti-6Al-4V structures by direct laser deposition,” *J. Alloys Compd.*, vol. 629, pp. 351–361, 2015, doi: 10.1016/j.jallcom.2014.12.234.

[47] H. Liu, Z. Li, F. Gao, Y. Liu, and Q. Wang, “High tensile ductility and strength in the Ti-42Al-6V-1Cr alloy,” *J. Alloys Compd.*, vol. 698, pp. 898–905, 2017, doi: 10.1016/j.jallcom.2016.12.306.

[48] Khorev, “Complex alloying and microalloying of titanium alloys.” 2010, doi: 10.1080/09507116.2010.527059.

[49] B. Konieczny, A. Szczesio-Wlodarczyk, J. Sokolowski, and K. Bociong, “Challenges of co-cr alloy additive manufacturing methods in dentistry-the current state of knowledge (Systematic review),” *Materials (Basel).*, vol. 13, no. 16, pp. 1–15, 2020, doi: 10.3390/MA13163524.

[50] K. Moussaoui, W. Rubio, M. Mousseigne, T. Sultan, and F. Rezai, “Effects of Selective Laser Melting additive manufacturing parameters of Inconel 718 on porosity, microstructure and mechanical properties,” *Mater. Sci. Eng. A*, vol. 735, no. August, pp. 182–190, 2018, doi: 10.1016/j.msea.2018.08.037.

[51] J. Metelkova, Y. Kinds, K. Kempen, C. de Formanoir, A. Witvrouw, and B. Van Hooreweder, “On the influence of laser defocusing in Selective Laser Melting of 316L,” *Addit. Manuf.*, vol. 23, no. August, pp. 161–169, 2018, doi: 10.1016/j.addma.2018.08.006.

[52] X. Nie *et al.*, “Effect of defocusing distance on laser powder bed fusion of high strength Al–Cu–Mg–

Mn alloy," *Virtual Phys. Prototyp.*, vol. 15, no. 3, pp. 325–339, 2020, doi: 10.1080/17452759.2020.1760895.

[53] W. Shifeng, L. Shuai, W. Qingsong, C. Yan, Z. Sheng, and S. Yusheng, "Effect of molten pool boundaries on the mechanical properties of selective laser melting parts," *J. Mater. Process. Technol.*, vol. 214, no. 11, pp. 2660–2667, 2014, doi: 10.1016/j.jmatprotec.2014.06.002.

[54] K. Q. Le, C. Tang, and C. H. Wong, "On the study of keyhole-mode melting in selective laser melting process," *Int. J. Therm. Sci.*, vol. 145, no. April, 2019, doi: 10.1016/j.ijthermalsci.2019.105992.

[55] S. Zhou *et al.*, "Impacts of defocusing amount and molten pool boundaries on mechanical properties and microstructure of selective laser melted AlSi10Mg," *Materials (Basel).*, vol. 12, no. 1, 2018, doi: 10.3390/ma12010073.

[56] N. Takata, H. Kodaira, K. Sekizawa, A. Suzuki, and M. Kobashi, "Change in microstructure of selectively laser melted AlSi10Mg alloy with heat treatments," *Mater. Sci. Eng. A*, vol. 704, no. May, pp. 218–228, 2017, doi: 10.1016/j.msea.2017.08.029.

[57] F. R. J. Mohammad Shamsuzzoha, "DUAL REFINEMENT OF PRIMARY AND EUTECTIC SILICON IN HYPER-EUTECTIC AL-SI ALLOYS," 2007.

[58] A. T. Silvestri *et al.*, "Assessment of the mechanical properties of AlSi10Mg parts produced through selective laser melting under different conditions," *Procedia Manuf.*, vol. 47, no. 2019, pp. 1058–1064, 2020, doi: 10.1016/j.promfg.2020.04.115.

[59] X. Liu, C. Zhao, X. Zhou, Z. Shen, and W. Liu, "Microstructure of selective laser melted AlSi10Mg alloy," *Mater. Des.*, vol. 168, pp. 1–9, 2019, doi: 10.1016/j.matdes.2019.107677.

[60] K. Kempen, L. Thijs, J. Van Humbeeck, and J. P. Kruth, "Mechanical Properties of AlSi10Mg Produced by Selective Laser Melting," *Phys. Procedia*, vol. 39, pp. 439–446, 2012, doi: 10.1016/j.phpro.2012.10.059.

[61] W. Li *et al.*, "Effect of heat treatment on AlSi10Mg alloy fabricated by selective laser melting: Microstructure evolution, mechanical properties and fracture mechanism," *Mater. Sci. Eng. A*, vol. 663, pp. 116–125, 2016, doi: 10.1016/j.msea.2016.03.088.

[62] D. S. Gouveia, Ronny M.Francisco J. G. Silva, Eleonora Atzeni and J. L. A. and A. B. Pereira, "Effect of Scan Strategies and Use of Support Structures on Surface Quality and Hardness of L-PBF AlSi10Mg Parts."

[63] L. Thijs, K. Kempen, J. P. Kruth, and J. Van Humbeeck, "Fine-structured aluminium products with controllable texture by selective laser melting of pre-alloyed AlSi10Mg powder," *Acta Mater.*, vol. 61, no. 5, pp. 1809–1819, 2013, doi: 10.1016/j.actamat.2012.11.052.

[64] "Carpenter Additive AlSi10Mg Powder Datasheet." .

[65] "Prima Industrie SpA Ep Hatch Manual."

[66] "Trimudajatimitra." [Online]. Available: http://www.trimudajatimitra.com/product/isomet-4000-5000-precision-saws/.

[67] ASTM D5671-20, "Standard Practice for Polishing and Etching Coal Samples for Microscopical Analysis by Reflected Light." 2020.

[68] "Direct industry." [Online]. Available: https://www.directindustry.it/prod/phenom-world/product-55442-950167.html.

[69] ASTM E8 / E8M -21, “Standard Test Methods for Tension Testing of Metallic Materials.” 2021.

[70] ASTM E384 – 17, “Standard Test Method for Microindentation Hardness of Materials.” 2017.

[71] M. Riggio and M. Piazza, “Hardness Test,” pp. 87–97, 2010, doi: 10.1007/978-94-007-0560-9_10.

[72] N. O. Larrosa *et al.*, “Linking microstructure and processing defects to mechanical properties of selectively laser melted AlSi10Mg alloy,” *Theor. Appl. Fract. Mech.*, vol. 98, no. June, pp. 123–133, 2018, doi: 10.1016/j.tafmec.2018.09.011.

[73] K. Kempen, L. Thijs, J. Van Humbeeck, and J. P. Kruth, “Processing AlSi10Mg by selective laser melting: Parameter optimisation and material characterisation,” *Mater. Sci. Technol. (United Kingdom)*, vol. 31, no. 8, pp. 917–923, 2015, doi: 10.1179/1743284714Y.0000000702.

[74] F. Trevisan *et al.*, “On the selective laser melting (SLM) of the AlSi10Mg alloy: Process, microstructure, and mechanical properties,” *Materials (Basel).*, vol. 10, no. 1, 2017, doi: 10.3390/ma10010076.

[75] Z. Dong, X. Zhang, W. Shi, H. Zhou, H. Lei, and J. Liang, “Study of size effect on microstructure and mechanical properties of AlSi10Mg samples made by selective laser melting,” *Materials (Basel).*, vol. 11, no. 12, 2018, doi: 10.3390/ma11122463.

[76] X. Nie *et al.*, “Effect of defocusing distance on laser powder bed fusion of high strength Al–Cu–Mg–Mn alloy,” *Virtual Phys. Prototyp.*, vol. 15, no. 3, pp. 325–339, 2020, doi: 10.1080/17452759.2020.1760895.

[77] Y. S. Eom *et al.*, “Fabrication and mechanical properties of Al–Si-based alloys by selective laser melting process,” *Powder Metall.*, vol. 0, no. 0, pp. 1–8, 2021, doi: 10.1080/00325899.2021.1899470.

[78] “Prima Additive.” [Online]. Available: https://www.primaadditive.com/it/tecnologie/powder-bed-fusion/print-sharp-250.